



저작자표시-비영리-변경금지 2.0 대한민국

이용자는 아래의 조건을 따르는 경우에 한하여 자유롭게

- 이 저작물을 복제, 배포, 전송, 전시, 공연 및 방송할 수 있습니다.

다음과 같은 조건을 따라야 합니다:



저작자표시. 귀하는 원저작자를 표시하여야 합니다.



비영리. 귀하는 이 저작물을 영리 목적으로 이용할 수 없습니다.



변경금지. 귀하는 이 저작물을 개작, 변형 또는 가공할 수 없습니다.

- 귀하는, 이 저작물의 재이용이나 배포의 경우, 이 저작물에 적용된 이용허락조건을 명확하게 나타내어야 합니다.
- 저작권자로부터 별도의 허가를 받으면 이러한 조건들은 적용되지 않습니다.

저작권법에 따른 이용자의 권리는 위의 내용에 의하여 영향을 받지 않습니다.

이것은 [이용허락규약\(Legal Code\)](#)을 이해하기 쉽게 요약한 것입니다.

[Disclaimer](#)

공학박사 학위논문

바이자 간섭 기술을 활용한
고체 내 미소 충격파 연구

**A Study on Micro Shock Waves in Solids
using the VISAR Interferometry Technique**

2017년 2월

서울대학교 대학원

기계항공공학부

유 현 주

바이자 간섭 기술을 활용한 고체 내 미소 충격파 연구

A Study on Micro Shock Waves in Solids

using the VISAR Interferometry Technique

지도 교수 여 재 익

이 논문을 공학박사 학위논문으로 제출함

2016년 11월

서울대학교 대학원

기계항공공학부

유 현 주

유현주의 공학박사 학위논문을 인준함

2016년 12월

위 원 장 _____ (인)

부위원장 _____ (인)

위 원 _____ (인)

위 원 _____ (인)

위 원 _____ (인)

Abstract

**A Study on Micro Shock Waves
in Solids using the VISAR
Interferometry Technique**

Hyeonju Yu

Mechanical and Aerospace Engineering

The Graduate School

Seoul National University

Since the early 1900s, as the space and defense industry gained importance, interest in high temperature and pressure phenomena such as collisions, explosions, and the use of energetic materials has been continuously increasing. The properties of materials under extreme conditions such as high temperatures and high pressures are significantly different from those observed under normal atmospheric environment. However, information about the response of condensed matter in extreme conditions is still lacking and needs to be studied.

Plasma-driven shock compression is a promising technique that can generate high-pressure shocks at the laboratory scale in contrast with conventional large-scale high-pressure generators such as gas guns, powder guns, electric guns, and rail guns. Moreover, a plasma-driven shock system has significant advantages in terms of lower cost, lesser time consumed, better control, higher repeatability, and ease of miniaturization of the system. Therefore, in the present study, experiment and numerical analysis were carried out in order to analyze the behavior of plasma-driven micro shock waves with extremely high pressure and short duration.

Diverse plasma-driven shock generators, such as laser-generated shock waves, a laser-driven flyer, and an exploding foil initiator, were developed for access to high pressure and precise control. A high-speed diagnostic using an instrument termed “Velocity Interferometer System for Any Reflector” (VISAR) was conducted to determine the performance characteristics of the developed plasma-driven shock systems. Numerical analysis was also performed for the verification of experimental results and for overcoming experimental limitations.

In this study, all aspects of the system including laser-matter interaction, plasma-driven shock waves, flyer acceleration, shock loading by flyer impact, and shock behavior in solids have been discussed. Therefore, the reported results establish the basis for future shock studies by providing a design guideline for a robust and optimized micro shock system.

Keywords: Shock wave, Hydrodynamic attenuation, Laser, Plasma, Flyer, High velocity, VISAR
Student Number: 2012-30179

Contents

Abstract	i
Contents.....	iii
List of Tables	v
List of Figures.....	vi
Preface.....	xi
Chapter 1. Introduction	1
Chapter 2. Experimental Apparatus	3
2.1 LASER.....	3
2.2 Exploding Foil Initiator.....	5
2.3 High Speed Camera	9
2.4 VISAR.....	10
2.4.1 Superposition and Interference of Waves	12
2.4.2 Heterodyne and Homodyne Interferometers	14
2.4.3 Velocity Calculation	17
Chapter 3. Generation of Micro Shock Waves	19
3.1 Laser-Driven Flyer Acceleration	19
3.1.1 Background and Motivation.....	19
3.1.2 Experimental Approach	21

3.1.3 Results and Discussion	26
3.2 High Velocity Impact by Laser-Driven Flyer.....	41
3.2.1 Background and Motivation.....	41
3.2.2 Experimental Approach	42
3.2.3 Results and Discussion	52
Chapter 4. Analysis of Micro Shock Waves in Solids.....	63
4.1 Evolution and Decay of Laser-Generated Shock Waves	63
4.1.1 Background and Motivation.....	63
4.1.2 Experimental Approach	64
4.1.2 Numerical Approach.....	68
4.1.3 Results and Discussion	76
4.2 Shock Waves Generated by Flyer Impact	88
4.2.1 Background and Motivation.....	88
4.2.2 Experimental Approach	90
4.2.2 Numerical Approach.....	98
4.2.3 Results and Discussion	104
Chapter 5. Conclusions	113
References	118
Abstract in Korean	130

List of Tables

Table 2.1. Characteristics of heterodyne and homodyne interferometers.....	16
Table 3.1. Flyer plate composition and dimension.	24
Table 3.2. Increase in flyer velocity with a black paint coating.	28
Table 3.3. Material properties.....	29
Table 3.4. Increase in normalized momentum of flyer with a black paint coating.	34
Table 3.5. Launcher composition.....	45
Table 4.1. Shock Hugoniot data of 304 stainless steel and water.	70
Table 4.2. Estimated reflectivity of target surface and time occurrence of laser ablation according to laser fluence.	83
Table 4.3. Shock Hugoniot data for 304 stainless steel and Kapton [63, 79].	102
Table 4.4. Parameters of Steinberg-Guinan strength model for 304 stainless steel [80].	104

List of Figures

Fig. 2.1. Powerlite Nd:YAG laser: Laser bench and electronic cabinet.....	4
Fig. 2.2. Spectra Nd:YAG laser.....	4
Fig. 2.3. Minilite Nd:YAG laser: Laser bench and electronic cabinet.....	5
Fig. 2.4. Picture of the (a) test EFI module, (b) initiation circuit, and (c) power supply.....	7
Fig. 2.5. Schematic of an EFI detonator.....	7
Fig. 2.6. (a) Metal bridge foil configured as a bridge structure having a narrow channel and (b) SEM image after firing.....	8
Fig. 2.7. Phantom v711 high speed camera.....	9
Fig. 2.8. (a) Picture and (b) Schematic of the VISAR.....	11
Fig. 3.1. (a) Experimental setup and (b) Laser driven flyer configuration.....	23
Fig. 3.2. Velocity of flyer plate: (a) aluminum_2.1 mm diameter and 50 μm thickness, (b) aluminum_2.1 mm diameter and 100 μm thickness, (c) copper_50 μm thickness and 2.6 mm diameter.....	27
Fig. 3.3. Comparison of % increase of velocity due to respective coating: A [8], B [11], C [12], and D [This work].....	32
Fig. 3.4. Flyer thickness effect: (a) copper with black paint, (b) aluminum with black paint.....	35
Fig. 3.5. Effect of black paint coating: (a) copper, (b) aluminum.....	36
Fig. 3.6. High-speed images (6.7 μs interval time) of flyers of 50 μm thickness and 2.6 mm diameter using 1.3 J laser energy: (a)	

copper, (b) copper with black paint.	37
Fig. 3.7. Random fragmentation of ‘thin’ (15 μm thick, 2.1 mm diameter) aluminum flyer with black-paint coating at 0.6 J laser energy: (a) 10 μs , (b) 20 μs , and (c) 30 μs after irradiation.	39
Fig. 3.8. Fastest particle velocity measured for ‘thin’ aluminum flyer of 2.1 mm diameter and 15 μm thickness.	40
Fig. 3.9. (a) Schematic view of experimental setup and (b) Launcher configuration.	44
Fig. 3.10. (a) Installation of ice particles on the launcher, (b) Small amount of ice particles located at the ablation point of the launcher.	47
Fig. 3.11. Schematic view of double exposure shadowgraph.	48
Fig. 3.12. Schematic view of velocity interferometer system for any reflector (VISAR).	49
Fig. 3.13. Cross-sectional view of a crater formed by collision of an ice particle at the velocity of 198 m/s.	52
Fig. 3.14. High-speed images (4.75 μs time interval) of ice particle using 500 mJ of laser energy.	53
Fig. 3.15. Double exposure shadowgraphs by 200 ns of exposure interval using 500 mJ of laser energy: (a) reference image before the laser irradiation and (b) flight motion of ice particles after the laser irradiation.	54
Fig. 3.16. Performance map of laser-driven accelerator: circular and square symbols represent velocity of ice particles and free surface velocity of metal foil, respectively.	55
Fig. 3.17. Damaged acrylic substrate per laser irradiance. The opacity of damaged area and cracks are induced by light absorption	

of an acrylic substrate and the recoil momentum of plasma, respectively.....	56
Fig. 3.18. Velocity history of free surface of metal foil and longitudinal stress profile of shock wave at 500 mJ laser energy: (a) direct ablation, (b) multi-layered (launcher composition) ablation.	58
Fig. 3.19. Velocity of ice particles as a function of peak pressure of the longitudinal wave.	60
Fig. 3.20. Dimension of crater: (a) diameter, and (b) depth.	61
Fig. 4.1. (a) Schematic view of experimental setup and (b) Target assembly.	65
Fig. 4.2. Temporal profile of the free surface velocity according to the thickness of a target at laser energy of 8.6 J/cm^2	76
Fig. 4.3. Evolution and decay of shock pressure represented by analytical model and experimental results.	78
Fig. 4.4. Temporal profile of (a) plasma pressures at laser pulse of various laser fluence and (b) normalized laser intensity and plasma pressure for 10.9 J/cm^2	80
Fig. 4.5. (a) Laser energy used for ablation of 304 stainless steel and (b) Temporal profile of plasma pressure after laser ablation according to laser fluence.	82
Fig. 4.6. (a) Pressure, (b) Velocity, and (c) Acceleration of a shock front with respect to the distance of wave propagation at various laser fluence.	85
Fig. 4.7. Velocity and acceleration profile of free surface at laser pulse of 8.6 J/cm^2	86
Fig. 4.8. (a) Operation sequence and schematic of an exploding foil	

initiator and (b) Metal foil layer configured as a bridge structure having a narrow channel.	91
Fig. 4.9. Target assembly of the test EFL.....	92
Fig. 4.10. Impedance matching technique for a relatively soft (Kapton) flyer impact on a hard (SS304) target.	93
Fig. 4.11. Assembly configuration of the improved VISAR probe.	95
Fig. 4.12. Gaussian beam propagation with a focusing lens: spot size and total beam divergence determined by the focal length of a lens and the diameter of the incident beam.	96
Fig. 4.13. Schematic of overall experimental setup.....	97
Fig. 4.14. Geometry and mesh of finite element model for 2-D axisymmetric flyer impact.....	100
Fig. 4.15. Temporal profile of the free surface velocity measured by VISAR for a 304 stainless steel target of 100 μm thickness at the capacitor charging voltage of 1 kV.	104
Fig. 4.16. Particle velocity generated by the shock front according to the distance of wave propagation within a 304 stainless steel target.....	106
Fig. 4.17. Temporal profile of shock loading generated by flyer impact at the various velocity.	107
Fig. 4.18. Temporal profile of (a) longitudinal stress and (b) particle velocity generated by flyer impact at 1.25 km/s, which are recorded by gauges placed at intervals of 10 μm along the central axis from 0 to 350 μm	109
Fig. 4.19. Pressure contour of a 304 stainless steel target and a Kapton flyer along the wave propagation when it collides at the	

velocity of 1.25 km/s.....	109
Fig. 4.20. Pressure-velocity diagram for single shock waves.	112

Preface

This thesis is based on the following publications and manuscripts.

Paper 1

Hyeonju Yu, Vitalij Fedotov, Wonkye Baek, and Jack J. Yoh. Towards controlled flyer acceleration by a laser-driven mini flyer. *Applied Physics A*, 2014, 115.3: 971-978.

Paper 2

Hyeonju Yu, Jungwook Kim, and Jack J. Yoh. A high velocity impact experiment of micro-scale ice particles using laser-driven system. *Journal of Applied Physics*, 2014, 116.17: 173508.

Paper 3

Hyeonju Yu and Jack J. Yoh. Laser-generated shock wave attenuation aimed at microscale pyrotechnic device design. *AIP Advances*, 2016, 6.5: 055314.

Paper 4

Hyeonju Yu, Bohoon Kim, Kyu-Hyoung Kim, Seung-Gyo Jang, and Jack J. Yoh. Performance characterization of a miniaturized explosive foil initiator via VISAR and shock wave analysis. *Journal of Applied Physics*, submitted for publication.

The contents are reproduced with permission of the co-authors and the publishers. Copyright of the publications remains with the publishers.

Chapter 1. Introduction

Investigations of shock compression of condensed matter began in the early 1900s and have been explosively increasing since it was applied to the space and defense industries during World War II. The properties of materials under extreme conditions are significantly different from those observed in normal atmospheric environment. Consequently, shock physics have been focusing on understanding response of condensed matter in extreme environments, such as impact, explosion, and the use of energetic materials.

The study of shock physics consists of the development of high-pressure shock generators, high-speed and high-resolution diagnostics, and theoretical analysis of observed phenomena. As for development of a high-pressure compression system for shock experiments, access to high pressures and precise control capabilities are important performance factors. High-speed diagnostics, including all kinds of measuring and recording equipment, is also essential to observe the response of condensed matter under shock compression. Observed results are analyzed through a theoretical approach to explain physical phenomena.

High-pressure shock compression rely on various techniques. Gas and powder guns are usually gigantic and cannot mount small, thin flyers of millimeter to micron thickness. Electric and rail guns require a non-conducting flyer plate or otherwise a dielectric layer to be placed between the launch pad and a conducting flyer plate. However, Plasma-driven shock

compression is a promising technique that can generate high-pressure shocks at the laboratory scale in contrast with conventional large-scale high-pressure generators such as gas guns, powder guns, electric guns, and rail guns. It also has significant advantages in terms of lower cost, lesser time consumed, better control, higher repeatability, and ease of miniaturization of the system. Therefore, in the present study, diverse plasma-driven shock generators, such as laser-generated shock waves, a laser-driven flyer, and an exploding foil initiator, were developed for access to high pressure and precise control.

Velocity measurements play an important part in shock compression studies. Velocity information under extreme condition is commonly easier to obtain than pressure and temperature. Based on measured velocity, other thermomechanical information of materials can also be calculated from the conservation law of mass and momentum. Hence, a velocity interferometer system for any reflector (VISAR), which is suitable for high speed and non-intrusive diagnostics, was adopted to measure the velocity of a moving surface during shock compression.

In this study, experiment and numerical analysis were carried out in order to analyze the behavior of plasma-driven micro shock waves with extremely high pressure and short duration. All aspects of the system including laser matter interaction, plasma-driven shock waves, flyer acceleration, shock loading by flyer impact, and shock attenuation in solids have been discussed. Therefore, the reported results establish the basis for future shock studies by providing a design guideline for a robust and optimized micro shock system.

Chapter 2. Experimental Apparatus

Shock generators and measuring equipment are necessary to conduct a shock experiment. In this experiment, plasma-driven compression systems were used to apply various compressive shock loadings to a target material. A flyer was accelerated to velocity up to an order of kilometers per second by using a laser-driven flyer system and an exploding foil initiator, respectively. Plasma in orders of gigapascal was also generated by direct laser ablation. Diverse diagnostic tools, such as a high speed camera, a shadowgraph, and a velocity interferometer system for any reflector (VISAR), were used to measure the response of condensed matter under shock compression.

2.1 LASER

Powerlite (Continuum Inc.) and Spectra (Lutronic Corp.) Q-switched Nd:YAG lasers are used as driving sources for shock generation. Powerlite emits a laser pulse at maximum 3 J with 1064 nm wavelength, 9 ns duration, and Gaussian spatial profile. The fundamental wavelength, 1064 nm, can be changed into 532, 355, 266 nm by using the second, third, and fourth harmonic generator, respectively. Spectra emits dual wavelength laser beams of 1064 and 532 nm with 5 ns pulse width and flat-top spatial profile. Maximum energy is 1200 and 400 mJ at 1064 and 532 nm, respectively.



Fig. 2.1. Powerlite Nd:YAG laser: Laser bench and electronic cabinet.



Fig. 2.2. Spectra Nd:YAG laser.

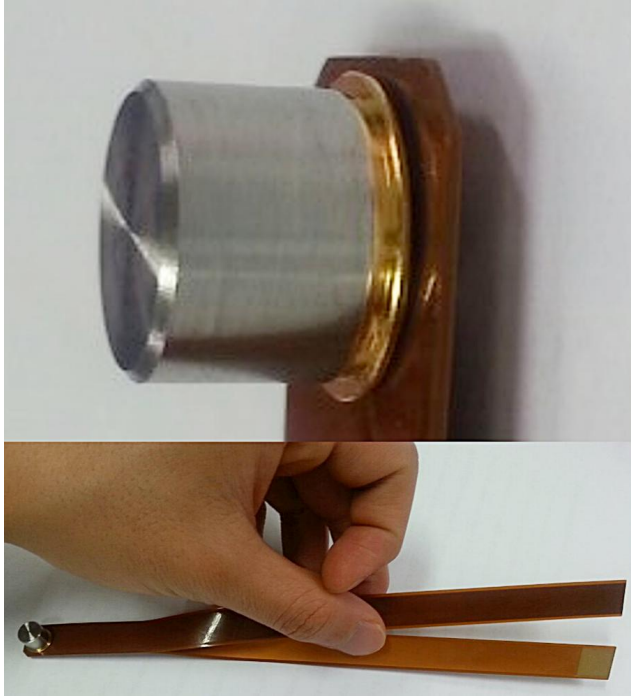
Minilite (Continuum Inc.) Q-switched Nd:YAG laser is used for a double exposure shadowgraph, because it contains two lasers on a laser bench. Two 1064 nm fundamental laser beams discharged from each laser resonator are superimposed to share a common optical path, passing through a single doubling crystal. Output beams at maximum 25 mJ with 532 nm wavelength and 3 ns pulse duration are emitted.



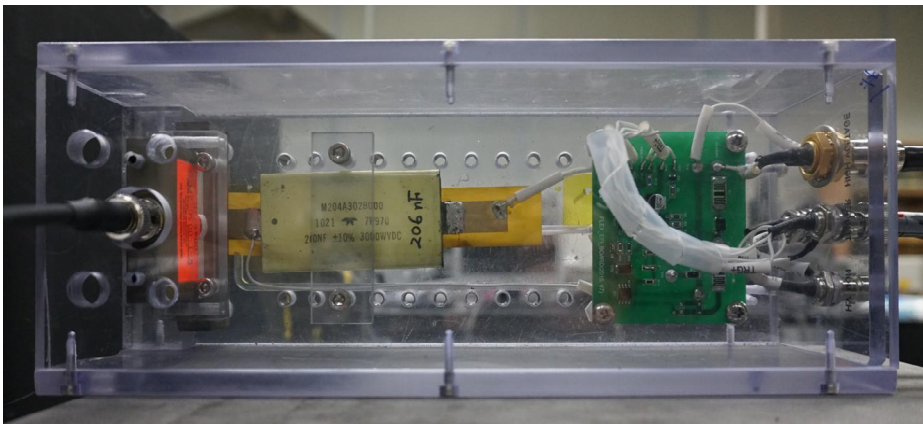
Fig. 2.3. Minilite Nd:YAG laser: Laser bench and electronic cabinet.

2.2 Exploding Foil Initiator

An exploding foil initiator (EFI) is used to accelerate a flyer for applying shock loading to a target material. A Kapton flyer of 165 μm diameter and 12.5 μm thickness reaches velocity up to 5 km/s. Figure 2.4 represents the picture of the test EFI module, initiation circuit, and power supply. The schematic of an EFI detonator is presented in Fig. 2.5.



(a)



(b)



(c)

Fig. 2.4. Picture of the (a) test EFI module, (b) initiation circuit, and (c) power supply.

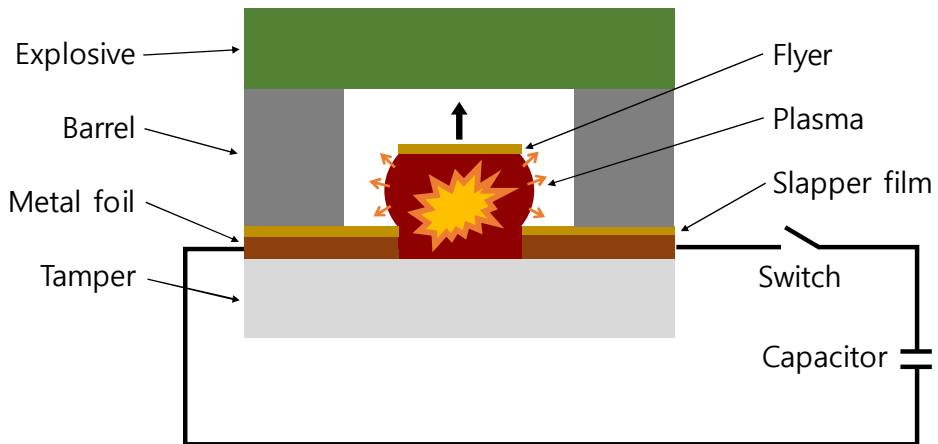
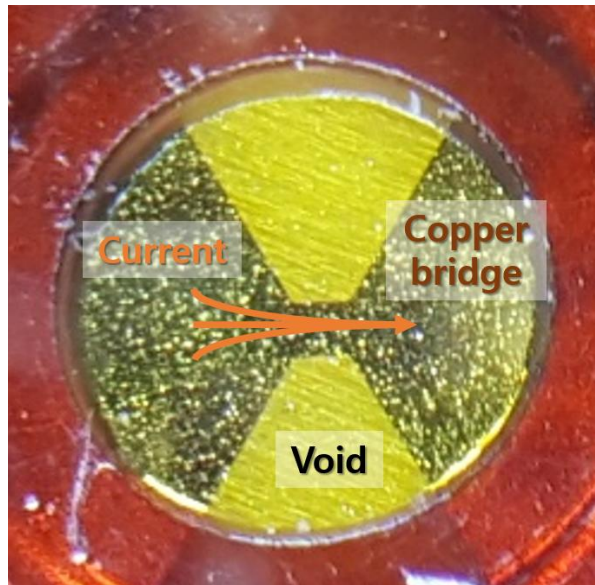
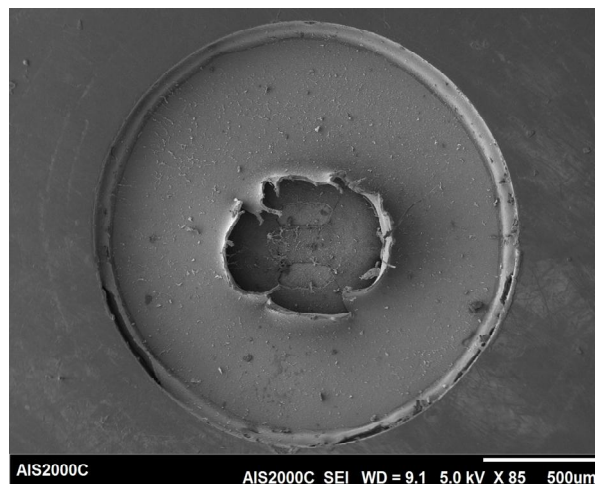


Fig. 2.5. Schematic of an EFI detonator.



(a)



(b)

Fig. 2.6. (a) Metal bridge foil configured as a bridge structure having a narrow channel and (b) SEM image after firing.

Fig. 2.6 shows thin metal bridge foil configured as a bridge structure having a narrow channel and the SEM image after firing. When the electric current pulse of a capacitor, which is charged up to several thousand volts, is discharged onto a thin metal bridge foil, the foil undergoes an explosive phase change to a plasma state, as the electrical resistance is at maximum in the narrow channel. The expansion of high-density plasma rapidly accelerates the flyer to the desired velocity by varying the charging voltage of the capacitor. Subsequently, an explosive block is initiated from a shock wave generated by the flyer impact.

2.3 High Speed Camera



Fig. 2.7. Phantom v711 high speed camera.

Phantom v711 (Vision Research Inc.) high speed camera is used to measure

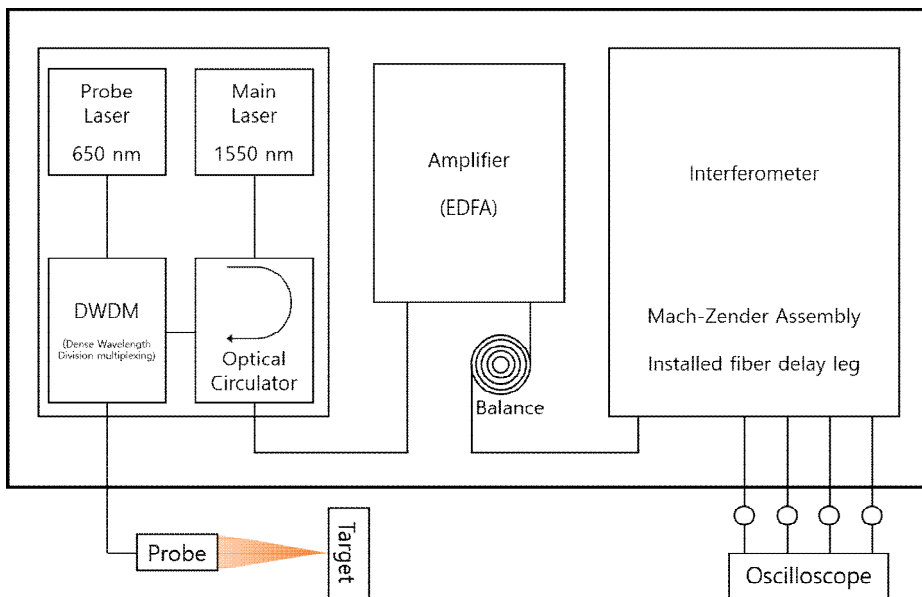
the velocity of a flyer. The Phantom v711 includes a CMOS sensor with 1 megapixel and 8 & 12 bit depth. The camera can deliver up to a maximum speed of 7530 frame per second (fps) at full resolution of 1280 x 800 pixels. At reduced resolution of 128 x 8 pixels, a maximum speed 1,400,000 fps is achieved with the fast option. A sub-microsecond shutter that goes from 1 μ s to 300 ns makes it possible to capture a clear image by eliminating image blur. And overexposed and saturated parts of an image are handled to increase visible information by a function of extreme dynamic range which allows two different exposures within a single frame.

2.4 VISAR

Velocity interferometry suitable for high speed and non-intrusive diagnostics plays an important role in shock compression studies. Based on the conservation law of mass, momentum, and energy, the velocity of a moving surface during shock compression yields pressure, temperature, and other thermomechanical information of materials under extreme conditions. In this study, Mark IV-3000 (Martin, Froeschner & Associates) VISAR is used and its picture and schematic are shown in Fig. 2.8. Here, an ultra-narrow line width (<20 kHz) semiconductor diode laser was used, operating at 1550 nm with a power of 5 mW, to minimize any signal broadening. The probe beam is focused onto a target surface of interest, whose velocity is to be measured, and then reflected from the target surface.



(a)



(b)

Fig. 2.8. (a) Picture and (b) Schematic of the VISAR.

The returning beam, passing through a band pass filter, is directed to the interferometer which is a delay leg, Mach-Zehnder type. Four output signals from Quadrature Push-Pull interferometer are split by a polarizing beam splitter. The intensities of four outputs are converted to electric signal by four 10 GHz fiber coupled photodetectors and then recorded by a digital oscilloscope. Fundamental principle of VISAR [1, 2] to derive the velocity of a target from interference signals is as follows.

2.4.1 Superposition and Interference of Waves

An interferometer is based on superposition of two electromagnetic waves, which undergoes constructive and destructive interferences according to phase, to measure some meaningful property. The interference-phase shifts are inferred from the intensity change of an inference signal (or fringe shift) measured by a photodetector. When considering one-dimensional propagating plane waves, which have different amplitudes, frequencies, propagation directions, and the same polarization, the total electric field is represented as

$$\begin{aligned} E_t(x,t) &= E_1(x,t) + E_2(x,t) \\ &= A_1 \cos(k_1x - w_1t + \phi_1) + A_2 \cos(k_2x - w_2t + \phi_2) \end{aligned} \quad (2.1)$$

where E is electric field of a light wave. A , k , w , and ϕ represent the peak amplitude, wavenumber, angular frequency, and initial phase of each electric field, respectively. The intensity of an interference signal is given by

the time average of the total electric field squared.

$$\begin{aligned}
I(x,t) &= \langle E_t^2(x,t) \rangle = \langle \{E_1(x,t) + E_2(x,t)\}^2 \rangle \\
&= \langle \{A_1 \cos(k_1x - w_1t + \phi_1) + A_2 \cos(k_2x - w_2t + \phi_2)\}^2 \rangle \\
&= \langle A_1^2 \cos^2(k_1x - w_1t + \phi_1) \rangle + \langle A_2^2 \cos^2(k_2x - w_2t + \phi_2) \rangle \\
&\quad + \langle 2A_1A_2 \cos(k_1x - w_1t + \phi_1) \cos(k_2x - w_2t + \phi_2) \rangle \quad (2.2) \\
&= \frac{A_1^2}{2} + \frac{A_2^2}{2} + \langle 2A_1A_2 \cos(k_1x - w_1t + \phi_1) \cos(k_2x - w_2t + \phi_2) \rangle \\
&= I_1 + I_2 + \langle 4\sqrt{I_1I_2} \cos(k_1x - w_1t + \phi_1) \cos(k_2x - w_2t + \phi_2) \rangle
\end{aligned}$$

The remaining time average term can be expanded by a trigonometric relationship, $2 \cos A \cos B = \cos(A+B) \cos(A-B)$.

$$\begin{aligned}
I(x,t) &= I_1 + I_2 + \langle 2\sqrt{I_1I_2} \cos\{(k_1 + k_2)x - (w_1 + w_2)t + (\phi_1 + \phi_2)\} \rangle \\
&\quad + \langle 2\sqrt{I_1I_2} \cos\{(k_1 - k_2)x - (w_1 - w_2)t + (\phi_1 - \phi_2)\} \rangle \quad (2.3)
\end{aligned}$$

Here, $I_1 + I_2$ and $2\sqrt{I_1I_2}$ respectively represent the intensity of background and interference fringes. The first time average term goes to zero because the frequency of light waves is too high to be measured by existing detectors. However, the second time average term slowly varies with the phase difference of the two waves. Finally, the intensity of an interference signal is expressed as follows.

$$I(x,t) = I_1 + I_2 + 2\sqrt{I_1I_2} \cos\{(k_1 - k_2)x - (w_1 - w_2)t + (\phi_1 - \phi_2)\} \quad (2.4)$$

2.4.2 Heterodyne and Homodyne Interferometers

In a laser Doppler velocity interferometry, the light is split and propagates in the unequal paths, one of which is longer than the other due to a delay leg. And then each light traveling a different route is superposed at the recombined point. Although interference is induced by the same process, a velocity interferometer system is distinguished into heterodyne and homodyne interferometers according to the frequency of a reference beam by which different fringe shifts are obtained at the same velocity condition.

A heterodyne velocity interferometer is based on a Michelson interferometer in which the Doppler shifted light is combined with un-shifted reference light that is the fundamental light of a laser system. The intensity of an interference signal, which varies with a beat frequency between the Doppler shifted light and the un-shifted reference light, is represented with assumption that a position is fixed for simplifying analysis (in which a phase shift is a function of time and a frequency).

$$I(t) = I_1 + I_2 + 2\sqrt{I_1 I_2} \cos \left\{ \int 2\pi f_b(t) dt + \phi_0 \right\} \quad (2.5)$$

$$f_b(t) = f_d(t) - f_0 = \frac{2v(t)}{c} f_0 \quad (2.6)$$

where f_b , f_d , f_0 and respectively represent the frequency of the beat, Doppler shifted, and reference signals. ϕ_0 is the initial phase of a beat signal. The Doppler shifted frequency according to the velocity, v , of a target is approximated as

$$f = f_0 \left(\frac{c+v}{c-v} \right) \approx f_0 \left(1 + \frac{2v}{c} \right) \quad (2.7)$$

Here f and c represent frequency and speed of light, respectively, and v is the velocity of a target. The approximation is reasonable in case that v/c is usually less than 0.001. Finally, the phase shift is expressed as

$$\begin{aligned} \Delta\phi(t) &= \int 2\pi f_b(t) dt = \int \frac{4\pi f_0}{c} v(t) dt \\ &= \frac{4\pi}{\lambda_0} \int v(t) dt = \frac{4\pi}{\lambda_0} \Delta d \end{aligned} \quad (2.8)$$

where λ represents the wavelength of light. Since the fringe shift is proportional to the displacement of a target, a heterodyne velocity interferometer actually is a displacement interferometer. However, the velocity can also be obtained through a fast Fourier transform. The phase shift in a heterodyne velocity interferometer is proportional to the velocity of a target.

$$v(t) = \frac{\lambda_0}{2} f_b(t) \quad (2.9)$$

On the other hand, a homodyne velocity interferometer is based on a Mach-Zehnder interferometer in which the Doppler shifted light is combined with the time-delayed Doppler shifted light. The intensity of an interference signal, which varies with a beat frequency between the Doppler shifted light and the time-delayed reference light, is represented in the same manner as a heterodyne interferometer.

$$I(t) = I_1 + I_2 + 2\sqrt{I_1 I_2} \cos \left\{ \int 2\pi f_b(t) dt + \phi_0 \right\} \quad (2.10)$$

$$f_b(t) = f_d(t) - f_d(t - \tau) = \frac{2\{v(t) - v(t - \tau)\}}{c} f_0 = \frac{2\Delta v}{c} f_0 \quad (2.11)$$

The phase shift is expressed as

$$\begin{aligned} \Delta\phi(t) &= \int_{t-\tau}^t 2\pi f_b(t) dt = \int_{t-\tau}^t \frac{4\pi f_0 \Delta v}{c} dt \\ &= \frac{4\pi}{\lambda_0} \int_{t-\tau}^t \Delta v dt = \frac{4\pi\tau_{res}}{\lambda_0} \Delta v \end{aligned} \quad (2.12)$$

Compared to a heterodyne velocity interferometer, the phase shift in a homodyne velocity interferometer is proportional to not the displacement but the velocity change of a target. The characteristics of heterodyne interferometer and homodyne interferometers are summarized in Table 2.1.

Table 2.1. Characteristics of heterodyne and homodyne interferometers.

	Heterodyne interferometer	Homodyne interferometer
Base	Michelson	Mach-Zehnder
Representative	PDV	VISAR
Superposition	Doppler shifted light and fundamental light	Doppler shifted light and time-delayed one of that
Fringe shift	Proportional to displacement	Proportional to velocity
Beat frequency	Very high	Low

Pros. and Cons.	Expensive High specification of detector and digitizer	Relatively inexpensive Moderate specification of detector & digitizer
	Multiple velocities measurement	Single velocity measurement
	Continuous detection is unnecessary (Measurement of absolute velocity)	Continuous detection is necessary (Measurement of relative velocity)
	Differentiation is necessary to calculate velocity (Displace measurement)	Differentiation is unnecessary to calculate velocity (Velocity measurement)

2.4.3 Velocity Calculation

When considering the lights having the same intensity with background light, $I_{bg}(t)$, the intensity of an interference signal, $I(t)$ is written as

$$I(t) = I_0 [1 + \cos \phi(t)] + I_{bg}(t) \quad (2.13)$$

The interference signal is split into four interference signals with a phase difference of 90° by passing through polarizing beam splitters.

$$\begin{aligned} I_1(t) &= I_0 [1 + \sin \phi(t)] + I_{bg}(t) \\ I_2(t) &= I_0 [1 + \cos \phi(t)] + I_{bg}(t) \end{aligned} \quad (2.14)$$

$$\begin{aligned}
I_3(t) &= I_0 [1 - \sin \phi(t)] + I_{bg}(t) \\
I_4(t) &= I_0 [1 - \cos \phi(t)] + I_{bg}(t)
\end{aligned}
\tag{2.14}$$

By subtracting the signals of sine and cosine pairs, the idealized interference signals are determined.

$$\begin{aligned}
x(t) &\equiv I_1(t) - I_3(t) = 2I_0 \cos \phi(t) \\
y(t) &\equiv I_2(t) - I_4(t) = 2I_0 \sin \phi(t)
\end{aligned}
\tag{2.15}$$

By using Eqs. (2.12) and (2.15), the velocity of a target is finally calculated from the intensity of interference signals.

$$\Delta v = K_f \frac{\Delta \phi}{2\pi} = \frac{K_f}{2\pi} \left[\tan^{-1} \left(\frac{y(t)}{x(t)} \right) - \phi_0 \right]
\tag{2.16}$$

$$K_f = \frac{\lambda_0}{2\tau} = \frac{\lambda_0 c}{2nL}
\tag{2.17}$$

where K_f is a fringe constant representing velocity increase per fringe. L , n , and τ are respectively the length, refractive index, and time delay (or resolution) of a delay leg.

Chapter 3. Generation of Micro Shock Waves

3.1 Laser-Driven Flyer Acceleration

3.1.1 Background and Motivation

Laboratory techniques using high-pressure shocks for a flyer acceleration process rely on one of three experimental concepts [3]: laboratory (powder or gas) guns, electric (or rail) guns, and less commonly laser-driven systems. Laboratory guns are usually gigantic and cannot mount small, thin flyers of millimeter to micron thickness. Electric guns require a non-conducting flyer plate or otherwise a dielectric layer to be placed between the launch pad and a conducting flyer plate. Less commonly, the laser-driven strong shock wave deposits laser energy in a few skin depths of the ablative surface, thereby thrusting what remains of the flyer material out by ejecting ablated product towards the direction of the laser beam. Unlike the first two gun-type acceleration systems, the laser-based method has advantages in terms of cost, repeatability, time consumed, and potential controllability. Such a system is desired where high-pressure shocking via impact of small objects is desired [4-6] as in the case of a mini-flyer launching system.

Here, a laser system is configured to accelerate an aluminum plate of 2.1 mm diameter and a copper plate of 2.6 mm diameter of different thicknesses (50 and 100 μm) to velocities up to an order of kilometers per second. A short pulse (9 ns) laser (Nd:YAG) at 1064 nm is used to irradiate the interface

between the substrate and the flyer material. When the intensity of the laser beam is higher than 10^{10} W/m², a rapid temperature rise of the flyer surface gives rise to an explosive phase change or plasma state, and then surface evaporation induces pressure recoil and momentum [7]. This plasma trapped between the substrate and the remaining flyer plate expands towards the ablative material while accelerating the flyer [8]. Given that the substrate cannot transmit infinite energy without subsequent system damage, it is necessary to maximize flyer velocity given a bearable incoming laser energy, typically below 0.6 J, and still be able to generate particle velocity comparable to or faster than what was attainable via similar LDF systems reported in the literature [3, 8, 9].

Existing LDF studies have used multi-layered flyer plate techniques that are aimed at increasing the flyer velocity [8, 10-12]. Each multiple-layer material is chosen to enhance particle acceleration. The first layer is an absorption layer for laser energy input at a minimal loss which transfers energy onto the ablation layer. The ablation layer needs to be vaporized in an instant for successful flyer launch. An insulating dielectric layer limits the extent of heat transfer and the phase change, protecting the flyer layer from possible melting [8, 11]. This multi-layered configuration, however, requires special techniques such as electron beaming and magnetron sputtering, which are rather expensive and time consuming [13]. In our work, the research is aimed at improving flyer coupling efficiency or the ratio of the laser energy to the flyer kinetic energy by using a single coat of black paint. A commercial-grade black lacquer paint is used as a coat and tested for its superior performance despite

the simplicity of the system concept. The flyer velocity was determined as a function of the laser energy, and the flyer coupling efficiency was then calculated for each shot tested.

The performance of the laser-driven flyer (LDF) is evaluated by varying the optical and physical properties of the light source as well as the ablative material. The velocity is precisely measured using high-speed photography (Phantom v711 at maximum 1,000,000 fps). The present LDF system is suitable for accelerating a mini flyer with an improved control over its size, shape, and velocity in comparison to its predecessor LDF system. Among various other potential uses, this launch device is suited for micrometeorite impact simulation, micro bullet testing for body armor testing, nanoscale material shock testing, and micro-ice particle impact for turbine blade survivability testing of airborne turbojet engines.

3.1.2 Experimental Approach

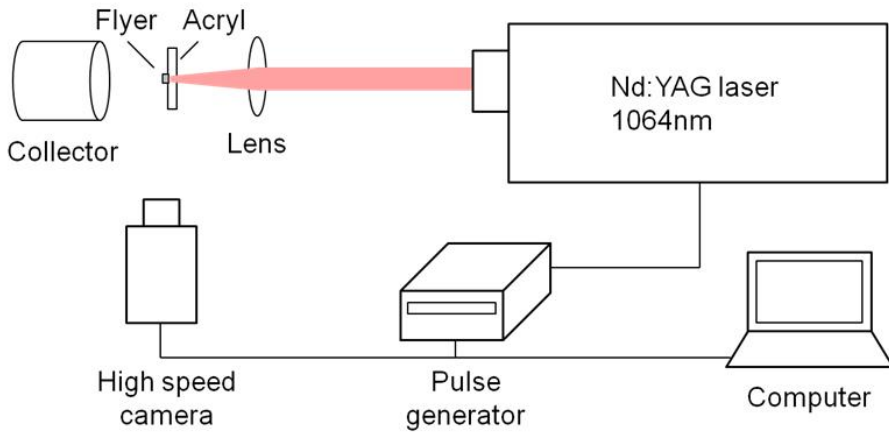
Using a Q-switched Nd:YAG laser, we are able to accelerate 50, 100 μm thickness, 2.1, 2.6 mm diameter aluminum and copper flyer plates to velocities of an order of km/s with 100-600 mJ at 1.064 μm wavelength and 9 ns pulse duration. A spot diameter of 2 mm is obtained with a 100 mm focal lens.

The impedance of the substrate material plays an important role in the resulting flyer velocity. Paisley [3] adopted a confinement method to increase

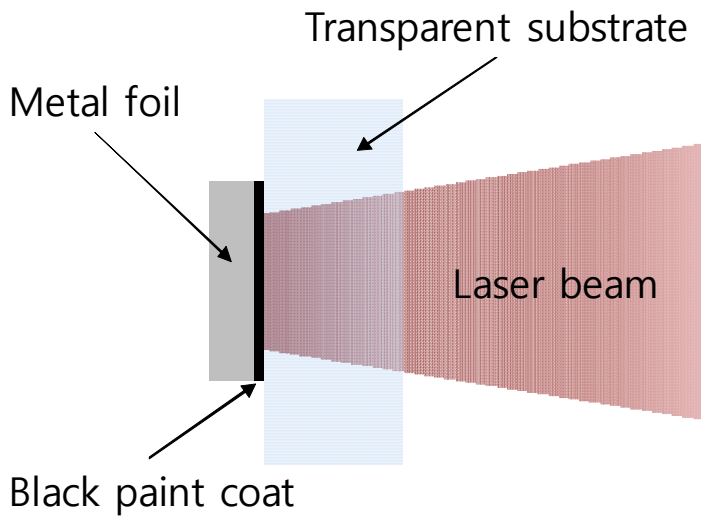
the flyer velocity without the direct ablation method; the ablated product confined between the metal surface and high-impedance transparent material resulted in a higher thrust. Robbins et al. [6] studied the effects of sapphire, fused silica, laser-grade BK7, and commercial-grade BK7 as window materials. There, they found that a sapphire window accelerates the flyer to a slightly higher velocity at first, but its terminal velocity is somewhat slower [6]. Their results represent that the substrate window and the transparent substrate have little effect on flyer velocity. Thus, choosing a transparent substrate is not the most daring task; rather, low cost and machinability are deemed more important in designing an efficient mini launch system [14]. We selected acrylic as a substrate window, which is both commercially available at low cost and can be manufactured quite easily.

The present LDF system consists of a flyer plate attached to an acrylic substrate which has over 90 % transmission for 1.604 μm wavelength. A low intensity of the laser beam is used below the breakdown threshold of acryl to avoid any optical damage, except for the surface damage that results from the launch of the flyer plate. As shown in Fig. 3.1, the laser beam is directed through a band-pass filter, for blocking the flash-lamp light, a convex lens, and then onto the rear of a substrate window. A long focal length lens is used to reduce the tolerance in beam diameter, which is controlled by moving the substrate/flyer plate assembly back and forth. The flyer plate diameters tested have been 2.1 and 2.6 mm that are greater than the flyer thickness of 100 μm . This dimension of a flyer plate guaranteed a high degree of planarity during the flight. Metals such as Al and Cu are used as flyer plates, and black paint is

used as an absorption/ablation layer.



(a)



(b)

Fig. 3.1. (a) Experimental setup and (b) Laser driven flyer configuration.

Table 3.1. Flyer plate composition and dimension.

Material	Absorption layer	Thickness [μm]	Diameter [mm]	Mass [g]
Aluminum	No coat	50	2.1	4.676×10^{-4}
Aluminum	Black paint (carbon)	55	2.1	5.014×10^{-4}
Aluminum	No coat	100	2.1	9.352×10^{-4}
Aluminum	Black paint (carbon)	105	2.1	9.689×10^{-4}
Copper	No coat	50	2.6	2.371×10^{-4}
Copper	Black paint (carbon)	55	2.6	2.422×10^{-4}

Table 3.1 summarizes the flyer compositions and dimensions, where black paint is considered to be carbon black (or graphite black) since its composition is mostly black pigment made from carbon black, solvents, and resins with extra additives.

To calculate the average velocity of the flyer, a high speed camera (Phantom v711) is set up horizontally in the path of the flyer. The camera images provide information about the displacement of the flyer for each time interval. Thus, to calculate the flyer velocity, one divides the distance of displacement by interval time. Since the images are captured from the very beginning of the flight, it is reasonable to neglect air drag for possible early decrease of velocity. Further assuming negligible rotation and shrinkage of the

flyer plate, the velocity is inferred from the momentum conservation law. Equation (3.1) represents deceleration of a flyer in the presence of drag shown in the second term of the left hand side.

$$m \frac{dv}{dt} + \frac{1}{2} C_D \rho v^2 A = 0 \quad (3.1)$$

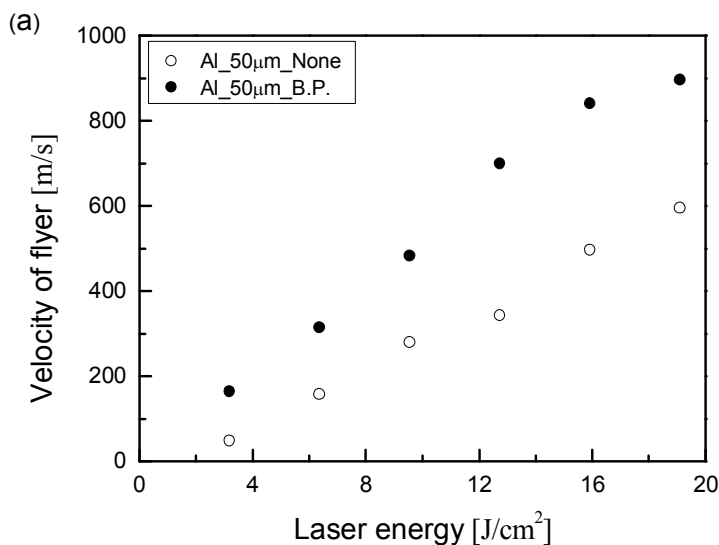
Here, m and v represent mass and velocity of the flyer, respectively, C_D is the drag coefficient, ρ is density of air, and A is frontal area of the flyer. A drag coefficient of a disk-type flyer is assumed to be 1.17 for high Reynolds numbers above 10^4 [15], because our experiment corresponds to $Re > 10^5$. Then, using all known values, Eq. (3.1) gives only a $\sim 8\%$ decrease in velocity during $10 \mu\text{s}$ after leaving the plasma region, which suggests that air drag can be neglected in the high speed camera images.

To capture the motion of a flyer, it is necessary to synchronize the release of the laser beam with the image capturing. After measuring the delay of the laser and the camera using an oscilloscope, a pulse generator was set up to capture images simultaneously with the start of the irradiation. The triggering sequence is as follows. A trigger signal goes into a flash lamp, and then a Q-switch is triggered in $200\text{--}300 \mu\text{s}$ to control the laser energy. Taking the delay of the laser output, the camera is triggered at 100 ms after firing the flash lamp. Since we set the camera to record $300 \mu\text{s}$ ahead of the trigger, it is possible to capture the initial stage of irradiation with the fixed trigger point of the camera without adjusting the triggering sequence. The flight characteristic of the flyer is successfully evaluated using the high-speed images taken at 1 million frames per second.

The error of measurement in velocity and laser fluence is as follows. 318 mJ/cm² of fluence error is noted since a single-shot mode of the laser has about 10 mJ of fluctuation. Approximately 5 % measurement error of velocity can result from the image analysis.

3.1.3 Results and Discussion

Aluminum and copper foils with/without a black paint coat were used as flyers. The velocity of a flyer is plotted as a function of laser fluence in Fig. 3.2. The black paint coat gave an average increase of 83-143 % in flyer velocity as represented in Table 3.2. Therefore, the reflectivity, required energy for laser ablation, and surface finish of the materials were investigated to figure out the effect of the black paint coat.



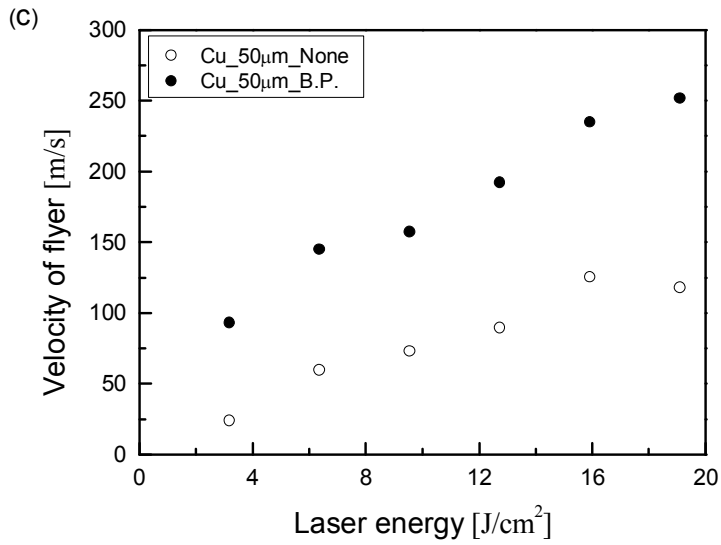
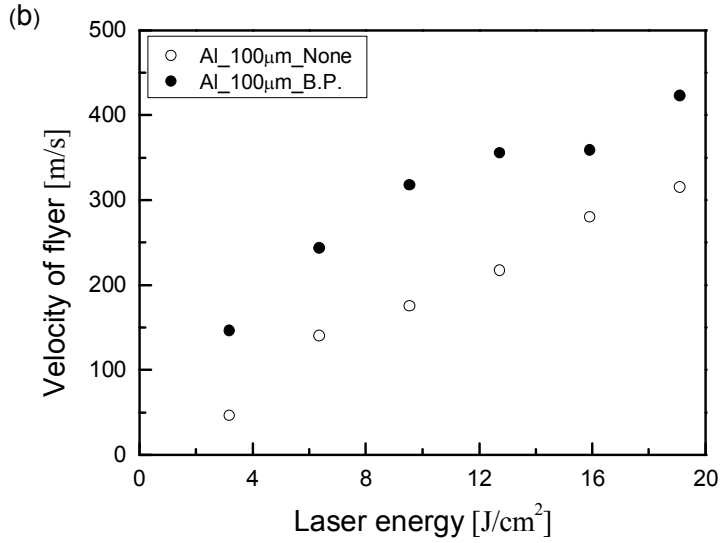


Fig. 3.2. Velocity of flyer plate: (a) aluminum_2.1 mm diameter and 50 µm thickness, (b) aluminum_2.1 mm diameter and 100 µm thickness, (c) copper_50 µm thickness and 2.6 mm diameter.

Table 3.2. Increase in flyer velocity with a black paint coating.

Laser Energy [mJ]	Velocity of Flyer Plate [m/s]								
	Thickness_50 μm			Thickness_100 μm			Thickness_50 μm		
	Diameter_2.1 mm			Diameter_2.1 mm			Diameter_2.6 mm		
	Al	Al B.P.	Increase [%]	Al	Al B.P.	Increase [%]	Cu	Cu B.P.	Increase [%]
100	49	165	236.7	46	146	217.5	24	93	287.5
200	158	315	99.4	140	243	73.6	60	145	141.7
300	280	483	72.5	175	317	81.1	73	157	115.1
400	343	700	104.1	217	355	63.6	90	192	113.3
500	497	840	69.0	280	358	27.9	126	235	86.5
600	595	896	50.6	315	423	34.3	118	252	113.6
	Average		105.4	Average		83.0	Average		142.9

As for laser irradiation onto a target surface, the laser irradiance according to depth is represented as

$$I(x,t) = (1 - R)I_0(t) \exp(-\alpha x) \quad (3.2)$$

where $I_0(t)$ is the incident laser irradiance at $x=0$, α is the absorption coefficient, and R is the reflectivity of the ablative material. Table 3.3 summarizes material properties of the metals and black paint. Since the thicknesses of both the black paint and the metal foils are much greater than the penetration depth of the laser light, $\delta = 1/\alpha$, free transmission of the

laser beam through the flyer is unlikely.

Table 3.3. Material properties.

	Aluminum	Copper	Carbon
Absorption Coefficient [cm^{-1}] [16-18]	1.18e6	8.35e5	2.40e5
Penetration depth [nm]	8.475	11.976	41.667
Reflectivity ($< 1 \text{ J/cm}^2$) [16-18]	0.95	0.97	0.05
Reflectivity ($> 10 \text{ J/cm}^2$) [19-21]	0.1~0.2	0.1~0.2	~ 0
Density_solid [kg/m^3] [22-24]	2700	8960	2267
Density_liquid [kg/m^3] [25, 26]	2385	8000	-
Molar mass [kg/kmol]	26.982	63.546	12.011
Thermal diffusivity [mm^2/s] [27-29]	97.1	117	100
Heat penetration depth [nm]	~985	~1082	~1000
Melting point [K] [30-32]	933.4	1357.8	-
Boiling point [K] [32-34]	2792	2835	-
Sublimation point [K]	-	-	3915
Heat of fusion [J/mm^3] [32, 35, 36]	1.069	1.837	-
Heat of vaporization [J/mm^3] [32, 36, 37]	25.043	38.020	-
Heat of sublimation [J/mm^3]	-	-	135.27
Heat capacity_solid [$\text{J/mm}^3\text{K}$] [26, 38]	2476e-6	3459e-6	1610e-6
Heat capacity_liquid [$\text{J/mm}^3\text{K}$] [26, 32]	2576e-6	3840e-6	-
Required ablation energy [J/mm^3]	32.534	49.280	56.121

It shows that the reflectivity of carbon is considerably lower than that of

aluminum or copper before plasma formation. Although the reflectance of Al or Cu at a fluence of over 10 J/cm² [19, 20] is set to 0.1-0.2, carbon still absorbs most of the incident laser beam without reflection; as such, R is close to zero. Therefore, higher absorption in the near-infrared region is obtained by doping of metal with a carbon layer or nanoparticles [39].

The nanosecond laser ablation is dominated by heat conduction, melting, vaporization, and ionization. When a laser beam is directed onto a target surface, the surface temperature starts to rise as the energy of a laser beam is absorbed and heat conduction produces the temperature distribution in the target. The target melts and evaporates or changes to a plasma state depending on achieved temperature. Then, the material is ablated by liquid and vapor expulsions. The process of laser ablation by nanosecond laser pulses can be described by a model based on classical laser-matter interaction [40]. In the model, all the absorbed laser energy is used to heat up the material to gas phase and to overcome latent heats of melting, vaporization, and sublimation. Heat conduction and vapor overheating are neglected. Since the heat penetration depth is given by $l \sim (D\tau_L)^{1/2}$, where D and τ_L are the thermal diffusivity of a material and the pulse duration of a laser beam, the required ablation energy per unit volume is calculated from the conservation law of energy.

$$\rho \left[c_{p,s} (T_m - T_0) + H_m + c_{p,l} (T_v - T_m) + H_v \right] = E_{pulse} / V \quad (3.3)$$

where E_{pulse} is the energy of a laser pulse and V is the ablated volume. ρ , T , c_p , and H respectively represent density, temperature, temperature, and latent heat.

heat capacity, and enthalpy of a material. The subscripts m , v , and 0 refer to properties of melting, vaporization, and reference points. s and l indicate solid and liquid phases, respectively. In the case of carbon, the parameters related to melting and vaporization in Eq. (3.3) are replaced by that of sublimation because sublimation occurs at atmospheric pressure. Material properties of the metals and black paint are summarized in Table 3.3. Here, the thermal properties of the target materials are assumed to be constant, because there is little change over a wide temperature range [41].

Compared to aluminum and copper, carbon has a low reflectivity but requires a relatively higher energy for vaporization. Therefore, the overall efficiency seems to remain constant because the increased energy for laser ablation cancels out the reduced reflectivity. However, the overall efficiency actually increases because black paint coat induces a dust explosion as compared to the rolled-anneal metal foils, allowing the rapid and strong combustion of fine carbon particles suspended in the air [42]. As a result, flyer velocity is significantly enhanced through the black paint coat.

It is common to consider system efficiency in terms of the increase of coupling efficiency, C_E , defined as

$$C_E = \frac{1}{2}mv^2 / E_L \quad (3.4)$$

Here, m and v represent mass and velocity of the flyer, respectively, and E_L is the laser pulse energy. It represents the flyer kinetic energy output per input of laser energy. Since comparison groups represent the result with flyer velocity, it is necessary to convert efficiency into velocity for correct

comparison. Then the percentage increase of flyer velocity (with and without respective coating) of reference data [8, 11, 12] can be compared as shown in Fig. 3.3. The amount of efficiency enhancement achieved by the present LDF system using an explosive absorptance layer is higher than those reported earlier. This suggests that a simple method may well circumvent multiple-layered approaches that require both expensive and time-consuming preparation before a controlled launch of a single mini flyer.

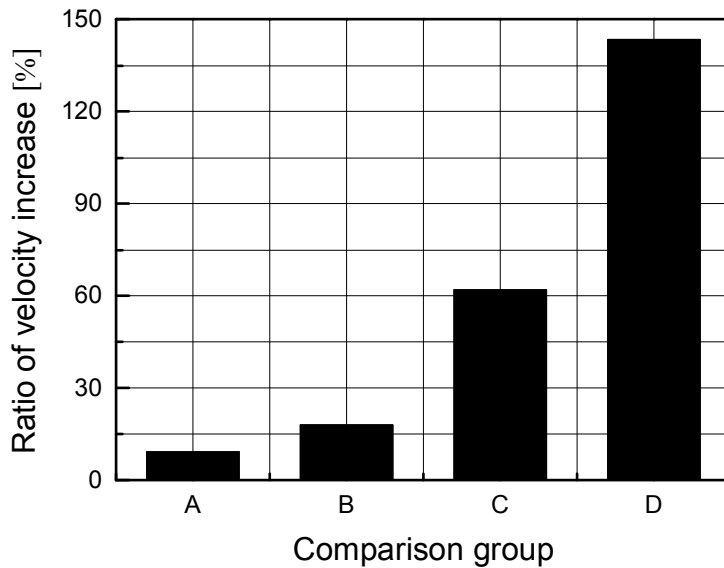


Fig. 3.3. Comparison of % increase of velocity due to respective coating: A [8], B [11], C [12], and D [This work].

When comparing aluminum and copper flyers with/without black paint coat, it is difficult to directly compare the degree of acceleration by considering only the flyer velocity because each flyer has different dimension and mass.

Therefore, the momentum of a flyer was taken into account to compare impulse by laser-generated plasma, because impulse applied to a flyer causes the equivalent change in its momentum as follows.

$$F\tau = mv \quad \text{or} \quad PA\tau = \rho Adv \quad (3.5)$$

where ρ , A , d , and v respectively represent density, area, thickness, and velocity of a flyer. P and τ are pressure and duration of plasma. The momentum of a flyer increases with its area because plasma instantaneously expands beyond the area of the flyer during laser irradiation. And it is assumed that plasma has a uniform pressure distribution because the increase ratio of momentum is proportional to that of the area.

Table 3.4 respectively represents the normalized momentum of copper of 50 μm thickness and aluminum of 100 μm thickness with/without black paint coat. Here, the momentum of a flyer is normalized by dividing by its area for direct comparison regardless of area. The momentums of aluminum and copper flyers both coated with black paint are almost similar. This is because the same impulse is applied to a flyer only by carbon plasma due the thin heat penetration depth which is much smaller than the thickness of black paint coat. On the other hand, the momentum of an aluminum flyer is larger than that of a copper flyer because aluminum requires relatively lower energy for laser ablation in spite of similar reflectivity. Therefore, the flyer velocity increase of copper according to existence of black paint coat becomes higher than that of aluminum.

Table 3.4. Increase in normalized momentum of flyer with a black paint coating.

Laser Energy [mJ]	Normalized momentum of Flyer Plate [kg/m·s]					
	Thickness_100 μm Diameter_2.1 mm			Thickness_50 μm Diameter_2.6 mm		
	Al	Al B.P.	Increase [%]	Cu	Cu B.P.	Increase [%]
	100	12.4	40.8	228.9	10.7	42.4
200	37.8	68.0	79.8	26.8	66.2	146.9
300	47.3	88.7	87.7	32.6	71.6	119.8
400	58.6	99.3	69.5	40.2	87.6	118.0
500	75.6	100.2	32.5	56.3	107.2	90.6
600	85.1	118.3	39.1	52.7	115.0	118.2
	Average		89.6	Average		148.2

The performance characteristics of the LDF system are examined according to (i) different flyer materials and coatings, (ii) diameter and thickness of the flyer, and (iii) laser pulse energy irradiated. Results from Fig. 3.4 illustrate how different materials and thicknesses of the flyer affect the velocity. Here, the velocity of the flyer increases with decrease of flyer thickness, which results in decrease of its mass. Hence, the velocity of the aluminum flyer is higher than that of copper.

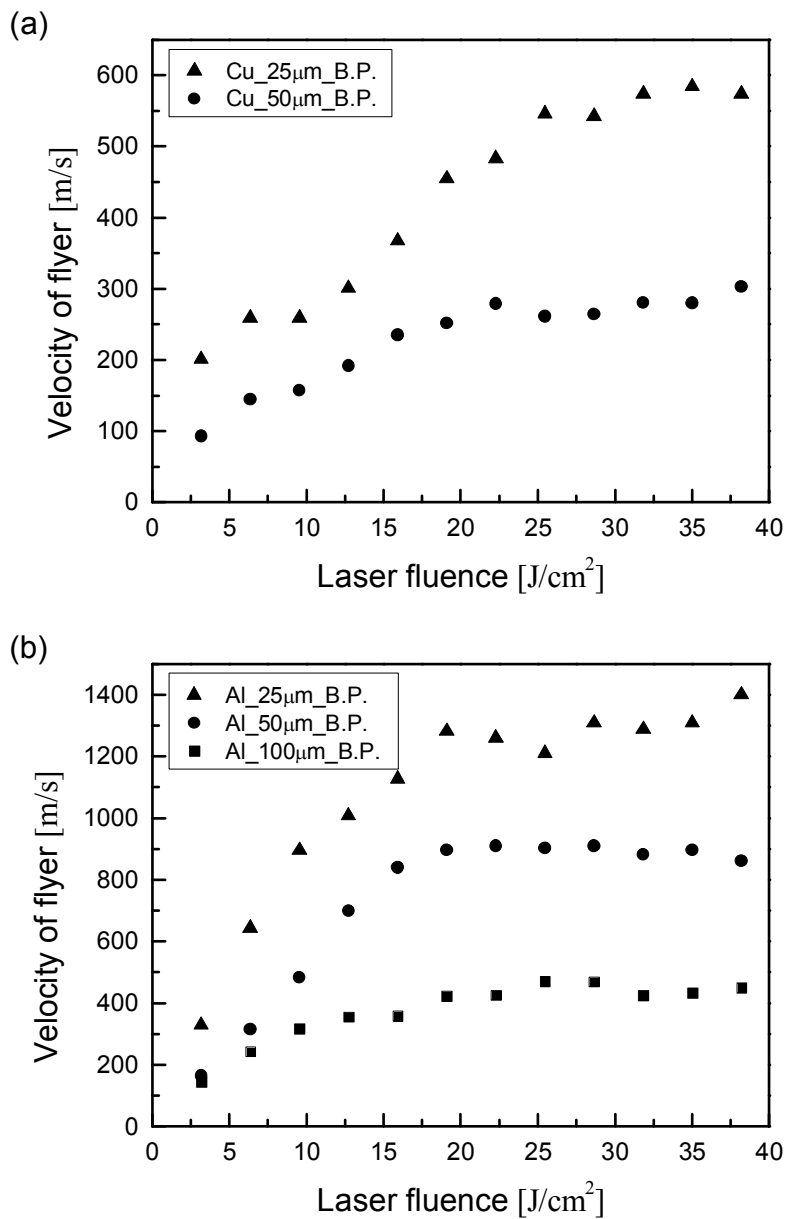


Fig. 3.4. Flyer thickness effect: (a) copper with black paint, (b) aluminum with black paint.

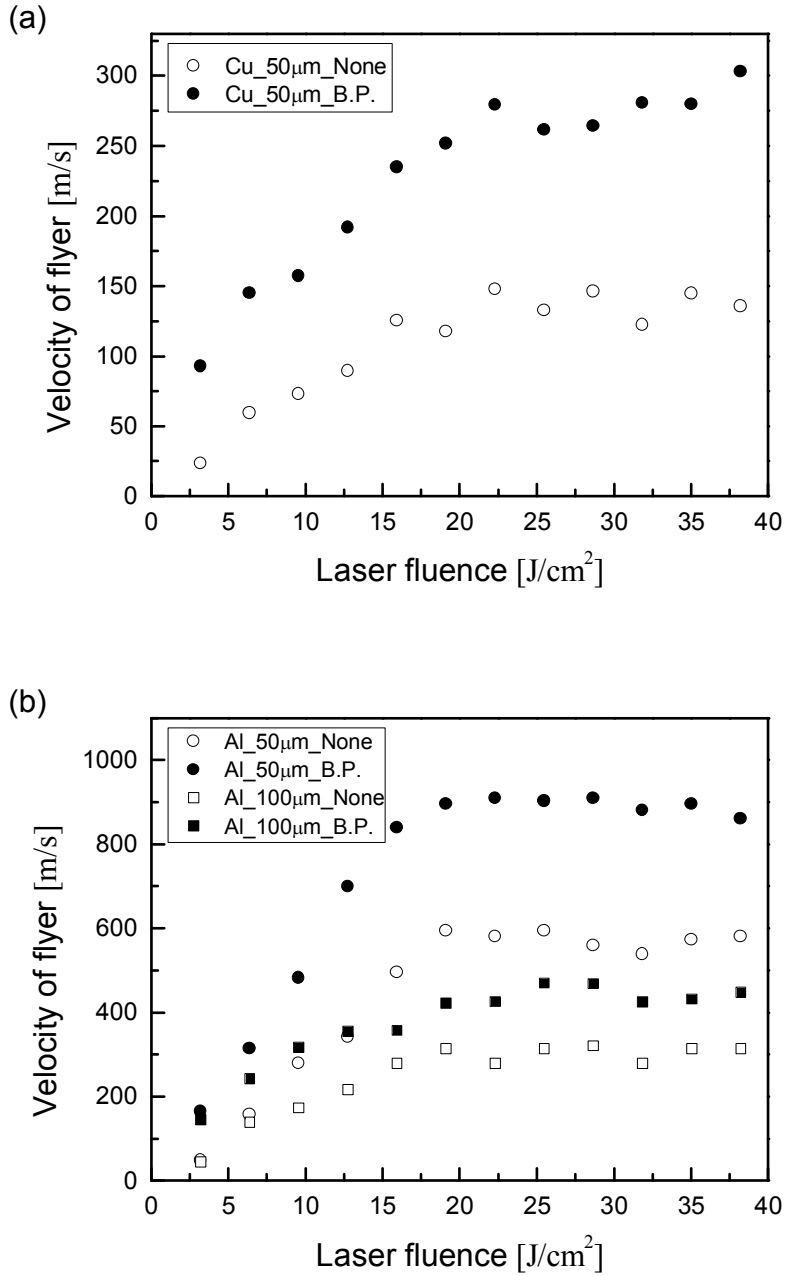
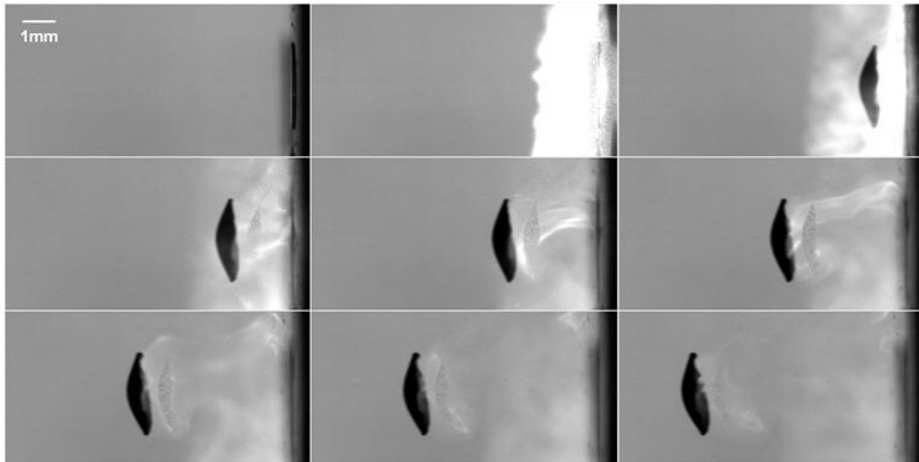
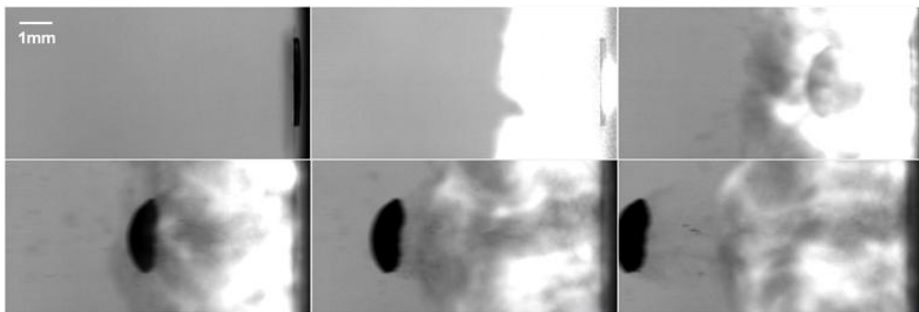


Fig. 3.5. Effect of black paint coating: (a) copper, (b) aluminum.

The effect of the black-paint coat is presented in Fig. 3.5. The terminal velocities of flyers with black paint were approximately 2 and 1.5 times the non-coated flyer for copper and aluminum, respectively. The high speed camera images make it clear why this increase of flyer velocity occurred.



(a)



(b)

Fig. 3.6. High-speed images ($6.7 \mu\text{s}$ interval time) of flyers of $50 \mu\text{m}$ thickness and 2.6 mm diameter using 1.3 J laser energy: (a) copper, (b) copper with black paint.

As shown in Fig. 3.6, both cases have similar flyer shape, bent in the middle due to Gaussian beam radiation at center. The center of the coated flyer was bent even more. The light of the plasma in black paint is much brighter, lasting longer than the non-coated flyer. The combination of black paint and acrylic confinement offered a considerable peak pressure rise for the duration approximately three times longer than the laser pulse [43], and therefore enhancement of the flyer acceleration.

The experiments were conducted by varying the laser pulse energy from 0.1 to 1.4 J, but no increase in flyer velocity was observed for energies beyond 1.2 J. Gojani et al. [44] confirmed that the ablated depth increases with increasing laser irradiance until a specific threshold is reached. After that, it decreases due to plasma shielding. Hence, blow-off products decrease, resulting in a further decrease of the thrust or the flyer velocity. Absorption or transmission of a transparent substrate, acrylic, also shows nonlinear characteristics as the substrate undergoes structural change (damage) by the high irradiance [45].

It is also noted that around 50 % of the flyers break randomly at laser energies above 1.4 J. Due to such randomness in fragmentation, precise measurement of the flyer velocity often becomes challenging. Figure 3.7 is evidence of such a notion showing a ‘thin’ (15 μm thickness) aluminum flyer upon random fragmentation during flight. The breaking of the flyer creates a plume of micro particles which limits flyer diameters to be within a few hundred μm .



(a)



(b)



(c)

Fig. 3.7. Random fragmentation of ‘thin’ (15 μm thick, 2.1 mm diameter) aluminum flyer with black-paint coating at 0.6 J laser energy: (a) 10 μs , (b) 20 μs , and (c) 30 μs after irradiation.

The fastest particle velocity, however, can be measured as shown in Fig. 3.8 with a range of scatters. Thus, further effort is necessary to allow as good of a control as in the earlier cases of ‘thicker’ plates over the flight path at speeds above 2.2 km/s using a higher laser energy. It is important to control fragmentation of the flyer such that its size and velocity remain predictable for advancing the current state of LDF research in various flyer impact applications.

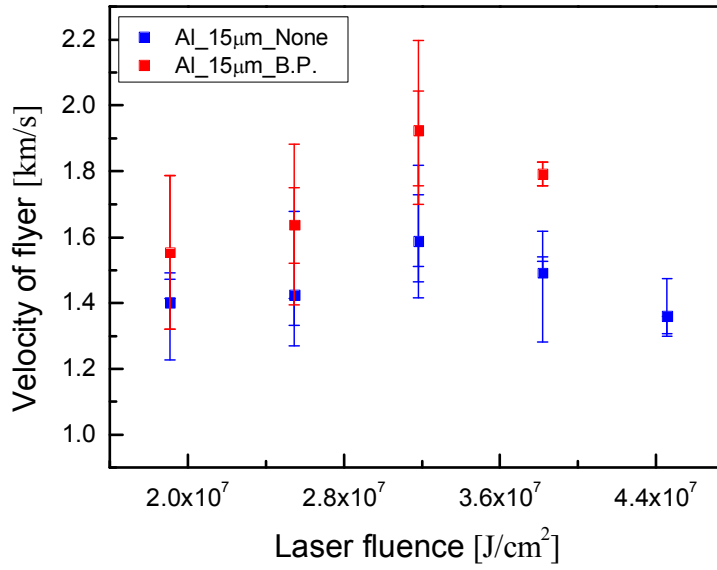


Fig. 3.8. Fastest particle velocity measured for ‘thin’ aluminum flyer of 2.1 mm diameter and 15 μm thickness.

3.2 High Velocity Impact by Laser-Driven Flyer

3.2.1 Background and Motivation

In the past, high-speed collision with ice particles entrained with the ambient air was thought to be benign to aircrafts. However, it has been known that even micro-scale ice particles cause significant damage to jet engine inlet blades [46]. Under the influence of frequent high-speed impact loading, incipient crack can be formed on the target surface and propagate, which induces significant decrease of life time of exposed component parts [47]. Deposition of frozen ice changes the flow path thorough the turbine blade, which affect heat transfer to surfaces protected by cooling [48]. The performance degradation, such as flight instability and power loss of jet engine, induced by the related erosion and deposition represents that a jet engine is always exposed to danger of frozen ice impacts at high-speed. Therefore, a careful experimental reproduction of such effect of high-speed collision with ice particles is desired for understanding the high strain rate phenomenon of target under extreme particle impact conditions [49].

Available techniques for accelerating an object to a high velocity fall into one of the three conventional categories [3]: gas (or powder) guns, electric (or rail) guns, and less commonly, laser-driven systems [4, 5, 50]. Gas gun is usually massive and cannot readily apply to free standing micro-scale thin flyer. Electric gun is suitable for a non-conducting flyer plate. If a conducting flyer has to be mounted, at least a dielectric is needed to be located between the launch pad and a conducting flyer plate. Unlike these gun-type

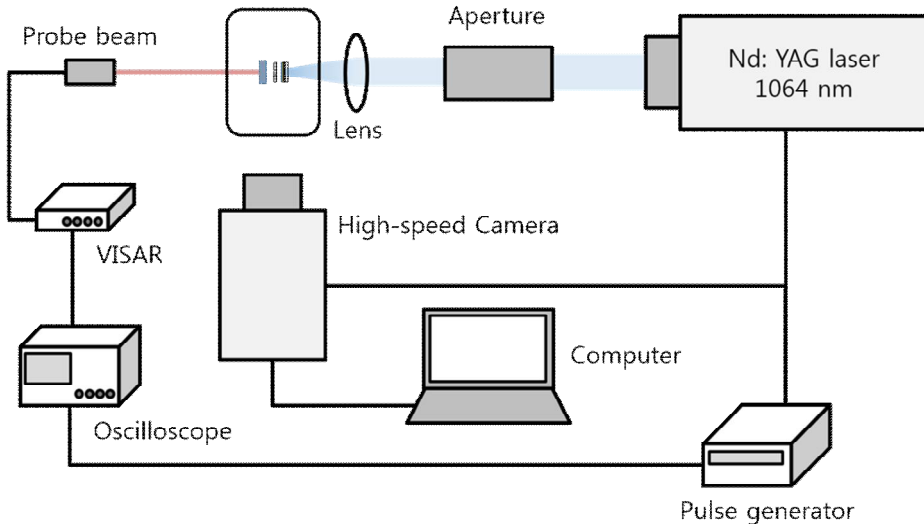
acceleration techniques, the laser based method has several advantages: the system scale is much smaller, and a little momentum or energy is all that is required. Moreover it requires low cost per shot and can offer highly repetitive experiment in a short time. For these reasons, the laser-based acceleration is a suitable technique for a high speed impact experiment of small flyer objects.

In our work, a laser-driven system was designed to accelerate micro-scale ice particles to velocities up to Mach 2 using a Q-switched Nd:YAG laser beam at 100-600 mJ with 1.064 μm wavelength and 9 ns pulse duration. The high speed images (Phantom v711) and double exposure shadowgraphs were used to measure the average velocity of the ice particles and their deceleration. The Velocity Interferometer System for Any Reflector (VISAR) was also constructed to measure free surface velocity of a metal foil, which presents interfacial interactions between ice particles and metal foil. The particle velocity of ice and free surface velocity of metal foil are determined in terms of the laser energy. Using a 3D Optical Surface Profiler (Nanofocus μsurf), the dimensions of craters by the high-speed impact were measured which is expected to shed light on the effects of moisture particle collisions on the jet engine inlet system.

3.2.2 Experimental Approach

Using a Q-switched Nd:YAG laser, water ice particles were accelerated to

speeds approaching Mach 2 at 100-600 mJ with 1.064 μm wavelength and 9 ns pulse duration. The schematic view of experimental setup is shown in Fig. 3.9. The laser beam was directed through an aperture of 6 mm diameter for a flat-top spatial beam profile, a long pass filter for blocking the flash lamp light, a focusing lens, and then onto the rear side of a launcher composition. A spot diameter of 1.73 mm was obtained by placing the front of a launcher approximately 69 mm apart from a 100 mm focal length of plano-convex lens. Such a long length focal lens was used to decrease the tolerance of a spot diameter coming from a very small location change of a launcher. A high-speed camera (Phantom v711) were placed perpendicular to the path of the laser beam to capture the motion of ice particles. Additionally, VISAR was used to measure free surface velocity of a metal foil.



(a)

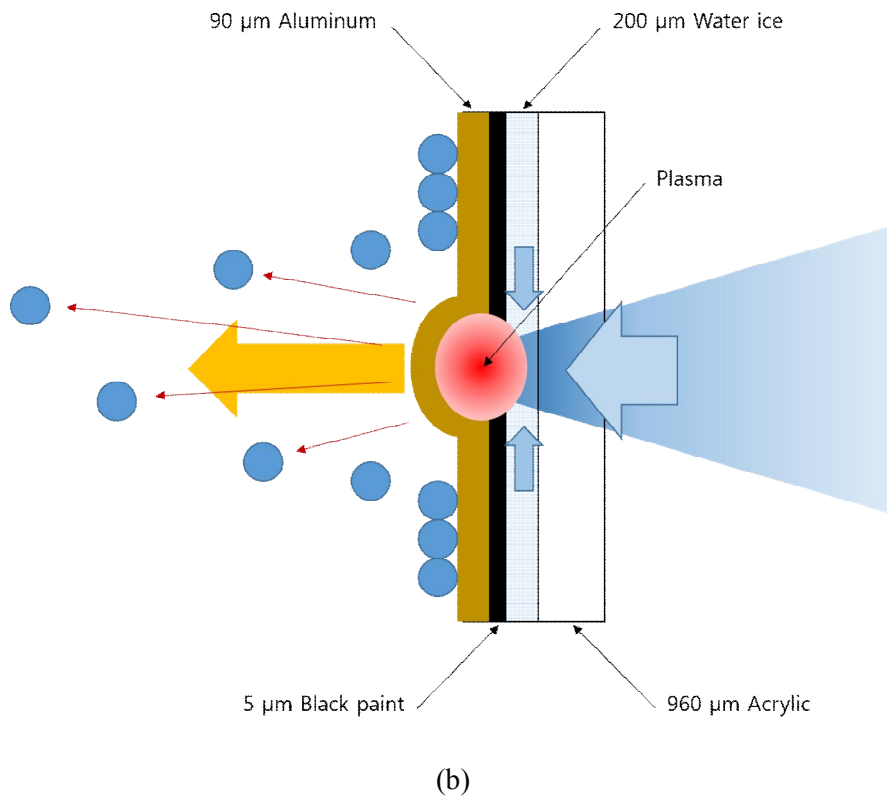


Fig. 3.9. (a) Schematic view of experimental setup and (b) Launcher configuration.

When a laser beam of high irradiance exceeding 10^{10} W/m^2 is focused onto a metal foil, energy of the laser beam is deposited in a few skin depths of the ablative material, and then a small fraction of the metal surface experiences rapid temperature rise accompanied by an explosive phase change to a plasma state. This surface evaporation generates recoil pressure and momentum [7], which are confined between metal surface and transparent substrate and subsequently expand towards the opposite direction of a laser beam while

deforming the metal foil in form of a dome. The ice particles are accelerated to a high velocity by the rapid deformation of the metal and then fly as they are detached from the metal surface.

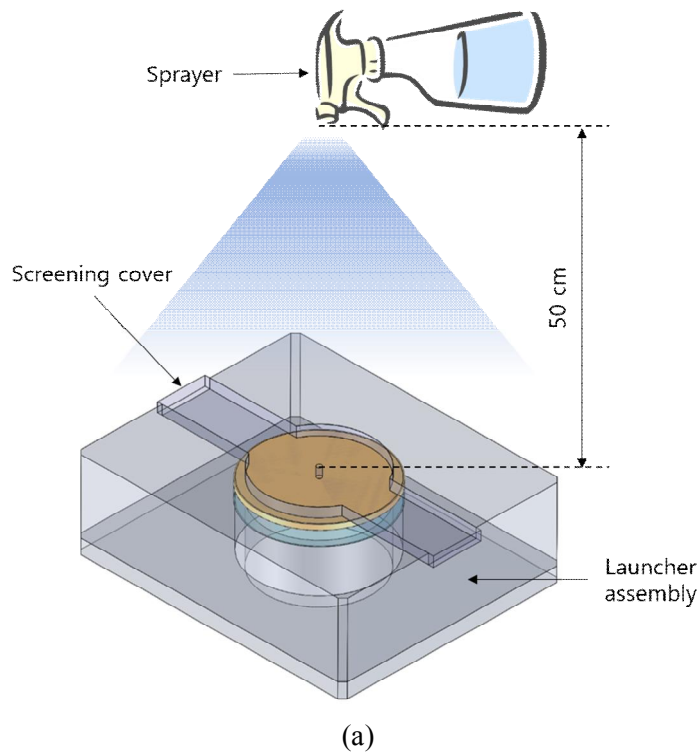
Table 3.5. Launcher composition.

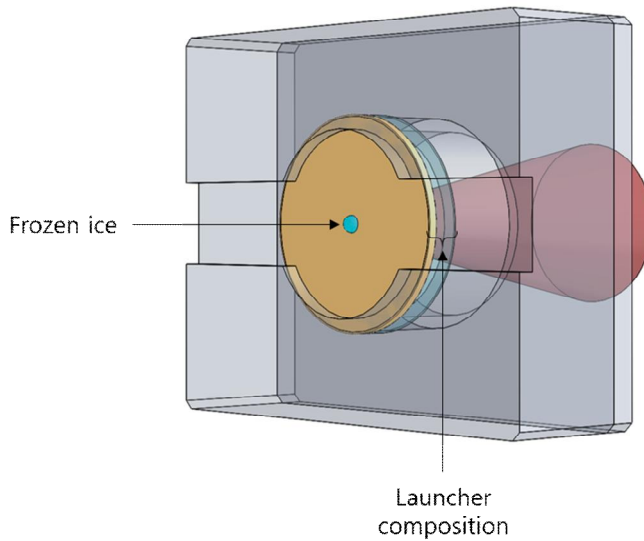
Layer	Material	Thickness [μm]
Insulation/Particle holder	Aluminum	90
Absorption/Ablation	Black paint (carbon)	5
Additional confinement	Water ice	200
Transparent substrate	Acrylic	960

The present acceleration system is composed of a launcher consisting of multi-layers of materials for making use of each layer and its assigned role. Its composition and dimension are summarized in Table 3.5. The first layer is a transparent substrate which is adopted to make the plasma pressure higher by confining the ablative materials between the metal foil and transparent substrate. Here an acrylic is used as a transparent substrate because of its high (over 90 %) transmittance for 1.604 μm wavelength. The second layer is water ice that offers an additional confinement effect by preventing plasma leakage by filling up the cavity between the metal surface and the transparent substrate. Also, it works as a low temperature heat reservoir for keeping the ice particles from melting at room temperature. The third layer is black paint coating that is used as absorption/ablation layer. This layer absorbs the incoming laser energy at a minimum reflection and can be easily vaporized

for generating a strong recoil momentum. The last layer is a metal which is applied to protect the ice particles from the possible melting [8, 11, 51].

Installation of the ice particles on a launcher is an important process in using the present laser-driven accelerator. When a launcher assembly is ready to use, a metal foil is initially covered with a screening cover having a hole at its center with a diameter of 1.5 mm. Next, the water droplets are vertically sprayed ten times with a sprayer that is approximately 50 cm away from the launcher assembly as shown in Fig. 3.10, from which only a very small amount of water droplets are localized at the center spot of ablation.





(b)

Fig. 3.10. (a) Installation of ice particles on the launcher, (b) Small amount of ice particles located at the ablation point of the launcher.

Next the launcher assembly with a screening cover and a small amount of water droplets is frozen for one hour at about 240 Kelvin in a refrigerator. One hour later, the launcher assembly is mounted on the laser-driven system after removing the screening cover. The experiment is conducted within 10 seconds as the launcher assembly is now exposed to a room temperature.

To calculate the velocity of ice particles, a high speed camera (Phantom v711) was placed perpendicular to the path of the laser beam. The positions of ice particles after launch are inferred from the camera images, and their velocities are calculated by dividing the displacement by time interval of consecutive pictures. The high speed camera has the limitation that deceleration of the ice particles by air drag is commonly not witnessed in the

high-speed images whose time interval is on the order of a micro second. Therefore, we have used a double exposure shadowgraph to check the possibility of deceleration of the ice particles at the very early stage of acceleration. The double exposure shadowgraph setup for visualizing the flight motion of ice particles is shown in Fig. 3.11.

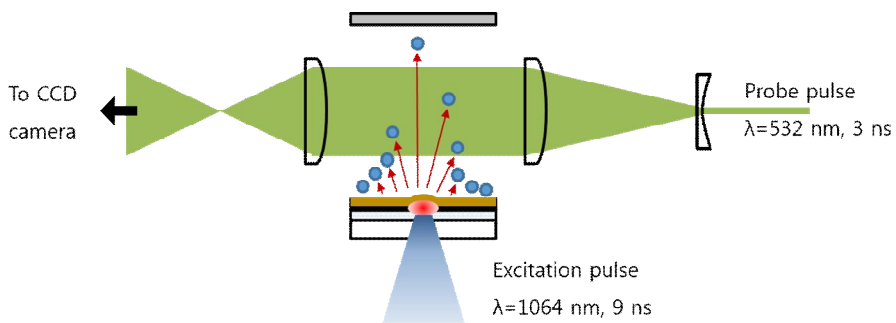


Fig. 3.11. Schematic view of double exposure shadowgraph.

The double exposure laser system is the Continuum Minilite which contains two laser heads. Two 1064 nm fundamental Q-switched Nd:YAG laser beams meet at the dielectric polarizer by using mirrors for each laser for optimized overlap and share a common optical path, passing through a single doubling crystal. 532 nm dichroic mirrors separate the two output pulses from the residual 1604 nm beam. Here, output beams have 532 nm wavelength and 3 ns pulse duration, and its time interval between the two pulses vary from 40 ns up to 100 ms. The probe beam for shadowgraph imaging is aligned perpendicular to the flight motion of ice particles. The collimated beam obtained by traveling across concave and convex lenses passes through the test section, and then focused in front of a CCD camera to acquire a focused

shadowgraph. A neutral density filter is applied ahead of the camera to avoid damage on a CCD sensor.

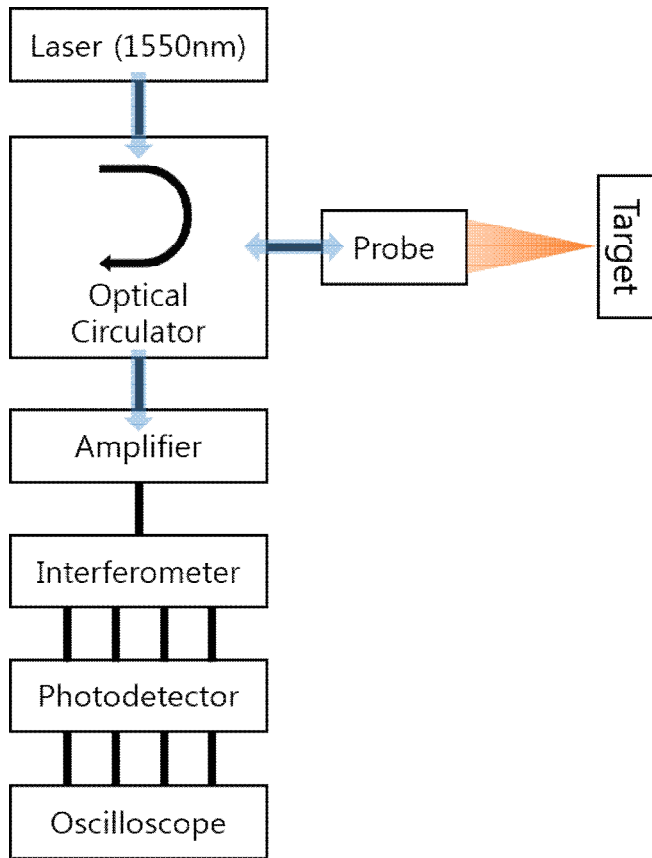


Fig. 3.12. Schematic view of velocity interferometer system for any reflector (VISAR).

Figure 3.12 shows the VISAR [1, 2] configuration used in the experiment. Here, an ultra-narrow line width (<20 kHz) semiconductor diode laser was used, operating at 1550 nm with a power of 5 mW, to minimize any signal broadening. The probe beam is focused onto a target surface of interest,

whose velocity is to be measured, and then reflected from the target surface. The returning beam, passing through a band pass filter, is directed to the interferometer which is a delay leg, Mach-Zehnder type. Four output signals from Quadrature Push-Pull interferometer are split by a polarizing beam splitter. The intensities of four outputs are converted to electric signal by four 10 GHz fiber coupled photodetectors and then recorded by a digital oscilloscope.

Based on the Rankine-Hugoniot relations and elastic-plastic deformation of the material, the longitudinal stress σ_x is approximated as follows [52].

$$\sigma_x = \begin{cases} \rho_0 C_{el} u & (< P_H) \\ \rho_0 D u + \frac{2}{3} Y_0 & (> P_H) \end{cases} \quad \text{where} \quad \begin{cases} P_H = \left(1 + \frac{\lambda}{\mu}\right) Y_0 \\ D = C_0 + S u \end{cases} \quad (3.6)$$

Here, Hugoniot elastic limit of the solid material P_H represents the point where an entirely elastic state changes to an elastic-plastic state due to strong shock wave. λ and μ are the Lamé constants and Y_0 is the compressive yield strength. u , D , C_{el} , and C_0 respectively represent the particle velocity, the shock wave velocity, the elastic wave velocity, and speed of sound. ρ_0 is density before shock compression and S is a characteristic material constant. According to the free surface approximation [53], the resulting free surface velocity u_f is about twice as fast as particle velocity u which is measured by VISAR. The following values are used to calculate the longitudinal stress of shock wave in aluminum: $\rho_0 = 2700$

kg/m³, $C_0 = 5092$ m/s, $C_{el} = 6451$ m/s, $Y_0 = 200$ MPa, $S = 1.34$, $\lambda = 60.49$ GPa, and $\mu = 25.93$ GPa.

In order to obtain proper measurement at the high speed regime, it is necessary to synchronize all the equipment using a delay generator. The triggering sequence as used is as follows. A flash lamp of driving laser was first triggered at 100-250 μ s before Q-switching to control the laser energy. A high-speed camera was triggered at 10 μ s before Q-switching with a wide margin to include the time interval between each image. For a double exposure shadowgraph, the first probing pulse was irradiated 1.2 μ s after excitation pulse and then the second pulse was fired in 200 ns to measure very early stage of acceleration. The probe laser was operated in low energy mode to avoid CCD camera damage, and its delay time between flash lamp and Q-switch was 140 μ s. An oscilloscope to record the VISAR signals is synchronized with the point of driving laser irradiation.

To figure out the effect of collision by ice particle at high velocity, Al foil of 18 μ m thickness was used as a target which is placed at 3.3 mm from a free surface of the launcher. Drag is negligible since impact time scale is too short to take considerable effect in this range. The overall diameter of the ice particles was approximately 40 μ m and randomly varied in the range of several micrometers. The dimension of the craters by impact of ice particles are measured by a 3D Optical Surface Profiler (Nanofocus μ surf), which has 1.5 mm of maximum vertical measurement range and 20 nm of vertical resolution. Fig. 3.13 shows cross-sectional view of a crater. The diameter and depth are represented as a function of the velocity of ice particles.

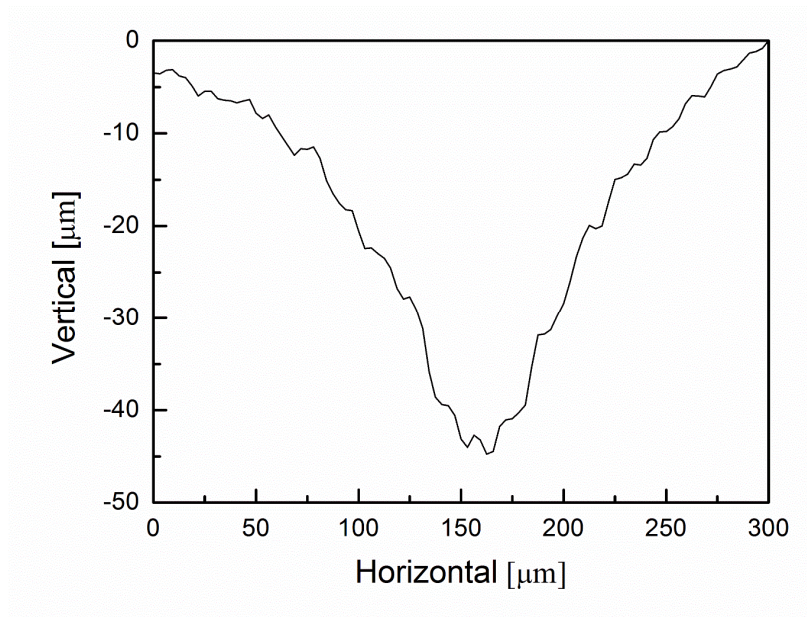


Fig. 3.13. Cross-sectional view of a crater formed by collision of an ice particle at the velocity of 198 m/s.

Here, the velocity of ice particles and free surface velocity of the metal foil are determined as a function of laser energy. Results of the above two techniques can have approximately 10% error in the measurement of velocity from the image analysis. Approximately 4.727×10^7 W/cm² of irradiance deviation was considered, because a single pulse has about 10 mJ of energy fluctuation.

3.2.3 Results and Discussion

It is important to consider flight characteristics of ice particles for

describing the performance of the laser-driven accelerator. Fig. 3.14 shows the flight motion of ice particles captured by a high speed camera. Since ablation spot is a small part of the entire acceleration area, ice particles fly in the shape of a cone, and a non-uniform acceleration occurs. However, a small amount of ice particles on the ablation spot can be uniformly accelerated in the horizontal direction. The velocity of ice particles is calculated on the basis of a front surface of the fastest cluster. In the high speed images, deceleration of ice particles by the air drag was not witnessed within an order of mm length scale. Therefore, we have used a double exposure shadowgraph to check the possibility of deceleration of particles at the very early stage of acceleration.

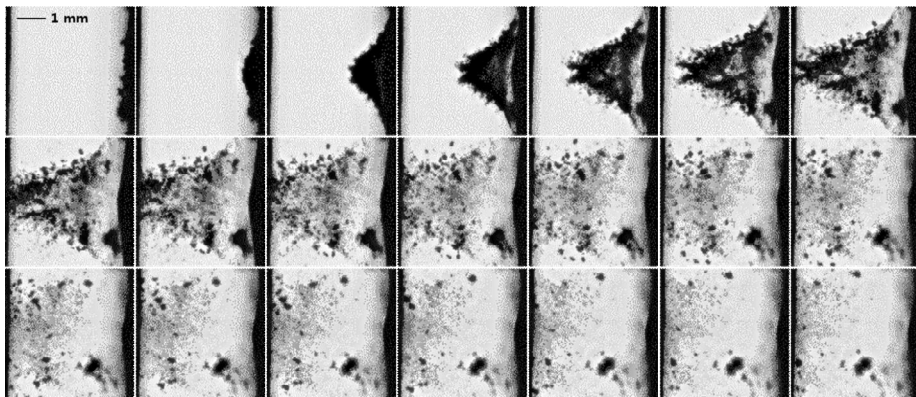
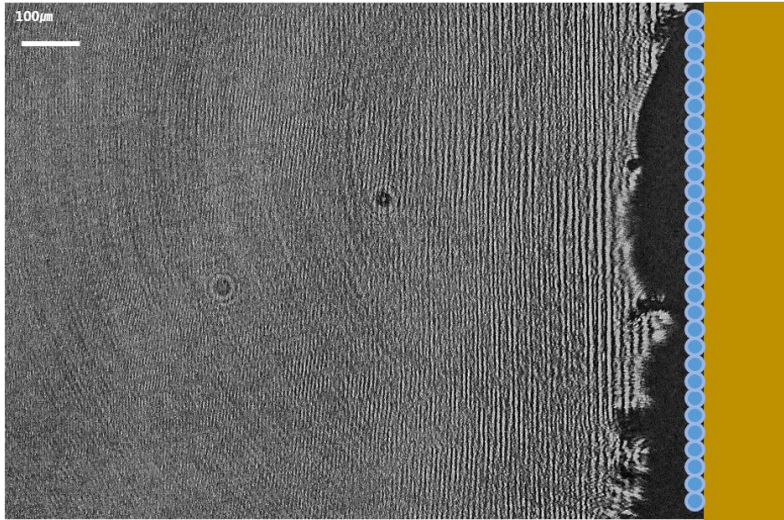
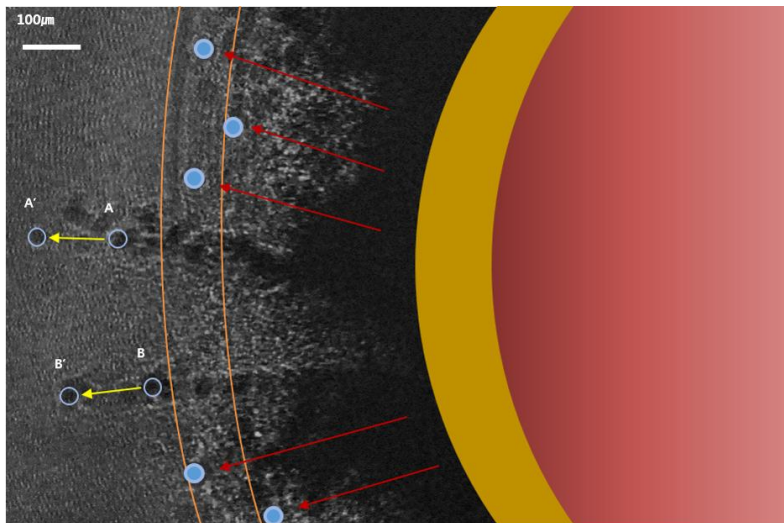


Fig. 3.14. High-speed images ($4.75 \mu\text{s}$ time interval) of ice particle using 500 mJ of laser energy.

As shown in Fig. 3.15, two shock waves and multiple pairs of ice particles exist in the image due to 200 ns time interval of the double exposure.



(a)



(b)

Fig. 3.15. Double exposure shadowgraphs by 200 ns of exposure interval using 500 mJ of laser energy: (a) reference image before the laser irradiation and (b) flight motion of ice particles after the laser irradiation.

It represents ice particles and shock wave that move away from the metal foil, including the information of the moving distance of an ice particle and its time of interval. From this shadowgraph, we found that no significant deceleration was detected when ice particles overtook a shock front in our range of tested velocity.

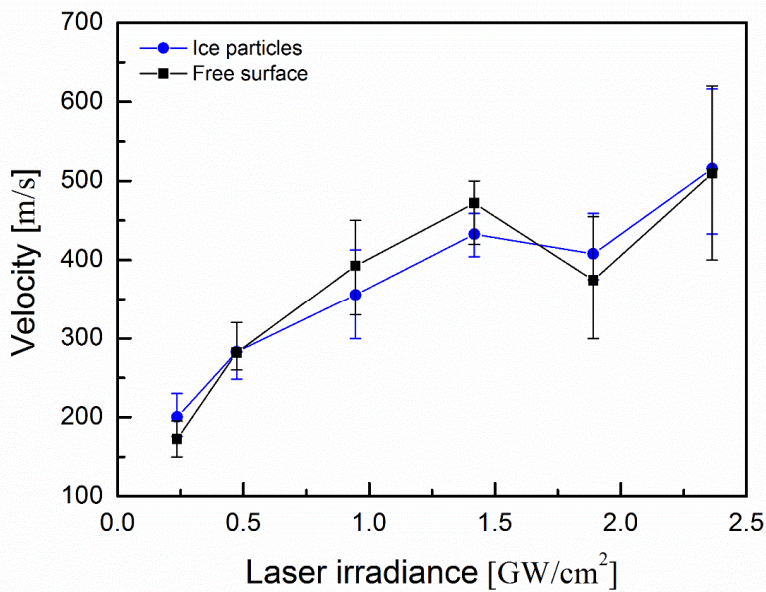


Fig. 3.16. Performance map of laser-driven accelerator: circular and square symbols represent velocity of ice particles and free surface velocity of metal foil, respectively.

The performance map of our laser-driven accelerator is represented in Fig. 3.16. Circles and squares represent the velocity of ice particles and the free surface velocity of a metal foil, respectively. The velocities are increased

nearly proportional to the laser irradiance until 1.418 GW/cm^2 . However, there was a sudden velocity drop at 1.891 GW/cm^2 and increases again at 2.363 GW/cm^2 of the laser irradiance.

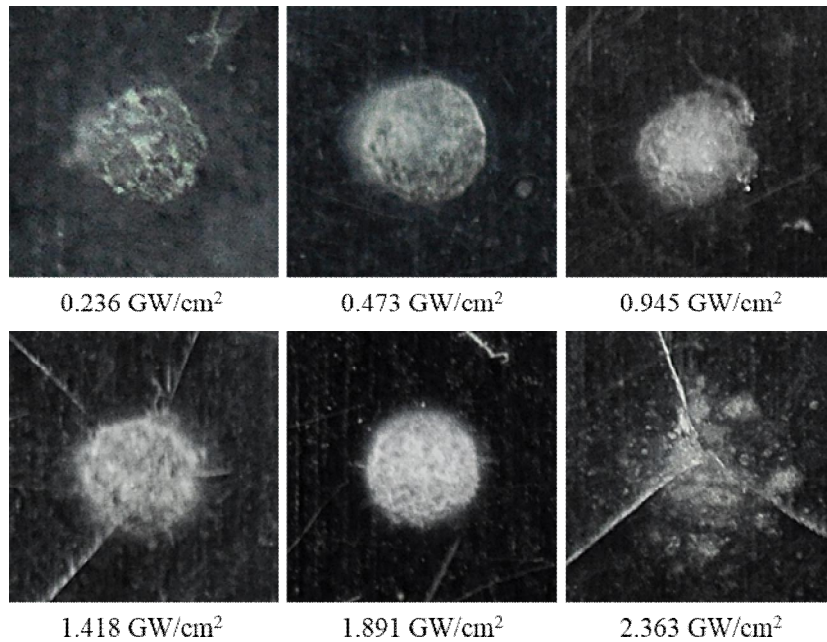
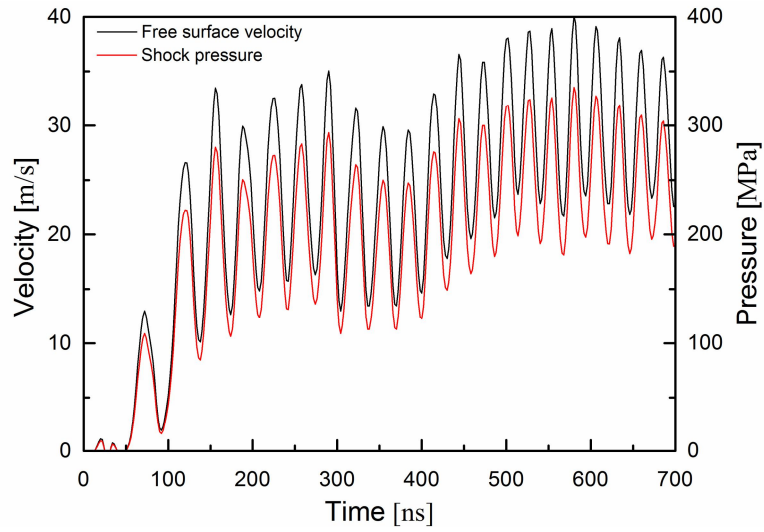


Fig. 3.17. Damaged acrylic substrate per laser irradiance. The opacity of damaged area and cracks are induced by light absorption of an acrylic substrate and the recoil momentum of plasma, respectively.

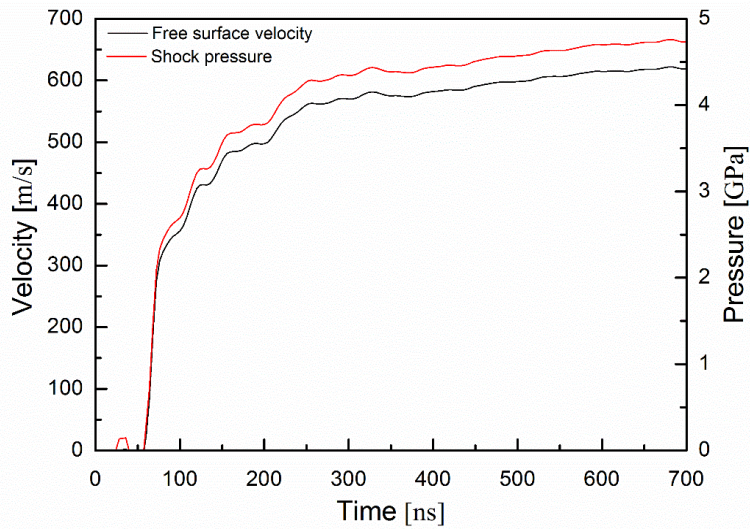
As evidenced from a sudden velocity drop, damages of an acrylic substrate for varying laser irradiances are shown in Fig. 3.17. The opacity of damaged area and cracks are induced by the light absorption of an acrylic substrate and the recoil momentum of plasma, respectively. Cracks occurred at 1.418 GW/cm^2 while nothing occurs at 1.891 GW/cm^2 as shown by the opaquely damaged

center spot. This suggests that high opacity or low transmission causes attenuation of the recoil momentum and ultimately gives rise to a sudden velocity drop. However, cracks occur again at 2.363 GW/cm^2 showing a higher transmission than that of 1.891 GW/cm^2 case. This is because a transparent polymer such as acrylic in the present experiment is influenced by the threshold process [45]. Above a certain irradiance, a sudden drop of transmission of laser beam occurs due to various forms of damage [41]. Moreover, the absorption of the short-pulsed laser in picoseconds to nanoseconds, becomes nonlinear as the substrate undergoes a structural change in the high irradiance regime [54]. The significance of the drop suggests that the performance map of our laser-driven accelerator is not linear at high irradiance regime. Thus the optical properties of a transparent substrate such as transmittance and damage threshold are important design variables that determine the working range of laser irradiance and velocity. The overall tendencies of these two velocities are similar to each other, which means that velocity of ice particles is related to the free surface velocity of a metal foil, suggesting that ice particles are detached from the metal surface and they fly at the free surface velocity of a metal foil.

Figure 3.18(a) shows a typical pressure profile and free surface velocity obtained from the direct ablation. The oscillation of pressure is induced by reflections of the shock and the release waves from the back and front surfaces of the aluminum foil.



(a)



(b)

Fig. 3.18. Velocity history of free surface of metal foil and longitudinal stress profile of shock wave at 500 mJ laser energy: (a) direct ablation, (b) multi-layered (launcher composition) ablation.

The time interval between each pressure peak has the same order with the

time calculated by dividing the thickness of the foil by a speed of sound. Here, shock wave decay may be neglected because a very small ratio of thickness to a spot diameter of the foil suppresses two dimensional smoothing effects by the propagation and reflections of the waves. The free surface of the foil was rapidly accelerated within 200 ns and then slowly reaches the maximum velocity until about 700 ns from the start. The peak pressure in two orders of MPa and the maximum velocity in an order of m/s were achieved by the direct ablation. In our laser-driven accelerator, the launcher composition consisting of the multi-layers was used, and its pressure profile is represented in Fig. 3.18 (b). The tendency of acceleration, such as free surface velocity and pressure according to time, is similar to that of a direct ablation, except that it has one order of magnitude improvement.

The velocity of ice particles and the free surface velocity of the material are represented as functions of the peak pressure in Fig. 3.19. Dot denotes experimental result which is represented with the maximum and minimum deviations in y-axis and standard deviation in x-axis. The solid line is the theoretical result obtained from Eq. (3.6) and the free surface approximation [53]. The velocity of ice particles is in good agreement with the theoretical free surface velocity, from which one can conclude that the metal foil is rapidly deformed by the laser-generated plasma pressure, and the ice particles are simply detached from the free surface velocity of the deforming metal surface. This shows the required pressure to achieve desired velocity of the ice particles in the operating range of the present laser-driven system.

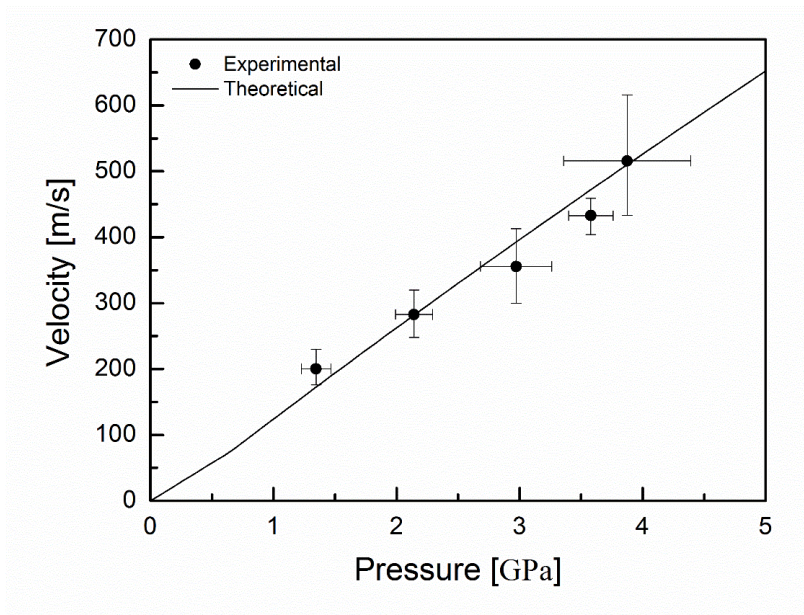
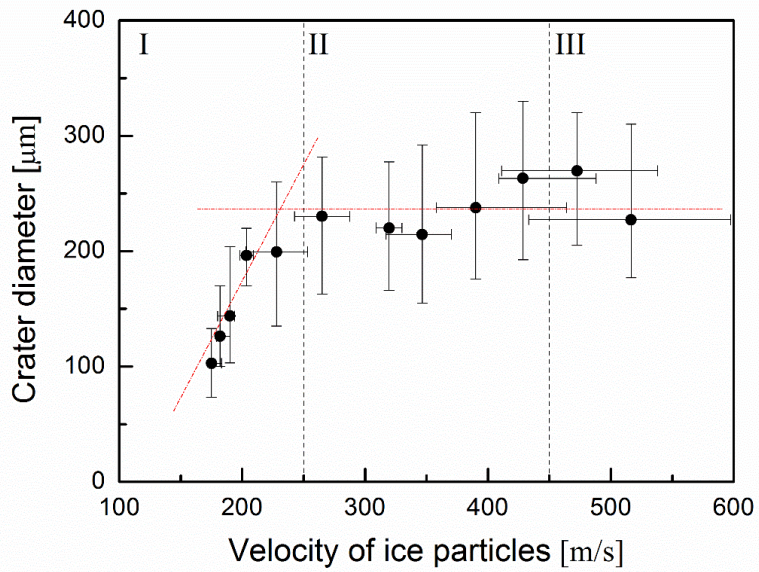
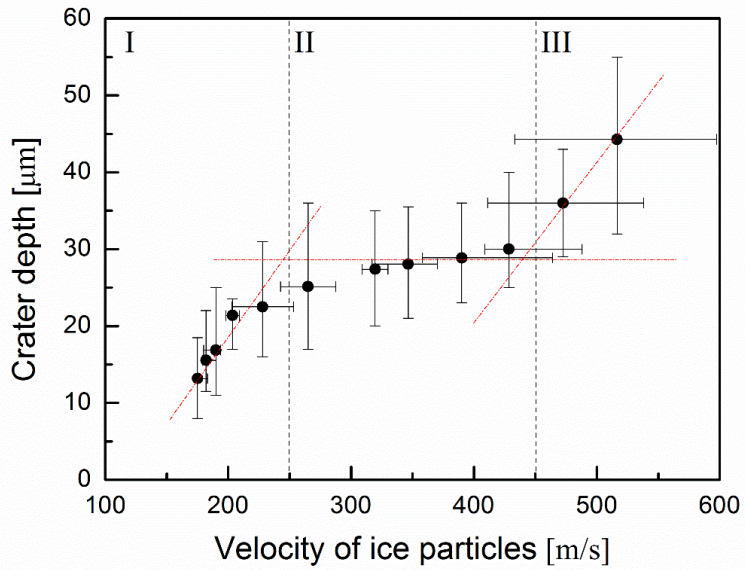


Fig. 3.19. Velocity of ice particles as a function of peak pressure of the longitudinal wave.

The resulting crater shape is casted into its diameter and depth under the impact velocity and separated into three (I, II, and III) regions. In Fig. 3.20(a), the crater diameter formed by impact increases with increasing velocity in region I and then reaches a plateau in region II with almost no change in diameter. Likewise, the crater depth follows the diameter in regions I and II until it starts to increase in region III as shown in Fig. 3.20(b). Oka et al [55] also showed the average contact pressure (impact energy divided by crater volume) in three distinct regions of impact velocity similar to our Fig. 3.20. In region I of their result, a constant pressure suggests that crater volume (diameter and depth) increases with increasing impact energy.



(a)



(b)

Fig. 3.20. Dimension of crater: (a) diameter, and (b) depth.

This is consistent with our result in Fig. 3.20 where both crater depth and diameter increased in region I. In region II of their result, the pressure increase suggests that the crater volume change is quite small, which is also consistent with the region II of Fig. 3.20 where the crater shape remains unchanged. Finally, region III of their result shows a sudden drop in pressure suggesting that the crater volume increased noticeably. Our region III in Fig. 3.20 also shows an increasing depth with constant diameter, suggesting an overall volume increase. Though the comparison between our results and those of Ref. [55] is qualitative, despite the difference in the experimental conditions (projectile, target, impact velocity, size, etc), the overall trends in Fig. 3.20 are consistent and explainable.

Chapter 4. Analysis of Micro Shock Waves in Solids

4.1 Evolution and Decay of Laser-Generated Shock Waves

4.1.1 Background and Motivation

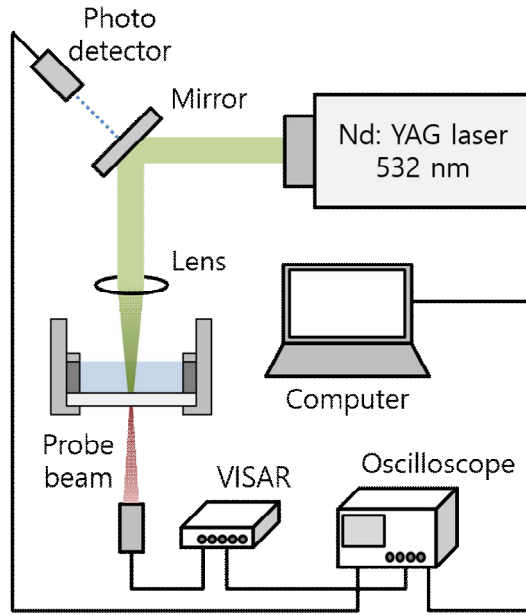
The performance of a pyrotechnic device that consists of donor/acceptor pair separated by a bulkhead or a metal gap relies on shock attenuation in the metal and shock sensitivity of the energetic materials. When shock wave emerges from a detonating donor, the amount of reflection and transmission of the shock waves at the interfaces of donor/bulkhead and bulkhead/acceptor is determined by the acoustic impedance of these materials. The transmitted shock wave starts to decay along the path of propagation in the bulkhead; if the shock pressure is higher than the initiation pressure of an acceptor, then acceptor is triggered. Thus the shock sensitivity of acceptor must be known along with the critical thickness of bulkhead in an effort to optimize the system [56, 57]. In order to address the rising demand for miniaturized pyrotechnic devices, the study on shock initiation sensitivity of small scale gap configuration is necessary. The gap thickness less than a millimeter and how the pressure is attenuated through the gap must be understood precisely.

In this research, therefore, a laser-based system is designed to send shock waves into a 304 stainless steel using a Q-switched Nd:YAG laser operating at

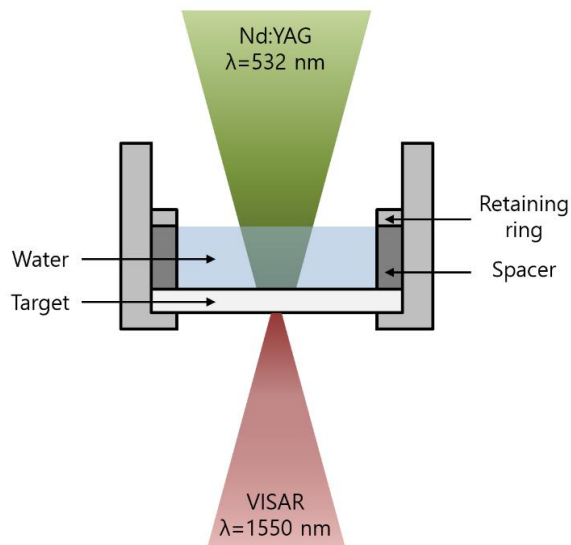
532 nm wavelength with pulse energy up to 400 mJ and 5 ns pulse width. To achieve high-pressure shock wave for a given energy, laser plasma is generated under a water confinement regime (WCR) [43]. Free surface velocity of a target is measured by making use of a velocity interferometer system for any reflector (VISAR). By varying the thickness of a target, shock pressure is determined in terms of the distance of wave propagation. Analytical models for plasma generation in a confined geometry and for formation and attenuation of shock waves is also performed to understand the behavior of the shock wave inside of a target. The shape and amplitude of the laser-driven initial pressure load and its attenuation pattern in the gap are controlled for targeting the microscale propagation distance and subsequent triggering pressure. Therefore, the miniaturization of pyrotechnic device is investigated from the present laser-based system.

4.1.2 Experimental Approach

Shock waves in orders of GPa are generated by a Q-switch Nd:YAG laser (Spectra, Lutronic Corp.) with 100-400 mJ at 0.532 μm of wavelength and 5 ns of Gaussian pulse. Fig. 4.1 depicts the schematic view of experiment setup and target assembly. The laser beam travels through a Nd:YAG mirror, a focusing lens, water confinement, and arrives at the front side of the target. When a laser beam is irradiated on the target surface, target material within a few skin depth is ablated accompanied by a plasma generation.



(a)



(b)

Fig. 4.1. (a) Schematic view of experimental setup and (b) Target assembly.

Since the plasma is confined by a transparent material to the incident laser beam, it induces stronger and longer recoil pressure than that of a direct ablation [43]. Here, a tap water layer of 3 mm thickness is used as a confining medium which has approximately 100 % transmission of a driving laser beam at one order of J/cm^2 fluence range [58]. 304 stainless steel is used as a target material whose thickness is varied from 10 to 800 μm to understand the physics of shock wave according to the distance of wave propagation. A spot diameter of 2.11 mm is obtained by using a plano-convex lens of 100 mm focal length which is chosen relatively long, for reducing the error during the installation of a spot diameter on the sample. The large ratio of spot diameter to thickness of the target and the flat-top spatial profile of a laser beam make it possible to maintain a 1-D planar shockwave for correct determination of a shock state [59]. Since the laser used in this experiment was designed for medical use, there is no sync out port to synchronize with the other laboratory apparatus. Instead, a photodetector was used to trigger the oscilloscope by collecting scattered light when the beam is reflected from the mirror. The oscilloscope to record output signals from VISAR is synchronized with the arrival time of shock waves at the back free surface of a target.

VISAR is set up to measure back free surface velocity of a target which starts to move when shock waves arrive. The principle and details of the VISAR used in our system were explained in authors' earlier works [60]. The probe beam of the VISAR is precisely aligned to receive reflected beam from the back surface of the target and moved back and forth to obtain the maximum output signals at the exact focal point. The resolutions of time and

velocity are respectively set to 1 ns and 1 m/s by installing the delay leg of 200 mm length. The measurement error of velocity is lower than 2 % in the present experimental set up.

From the back free surface velocity, the longitudinal stress (or pressure) of shock wave is determined by the Rankine-Hugoniot jump condition and elastoplastic behavior of the material. The longitudinal stress is determined by the expressions of Eq. (4.1) where the amplitude is compared with the Hugoniot elastic limit (HEL).

$$\sigma_x = \begin{cases} \rho_0 C_{el} u_p & (< \text{HEL}) \\ \rho_0 U_s u_p + \frac{2}{3} Y_0 & (> \text{HEL}) \end{cases} \quad (4.1)$$

$$u_f = 2u_p \quad (4.2)$$

$$U_s = C_0 + S u_p \quad (4.3)$$

Here, HEL marks the transition from a purely elastic state to an elastoplastic state. u_p , U_s , C_{el} , and C_0 represent the velocities of particle, shock wave, elastic wave, and bulk sound wave, respectively. By matching impedance at the free surface, the resulting particle velocity is approximated as a half of the free surface velocity, u_f which is measured by VISAR [61]. Shock and particle velocities are assumed to follow a linear relationship for materials over a wide range of pressures as indicated in the experiments [62]. ρ_0 , Y_0 , and S represent density before shock compression, compressive yield strength, and characteristic material constant, respectively. Material properties

for calculation of the longitudinal shock stress in 304 stainless steel are as follows: $\rho_0 = 7900 \text{ kg/m}^3$, $C_0 = 4570 \text{ m/s}$, $C_{el} = 5770 \text{ m/s}$, $Y_0 = 205 \text{ MPa}$, $s = 1.49$ [59, 63].

4.1.2 Numerical Approach

An analytical method is developed to predict the shock behavior in the steel, such as evolution and attenuation of a shock front during its propagation. The method outlined here provides pressure, pressure gradient, velocity, acceleration, and position of a shock front [64, 65]. The mechanism of evolution and attenuation of shock waves are explained from the hydrodynamic point of view [66], such that mass and momentum are conserved and the coalescence of compression waves form shock waves. Shock waves evolve and decay by a sequence of compression and release waves. Also the perturbation waves are generated by the infinitesimal change in the pressure at the tail of a propagating pressure pulse. In the laboratory frame, perturbation waves immediately behind the shock front propagate at the velocity of $C + u_p$. Here, C and u_p represent sound velocity and particle velocity of each preceding shock front at a pressure, P . Since shock velocity is lower than the sum of sound and particle velocities, pressure of the shock front increases or decreases when perturbation waves overtake the shock front. Finally, a leading edge of the shock front becomes steep until the shock front reaches the maximum pressure, and then decays according to the

profile of input pressure pulse during the propagation. Here, the energy losses by viscosity, thermal conduction, and reflection of perturbation waves at the shock front are not taken into account in the model [62, 66].

Based on the assumptions of shock discontinuity and isentropic flow, an expression for the shock evolution and attenuation is known from the conservation laws of mass and momentum [67]. Then we can obtain the following expression for a 1-D planar geometry,

$$\frac{dP}{dx} = \frac{\left\{ (U_s - u_p)^2 - C^2 \right\} \frac{\partial P}{\partial x}}{(U_s - u_p)U_s + \rho U_s C^2 \frac{du_p}{dP}} \quad (4.4)$$

where x is the space coordinate, dP/dx is the variation of shock pressure, and $\partial P/\partial x$ is the pressure gradient immediately behind the shock front. In order to solve Eq. (4.4), U_s , u_p , C , and $\partial P/\partial x$ are expressed in terms of pressure. The conservation laws of mass and momentum for a steady 1-D planar shock wave are

$$\rho / \rho_0 = U_s / (U_s - u_p) \quad (4.5)$$

$$P = \rho_0 U_s u_p \quad (4.6)$$

From Eqs. (4.3) and (4.6),

$$U_s = \frac{C_0}{2} + \sqrt{\left(\frac{C_0}{2}\right)^2 + S \frac{P}{\rho_0}} \quad (4.7)$$

$$u_p = \frac{-\rho_0 C_0 + \sqrt{(\rho_0 C_0)^2 + 4S\rho_0 P}}{2S\rho_0} \quad (4.8)$$

$$\frac{du_p}{dP} = \frac{1}{\rho_0(2U_s - C_0)} \quad (4.9)$$

Here, the sound velocity is approximated along the Hugoniot, Eq. (4.10) was derived from the $U_s - u_p$ linear relation, Eq. (4.3) and standard assumption of Gruneisen parameter, Eq (4.11) [59].

$$C = (U_s - u_p) \left[2 \left(\frac{U_s}{C_0} - 1 \right) \left(1 - \frac{\Gamma_0}{2} \frac{u_p}{U_s} \right) + 1 \right]^{1/2} \quad (4.10)$$

$$\Gamma \rho \cong \Gamma_0 \rho_0 \quad (4.11)$$

Γ_0 and Γ are the Gruneisen parameters for the initial density and the shocked state, respectively. The Shock Hugoniot data of 304 stainless steel and a water are provided in Table. 4.1.

Table 4.1. Shock Hugoniot data of 304 stainless steel and water.

	ρ_0 [kg/m ³]	C_0 [m/s]	S	Γ_0
304 SS	7900	4570	1.49	2.17
Water	1000	1489	1.79	1.65

An expression for $\partial P / \partial x$ at specific position was obtained in the following

way [64]. Pressure waves of different magnitude are emitted from the interface between target and confining medium at different times during the plasma generation, and then transmitted to the target material at a different speed which is a sum of the particle and sound velocities. Due to the difference in the departure time of pressure waves at the interface and the difference of particle and sound velocities depending on pressure amplitude, the arrival time of pressure waves reaching a specific position x is changed with the distance of wave propagation. In all earlier works, the ablation surface or the interface between target and confinement was fixed at the reference position ($x=0$) without considering the particle velocity. The temporal profile of an input loading was simplified as a triangular pulse which is linear in time. However, in the present work, the displacement of the ablation surface and the actual temporal profile of input pressure loading are added to the consideration for more realistic results. Since the profile of plasma pressure is expressed as a function of time, the pressure derivative with respect to time $\partial P/\partial t$ must be obtained prior to expressing in the form of $\partial P/\partial x$.

$$\frac{\partial P}{\partial t} = \left[\begin{array}{c} -\frac{x}{(C+u_p)^2} \left(\frac{du_p}{dP} + \frac{dC}{dP} \right) + \left(\frac{\partial P}{\partial t} \Big|_{x_A} \right)^{-1} \\ -\frac{x_A}{(C+u_p)} \left\{ \frac{u_p}{x_A} \left(\frac{\partial P}{\partial t} \Big|_{x_A} \right)^{-1} - \frac{1}{(C+u_p)} \left(\frac{du_p}{dP} + \frac{dC}{dP} \right) \right\} \end{array} \right]^{-1} \quad (4.12)$$

Here x_A is the position of the ablation surface and $\partial P/\partial t|_x$ is the time derivative of pressure at the ablation surface. x_A and dC/dP are expressed

as follows.

$$x_A = \int_0^t u_p(t) dt \quad (4.13)$$

$$\begin{aligned} \frac{dC}{dP} = \frac{d}{dP} (U_s - u_p) A^{1/2} \\ + \frac{(U_s - u_p)}{2} A^{-1/2} \times \left\{ \begin{aligned} &2 \frac{d}{dP} \left(\frac{U_s}{C_0} - 1 \right) \left(1 - \frac{\Gamma_0}{2} \frac{u_p}{U_s} \right) \\ &+ 2 \left(\frac{U_s}{C_0} - 1 \right) \frac{d}{dP} \left(1 - \frac{\Gamma_0}{2} \frac{u_p}{U_s} \right) \end{aligned} \right\} \end{aligned} \quad (4.14)$$

$$\begin{aligned} \text{where } A &= \left[2 \left(\frac{U_s}{C_0} - 1 \right) \left(1 - \frac{\Gamma_0}{2} \frac{u_p}{U_s} \right) + 1 \right], \\ \frac{d}{dP} (U_s - u_p) &= \frac{S - 1}{\rho_0 (2U_s - C_0)}, \\ \frac{d}{dP} \left(\frac{U_s}{C_0} \right) &= \frac{S}{\rho_0 C_0 (2U_s - C_0)}, \\ \frac{d}{dP} \left(\frac{u_p}{U_s} \right) &= \frac{C_0}{\rho_0 U_s^2 (2U_s - C_0)} \end{aligned} \quad (4.15)$$

Since the velocity of pressure wave is $C + u_p$, $\partial P / \partial x$ becomes

$$\begin{aligned} \frac{\partial P}{\partial x} &= - \frac{1}{C + u_p} \frac{\partial P}{\partial t} \\ &= \left[\begin{aligned} &\frac{x}{C + u_p} \left(\frac{du_p}{dP} + \frac{dC}{dP} \right) - (C + u_p) \left(\frac{\partial P}{\partial t} \Big|_{x_A} \right)^{-1} \\ &+ x_A \left\{ \frac{u_p}{x_A} \left(\frac{\partial P}{\partial t} \Big|_{x_A} \right)^{-1} - \frac{1}{(C + u_p)} \left(\frac{du_p}{dP} + \frac{dC}{dP} \right) \right\} \end{aligned} \right]^{-1} \end{aligned} \quad (4.16)$$

The variation of shock pressure ΔP according to propagation distance Δx

is calculated by using Eq. (4.4) with above variables written in terms of pressure. In return the shock pressure in x , $P(x)$ is obtained by the iteration,

$$P(x_{i+1}) = P(x_i) + \Delta P \quad \text{where} \quad \Delta P = \frac{dP}{dx} \Delta x = \frac{dP}{dx} U_s \Delta t \quad (4.17)$$

The acceleration and time of the shock front at position x are computed from

$$a(x) = \frac{dU_s}{dt} = \frac{dU_s}{dP} \frac{dP}{dx} \frac{dx}{dt} = \frac{dU_s}{dP} \frac{dP}{dx} U_s \quad (4.18)$$

$$t = \int_0^x \frac{dx}{U_s(x)} \quad (4.19)$$

To simulate the temporal profile of the plasma pressure in the confined geometry according to temporal shape of the laser pulse, 1-D analytical model was applied [68]. When a laser beam is irradiated at the interface between a target and a confinement, rapid generation and expansion of plasma induce strong shock waves which propagate into the two mediums. The fluid motion behind the shock waves results in a displacement of the interface. Using the Hugoniot relation, particle velocities and the time derivative of the interface thickness at time t can be related as follows.

$$u_{p,1}(t) + u_{p,2}(t) = \frac{dL(t)}{dt} = \left(\frac{1}{Z_1} + \frac{1}{Z_2} \right) P(t) = \frac{2}{Z} P(t) \quad (4.20)$$

Here, shock impedance of materials, $Z_i = \rho_{0,i} U_{s,i}$ can be regarded as acoustic impedance for a pressure range of the experimental condition. The

subscripts 1 and 2 represent properties for target and confining mediums, respectively.

The deposited laser energy during time interval $I(t)dt$ is used as the pressure-volume work $P(t)dL$ and the internal energy of the plasma $E_i(t)dL$. The fraction α and $1-\alpha$ of the internal energy are respectively used for the thermal energy and ionization of the gas. By assuming the plasma as an ideal monatomic gas, the pressure is represented with the thermal energy and corrective factor α [69]. Therefore the conservation of energy can be expressed as

$$\begin{aligned} I(t) &= P_p(t) \frac{dL(t)}{dt} + \frac{d}{dt} [E_i(t)L(t)] \\ &= P_p(t) \frac{dL(t)}{dt} + \frac{3}{2\alpha} \frac{d}{dt} [P_p(t)L(t)] \end{aligned} \quad (4.21)$$

$$P_p(t) = \frac{2}{3} E_T(t) = \frac{2}{3} \alpha E_i(t) \quad (4.22)$$

Here $P_p(t)$, $L(t)$, and $E_i(t)$ are the pressure, thickness, and internal energy density of the plasma, respectively. $E_T(t)$, $I(t)$, and α represent the thermal energy density of the gas, the absorbed laser intensity, and the ratio of thermal to internal energy density, respectively. The pressure, impedance, and laser intensity are expressed in the unit of Pa, kg/m²s, and W/m², respectively. By combining Eqs. (4.20) and (4.21), it becomes

$$\ddot{y} = \frac{1}{y} \left[\frac{\alpha Z}{3} I(t) - \frac{2\alpha + 3}{3} \dot{y}^2 \right] \quad \text{where} \quad \begin{cases} y = \int P_p(t) dt \\ \dot{y} = P_p(t) \end{cases} \quad (4.23)$$

The temporal profile of plasma pressure is obtained by solving the 2nd order ordinary differential equation.

Since this model assumes that the plasma pressure is strong enough to send shock waves into the adjacent two materials, the model should be used with care only when target material is ablated. Therefore we considered the ablation threshold in conjunction with the laser fluence in time in order to find the initiation point of the ablation. For a Gaussian laser pulse which is used in the experiment, the intensity profile and laser fluence in time are expressed as follows,

$$I(t) = \frac{F}{\sigma\sqrt{2\pi}} \int \exp\left(-\frac{t^2}{2\sigma^2}\right) dt \quad (4.24)$$

$$F_{th} = \int_{-\infty}^{\beta\sigma} I(t) dt = \frac{F}{2} \left[1 + \operatorname{erf}\left(\frac{\beta}{\sqrt{2}}\right) \right] \quad (4.25)$$

Here F , F_{th} , and σ are the total laser fluence, ablation threshold of a target material, and standard deviation of Gaussian distribution, respectively. Consequently, the generation point of the plasma and subsequent shock waves is shifted by $\beta\sigma$.

By assuming that the plasma experiences adiabatic cooling process after the pulse duration of the laser beam, the plasma pressure is expressed by the following relation.

$$P_p(t) = P_p(\tau) \left[\frac{L(\tau)}{L(t)} \right]^\gamma \quad (4.26)$$

where τ and λ represent the pulse duration of the laser beam and the ratio

of specific heat, respectively.

4.1.3 Results and Discussion

The free surface velocity for various thicknesses was measured by VISAR to investigate the shock attenuation with distance of the wave propagation. Figure 4.2 shows the velocity profile of the free surface for various thicknesses of a target at the laser pulse of 8.6 J/cm^2 .

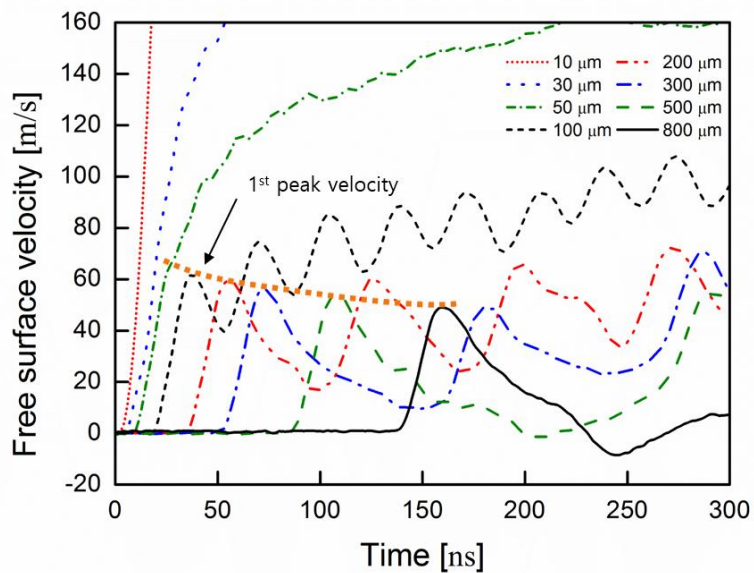


Fig. 4.2. Temporal profile of the free surface velocity according to the thickness of a target at laser energy of 8.6 J/cm^2 .

The first and the subsequent peaks are caused by the arrival of the shock

waves at the free surface and its reverberations, respectively. From the amplitude of the first peak, shock pressure is determined. As the thickness of the target decreases, the time interval and the fluctuation amplitude of the free surface velocity between each crest and trough become shorter and narrower. In the case of a thin foil target whose double transit time of a shock wave is much shorter than the duration of the plasma pressure loading, numerous reverberations of shock and release waves rapidly accelerate a target without noticeable fluctuations [69]. This phenomenon shows the experimental difficulty where the measurement of the first peak by a single shock is a challenging task for a thin target below 100 μm thickness. Therefore, the pulse width and temporal profile of the input pressure loading are quite essential when determining the minimum thickness limit for a potential miniaturization of a such system.

The analytical model for laser-induced plasma and evolution/attenuation of shock is applied near the ablation surface where the accurate measurement of the shock properties is not possible due to the minimum thickness limit. The pressure and particle velocity of a shock front obtained both numerically and experimentally are represented in terms of the distance of wave propagation in Fig. 4.3. Solid lines denote the theoretical results based on the hydrodynamic analysis. Dots are experimental results shown with maximum and minimum deviations. Here, the calculation is validated by showing a good agreement between the calculation and experiment. The shock behavior such as how its front is evolved and attenuated within the thickness limit shows a different characteristics with respect to a laser fluence.

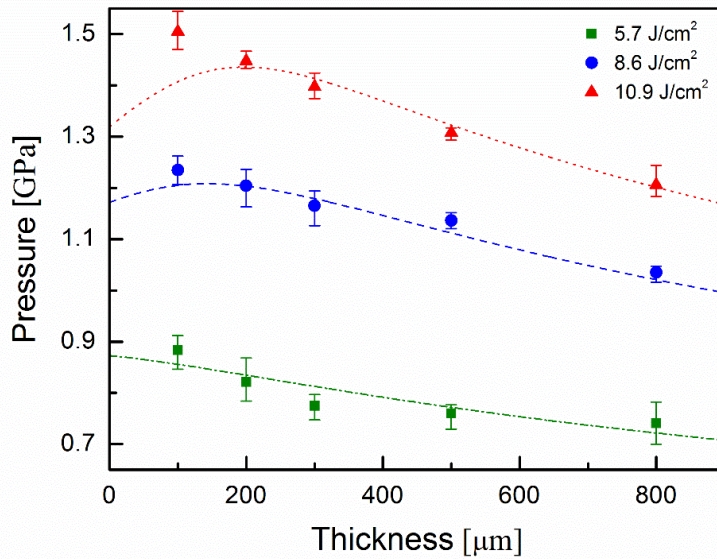


Fig. 4.3. Evolution and decay of shock pressure represented by analytical model and experimental results.

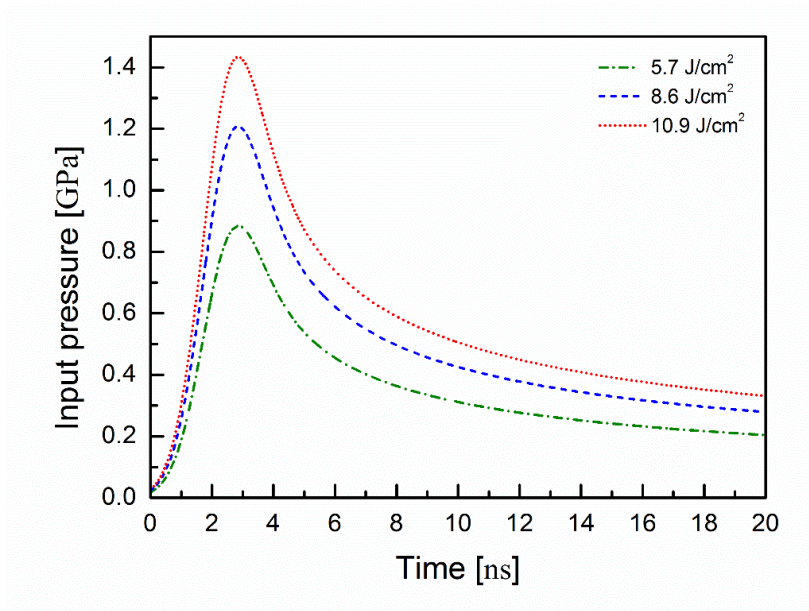
In the case of 10.9 J/cm^2 , the shock front evolves until reaching a maximum value and then starts to decay. Whereas the shock front is immediately attenuated without evolution in the beginning for all other low fluence cases. This shows that the distance to shock steepening is necessary to estimate the exact magnitude of shock pressure at a desired distance. Therefore, such distance must be considered in addition to the minimum thickness limit.

The different behavior of shock waves is resulted from the reflectivity and ablation threshold of a target. Generally, total reflectivity of metals above the ablation threshold starts to decrease rapidly as laser fluence is increased and kept at constantly rising. In the case of a nanosecond Nd:YAG laser ablation at room temperature and pressure, the total reflectivity of metals starts to

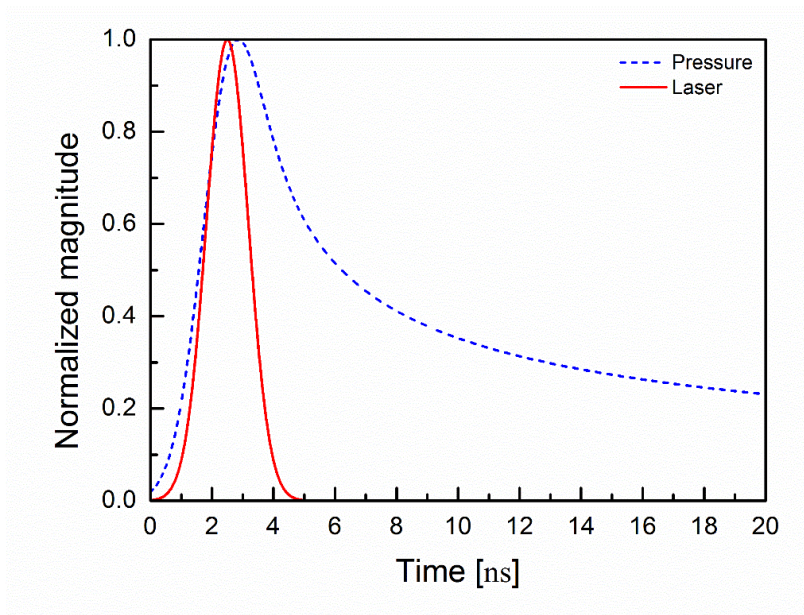
decrease in the fluence proximity of 1~12 J/cm² [19]. Since the fluence range of our experimental condition is within the transient region, the reflectivity of the target surface must be considered for exact plasma pressure from which exact shock behavior can be obtained. Therefore, Eq. (4.23) is corrected by adding the reflectivity term to consider the change of the reflectivity according to laser fluence, such that

$$\ddot{y} = \frac{1}{y} \left[\frac{\alpha Z}{3} (1-R) I(t) - \frac{2\alpha + 3}{3} \dot{y}^2 \right] \quad (4.27)$$

The plasma pressures generated by a Gaussian laser pulse at various fluences are represented in Fig. 4.4(a).



(a)



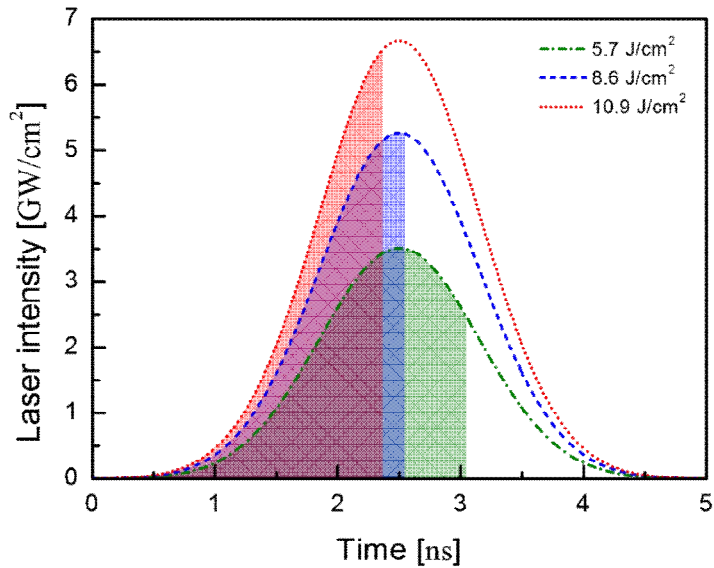
(b)

Fig. 4.4. Temporal profile of (a) plasma pressures at laser pulse of various laser fluence and (b) normalized laser intensity and plasma pressure for 10.9 J/cm².

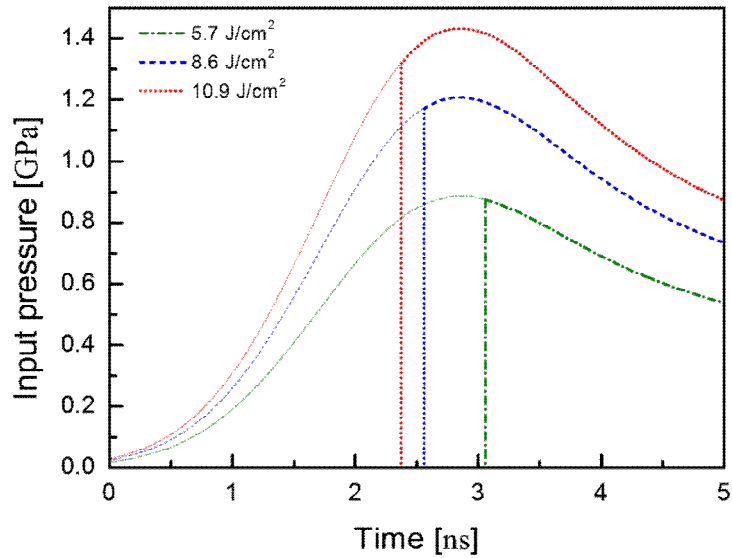
As the laser fluence increases, the slope of the pressure gradually increases with a similar rise time to a maximum value for all cases, then the pressure starts to decay slowly. Figure 4.4(b) shows the temporal profile of laser intensity and plasma pressure which are normalized by their maximum values without considering an ablation threshold. Since the plasma pressure is mostly influenced by the absorbed laser intensity which is used to heat and vaporize the target, the temporal profile of the plasma pressure behaves similarly to the temporal profile of the laser intensity until reaching the peak. Whereas the plasma pressure smoothly decays because it is controlled by the rate of heat

conduction from the metal and vaporization to the colder enclosed medium and pressure-volume work done on the neighboring medium [70].

In the analytical model, laser-induced shock waves are generated when a deposited laser fluence reaches the ablation threshold of a target surface. Therefore ablation threshold and deposited laser fluence in time have an influence on the amplitude and initiation time of shock wave, which are calculated by using Eqs. (4.23) and (4.24). Figure 4.5(a) shows intensity profile of a Gaussian laser pulse according to the laser fluence and ablation threshold which is represented as an area filled with color and shades. As the laser fluence increases, the peak amplitude of laser intensity rises due to the same standard deviation of a Gaussian distribution, and consequently the occurrence time of laser ablation goes forward.



(a)



(b)

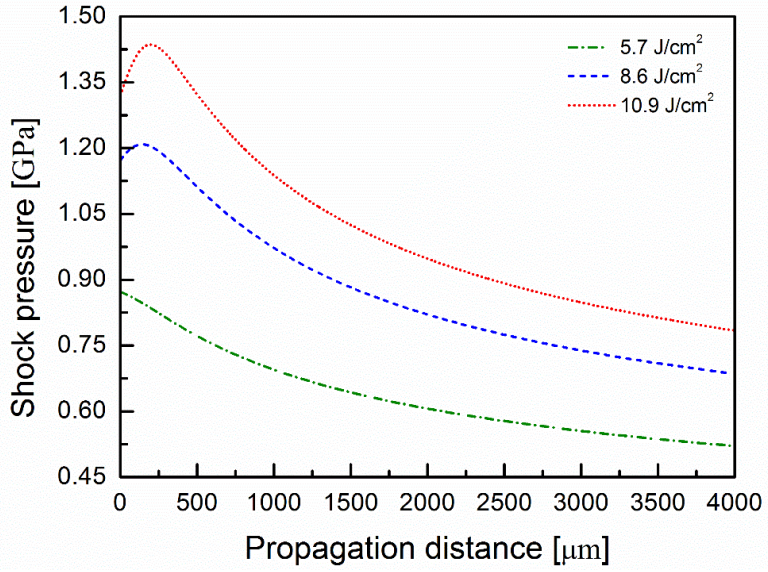
Fig. 4.5. (a) Laser energy used for ablation of 304 stainless steel and (b) Temporal profile of plasma pressure after laser ablation according to laser fluence.

This means that different magnitude and temporal shape of the plasma pressure is directed to the target surface, resulting in the different behavior of the shock waves in the medium. As shown in Fig. 4.5(b), the occurrence time of plasma pressure is the same with that of the laser ablation, and the plasma pressure starts to follow the previously calculated results after the onset of plasma generation. The estimated reflectivity of 304 stainless steel and the time occurrence of laser ablation are represented in Table. 4.2.

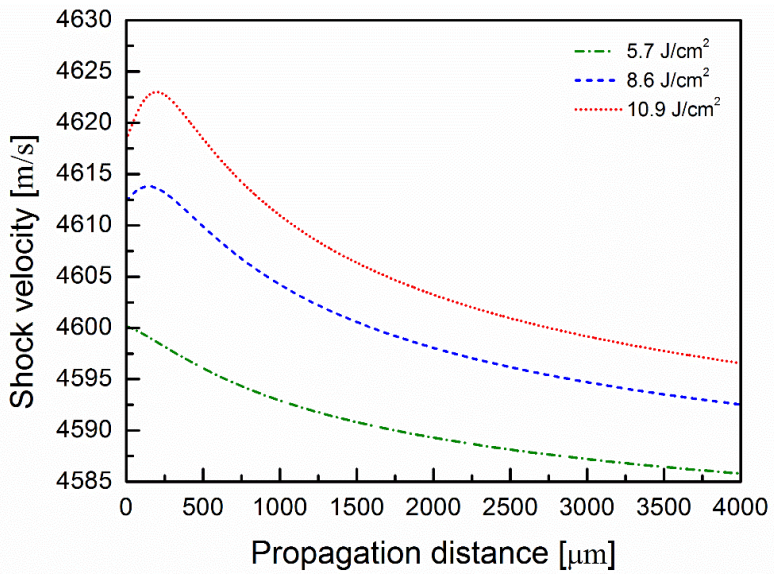
Table 4.2. Estimated reflectivity of target surface and time occurrence of laser ablation according to laser fluence.

Laser fluence [J/cm ²]	Reflectivity	Time occurrence [ns]
5.720	0.448	3.057
8.580	0.313	2.559
10.868	0.234	2.374

Using the analytical model validated from the experimental results, it is possible to simulate the laser-induced plasma pressure and the subsequent shock waves in the suggested thin medium. Figures 4.6 represents pressure, velocity, and acceleration of a shock front as a function of distance of wave propagation, respectively. As shown in Fig. 4.6, the overall shape of the shock pressure and velocity is similar to the temporal profile of plasma pressure toward a target surface that was shown in Fig. 4.4(a) and 4.5(b). This means that evolution and attenuation of a shock front is greatly influenced by the temporal shape of an input pressure or a laser pulse, and the position of shock front is affected by the material properties of a target and magnitude of shock pressure. This result is consistent with the existing reports where input pressure pulse in a triangular or trapezoidal shape causes the shock front to evolve and decay in a triangular or trapezoidal form [64, 65]. Figure 4.6 also describes the acceleration of a shock front with the propagation distance.



(a)



(b)

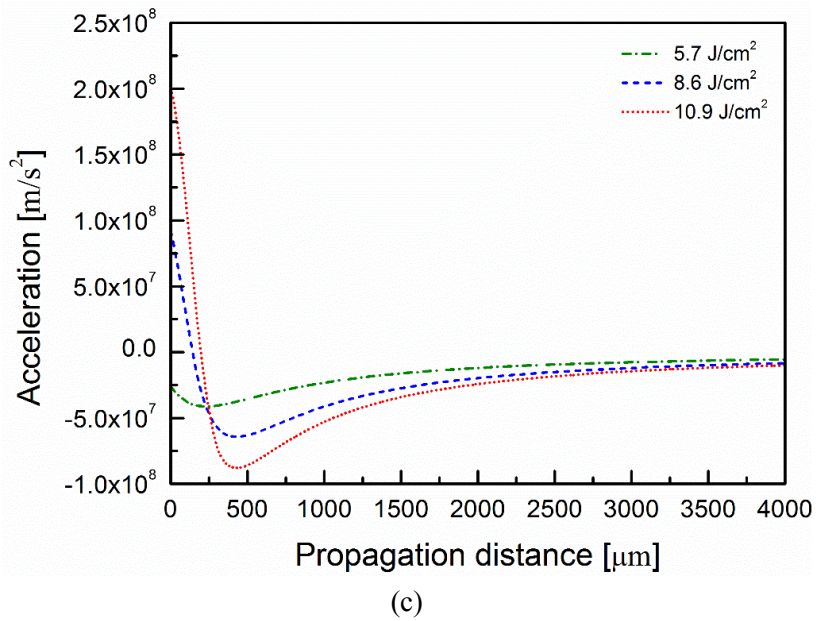


Fig. 4.6. (a) Pressure, (b) Velocity, and (c) Acceleration of a shock front with respect to the distance of wave propagation at various laser fluence.

When pressure waves exceeding HEL is transmitted through the elastoplastic material, the waves are divided into an elastic precursor of HEL amplitude and a plastic shock wave. The measurement of HEL is necessary as it is related to the mechanical properties of the target. The strain rate influences the value of HEL which is much higher in the laser-driven shock experiment when compared with gas guns. Therefore it is essential to measure HEL in the laser-driven shock system as discussed here. The only way to determine HEL is by distinguishing the elastic-plastic inflection from the free surface velocity [71]. Shown in Fig. 4.2, 304 stainless steel has an indistinguishable HEL point that is different from those of 316L and 55C1 steels [72]. Therefore, what we proposed in this analysis favorably determines

the inflection point by drawing an acceleration curve along with the free surface velocity as represented in Fig. 4.7.

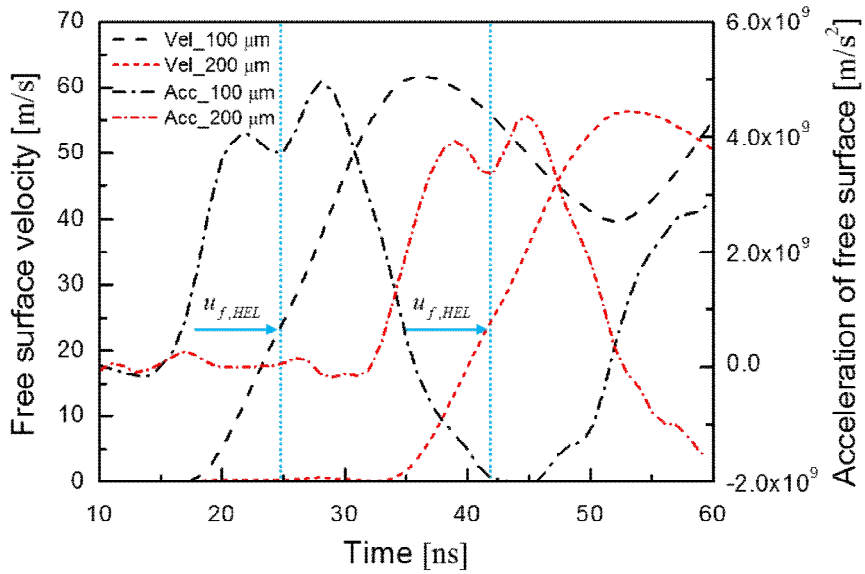


Fig. 4.7. Velocity and acceleration profile of free surface at laser pulse of 8.6 J/cm^2 .

During the period in which the velocity increases, the acceleration curve has two peaks. These waves are caused by the arrival of an elastic precursor and a plastic shock wave, respectively. Thus, it is possible to determine HEL even if material has a blurred distinction. The amplitude of HEL is calculated from the conservation of momentum, from which the dynamic yield strength is obtained [61].

$$HEL = \rho_0 C_{el} u_{p,HEL} \quad (4.28)$$

$$\sigma_y^{dyn} = \left(\frac{1-2\nu}{1-\nu} \right) \text{HEL} \quad (4.29)$$

Here ν and σ_y^{dyn} represent the anisotropy coefficient and the compressive yield strength at high strain rate of a material, respectively. We have the following values on 304 stainless steel: $u_{f,HEL} = 23$ m/s, $\text{HEL} = 524$ MPa, $\sigma_y^{dyn} = 330$ MPa, which remain almost constant regardless of propagation depth all within a few hundred orders of a micron. The dynamic yield strength is different with the quasi static yield strength $\sigma_y = 205$ MPa. This means that the compressive yield strength is dependent on the strain rate [73].

$$\dot{\varepsilon} = \frac{1}{C_0} \frac{du_p}{dt} \quad (4.30)$$

The yield strength at the strain rate 10^5 s^{-1} is approximately 1.6 times higher than the yield strength at the quasi strain rate 10^3 s^{-1} . Therefore the amplitude of an elastic precursor and the dynamic yield strength must be considered for the present setup, aimed at studying the shock attenuation in a miniaturized pyrotechnic unit.

4.2 Shock Waves Generated by Flyer Impact

4.2.1 Background and Motivation

A detonator is a primary initiator unit that insures reliable triggering of an explosive train of which the sequence of events culminates in the detonation of sensitive high explosives in a variety of applications [74]. The explosive train requires a physical barrier or misalignment between the primary and secondary explosives to avoid the inherent hazard of accidental discharging during handling and transport. However, an exploding foil initiator (EFI), also known as a slapper detonator, simplifies the design of the explosive train by eliminating the mechanical assemblies usually used for safety when using explosives, because it can directly initiate secondary explosives by the impact of a flyer at a desired velocity [75]. Thus, the performance map of the EFI detonator and the burst current density must be known in order to optimize the explosive system [76].

An increasing demand for miniaturized pyrotechnic devices has resulted in an investigation of the shock initiation performance of a micro flyer designed for a miniaturized EFI detonator [74]. The shock pressure according to the impact velocity and flight characteristics of a flyer, of which the thickness and diameter are two and three orders of micrometers, respectively, must be fully understood. Therefore, an EFI is used to initiate an insensitive high explosive (HE) from the impact of a Kapton flyer of which the thickness is 12.5 μm and velocity reaches up to 5 km/s. Velocity Interferometer System for Any Reflector (VISAR) measurement was conducted to obtain the impact velocity

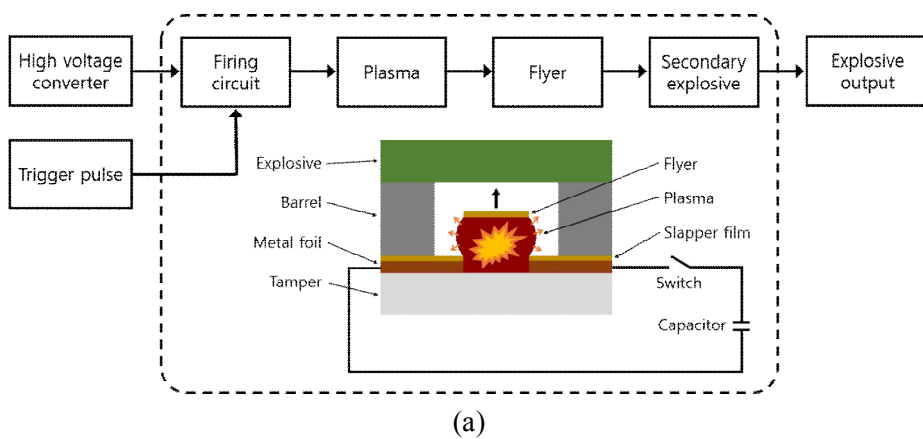
of a flyer; the impact velocity is in principle the most significant parameter of EFI performance. In comparison to the existing EFI, the present micro EFI offers additional challenges associated with obtaining precise measurements of flyer velocity. The VISAR measurement can only be taken for a planar flying surface, and the flyer poses various flight motions of rotation, bend, and fragmentation due to its extreme thinness [50]. A VISAR system cannot measure the exact center velocity within the focal spot, nor can it receive deflected Doppler-shifted light due to the relatively large deformation on the very small and local area of the target surface [77]. Therefore, as an alternative to using flyer velocity, a 304 stainless steel witness plate is placed in the flight path of the VISAR to measure the free surface velocity of the plate instead of the flyer. Consequently, the averaged impact velocity of a flyer and the following impact pressure are obtained by using the impedance matching technique [61, 66]. The lens configuration of a VISAR probe is designed to receive more accurate and longer velocity data without failure of data acquisition. Numerical analysis is also performed to determine the initial pressure at zero thickness of a target, because it is difficult to distinguish the initial value from the experimental results due to the multiple reverberations of shock waves and large deformation as the thickness of a target decreases. By varying the thickness of a target, the attenuation pattern of shock waves is determined in terms of the distance of wave propagation for numerical validation. Therefore, the impact velocity of a small-scale flyer and the ensuing shock pressure according to the burst current density are investigated in the current EFI system.

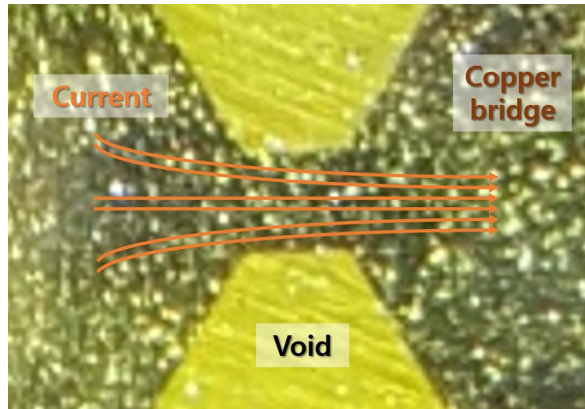
The aim of the detailed description and analysis of the system is the development and optimization of an EFI towards miniaturization of the pyrotechnic device.

4.2.2 Experimental Approach

Utilizing the impact of a flyer is a useful technique to generate reproducible pressure pulse in a target material. The impact pressure and duration of the pressure pulse can be easily controlled by changing the impact velocity and thickness of the flyer, respectively. Therefore, in this experiment, an EFI is used to generate the input shock loading on the explosive.

The operation sequence and schematic of an EFI detonator is presented in Fig. 4.8(a). Fig. 4.8(b) shows the case when the electric current pulse of a capacitor,





(b)

Fig. 4.8. (a) Operation sequence and schematic of an exploding foil initiator and (b) Metal foil layer configured as a bridge structure having a narrow channel.

which is charged up to several thousand volts, is discharged onto a thin metal bridge foil configured as a bridge structure having a narrow channel. The foil undergoes an explosive phase change to a plasma state, as the electrical resistance is at maximum in the narrow channel. The expansion of high-density plasma rapidly accelerates the flyer to the desired velocity by varying the charging voltage of the capacitor. Subsequently, an explosive block is initiated from a shock wave generated by the flyer impact.

VISAR measurement was conducted to obtain the impact velocity of a flyer for characterizing EFI. The measurement of the flyer velocity is particularly challenging as the system is developed for a miniaturized pyro-mechanical system, requiring additional precision in the measurement. First, while the VISAR measurement is intended for a planar surface, the actual flyer exhibits

various flight motions such as rotation, bending, and fragmentation due to its extreme thinness. Therefore, as an alternative to measuring flyer velocity, a witness plate of varying thickness is placed in the flight path to measure the bulging velocity, as depicted in Fig. 4.9.

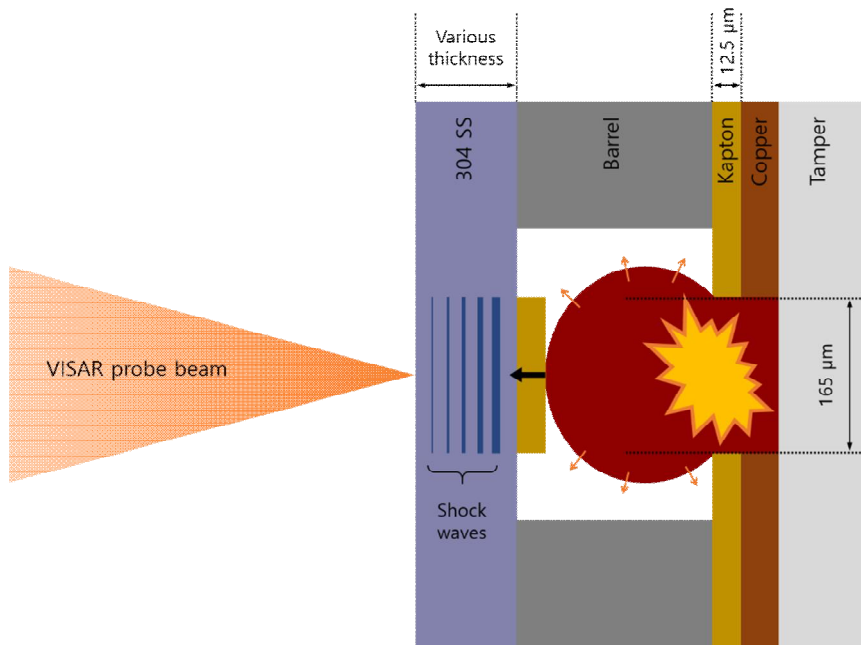


Fig. 4.9. Target assembly of the test EFI.

Then, the average impact velocity of a flyer is obtained using the impedance matching technique. 304 type stainless steel is used as a witness plate, of which the thickness varies from 50 to 300 μm to obtain the shock attenuation data according to the distance of wave propagation. Kapton used as a flyer is a dielectric insulation film which increases the plasma pressure by limiting the extent of heat transfer until the flyer is torn away [60]. Here, the thickness and width of the flyer are 12.5 μm and 165 μm, respectively.

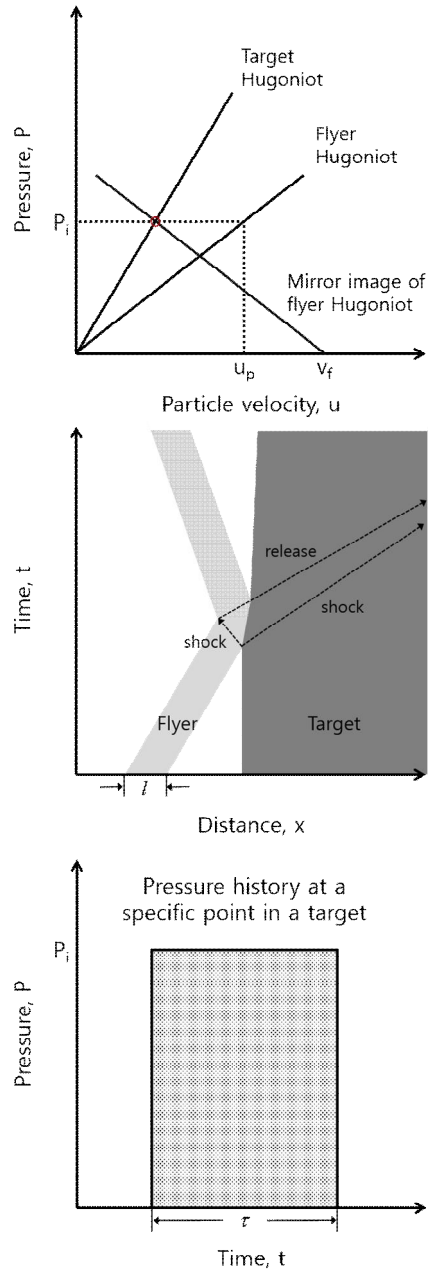


Fig. 4.10. Impedance matching technique for a relatively soft (Kapton) flyer impact on a hard (SS304) target.

Figure 4.10 illustrates the impedance matching technique in which the impact velocity, pressure, and pulse duration are determined from the analysis of P-u and x-t diagrams. Since the same impact pressure is loaded onto both sides of the target and flyer from the momentum conservation, the flyer velocity can be obtained from a mirror image of a flyer Hugoniot intersecting with a target Hugoniot at the impact pressure, which is measured by VISAR. Here, v_f , u_p , and l represent the impact velocity, particle velocity, and thickness of a flyer, respectively. P_t is the pressure imparted to a target material when a flyer impacts at velocity, v_f . τ is the pulse duration of the pressure loading, which is similar to the double transit time of the shock wave within a flyer. This is because the shock impedance of a flyer is lower than that of the target material. Therefore, a single rectangular pulse applied to a target is easy to control [66].

The impact of a micro flyer induces relatively large deformation on a small and local area of the target surface. However, since a VISAR system generally has a laser beam focal spot ranging from 0.5 to 1 mm, it is difficult to measure the exact velocity at a specific point when a flyer is smaller than the spot size [77]. Furthermore, it is easy to lose the light signal of a reflected beam because of the relatively large deformation at a very small spot. For this reason, the optical configuration of a VISAR probe is designed to receive more accurate and longer velocity data as shown in Fig. 4.11. The laser beam passes through an optical fiber and a collimator is emitted towards the aperture, which is used for central alignment with the optical axis of the collimated beam. The width of the collimated beam is increased through a

beam expander for a high numerical aperture and the beam is then focused on the free surface of the target. All these components are assembled at 5-axis optical mounts, which have an XYZ translation as well as horizontal and vertical tilting in order to precisely control the alignment between the probe beam and the target surface. As a result, the advantages include the reduction in both time and cost by minimizing the failure of data acquisition.

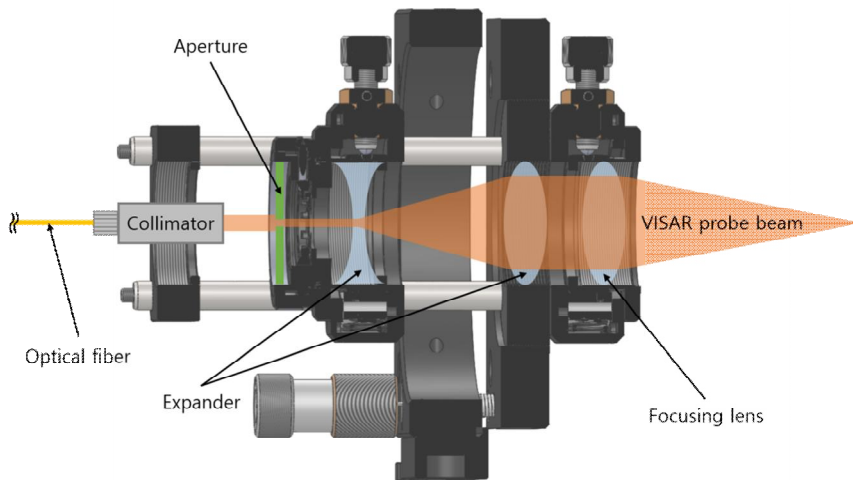


Fig. 4.11. Assembly configuration of the improved VISAR probe.

In order to determine an appropriate lens configuration for each experimental condition, the Gaussian beam propagation needs to be understood [78]. Equation (4.31) represents the diameter of the focused spot in terms of the input beam and focusing lens parameters, as shown in Fig. 4.12.

$$d_0 = \left(\frac{4\lambda}{\pi} \right) \left(\frac{f}{D} \right) \quad (4.31)$$

Here, d_0 is the Gaussian beam diameter, which is defined by the $1/e^2$ contour of the maximum intensity, and f is the focal length of a convex lens. λ and D represent the wavelength and diameter of the incident beam, respectively.

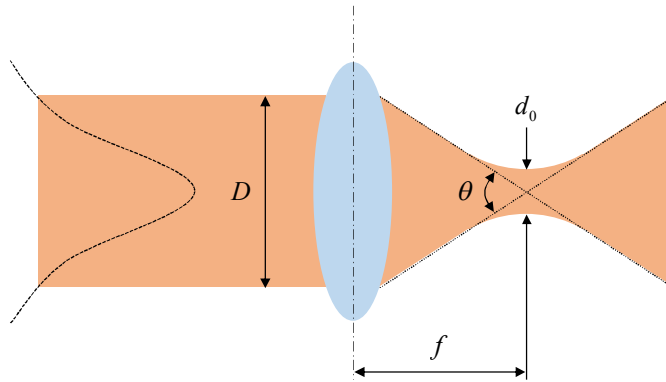


Fig. 4.12. Gaussian beam propagation with a focusing lens: spot size and total beam divergence determined by the focal length of a lens and the diameter of the incident beam.

The total angle of light that can enter or exit the lens is determined by using Eq. (4.32).

$$\theta \approx \frac{D}{f} = \frac{1}{N} \approx 2NA \quad (4.32)$$

where N and NA are the photographic f-number and numerical aperture of the lens, respectively. Therefore, we apply a beam expander and a lens of short focal length to increase the numerical aperture and precision of the focal point

of the VISAR probe. Consequently, the spot diameter of 5 μm and the numerical aperture of 0.19 radian are obtained from an incident beam size of 15.5 mm, focal length of 40 mm, and laser wavelength of 1550 nm.

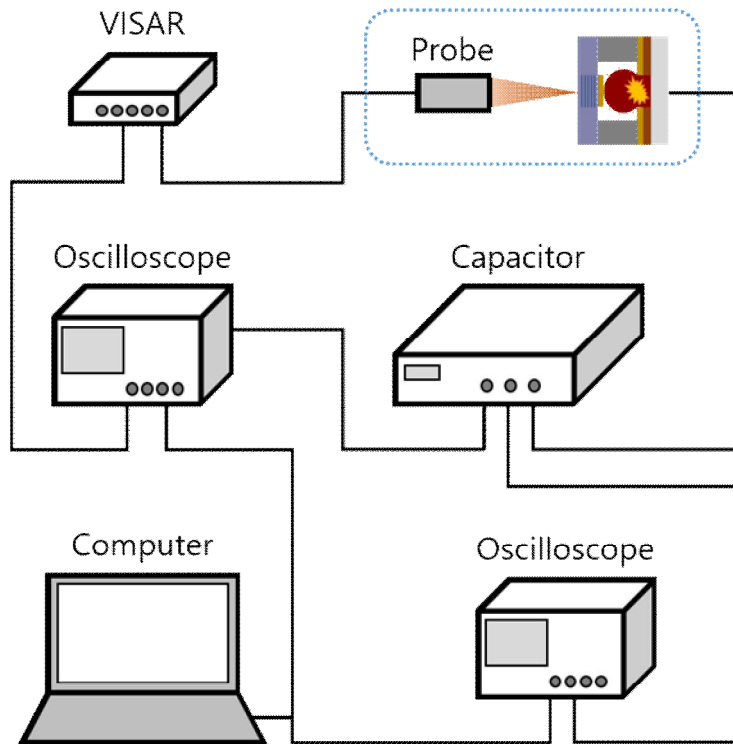


Fig. 4.13. Schematic of overall experimental setup.

As shown in Fig. 4.13, the overall experimental setup consists of an assembly of a target and a VISAR probe, a capacitor, two oscilloscopes, and a computer. When a capacitor is discharged, a current pulse flows out to the EFI detonator and then propels the Kapton flyer. The VISAR is connected to an oscilloscope to measure the intensity history of photodetectors, which varies

with change of flyer velocity. The principle and details of the VISAR used in our system were explained in the authors' earlier work [60]. To capture the free surface motion of a target when a collision with a flyer occurs, it is necessary to synchronize the release of the transistor-transistor logic (TTL) signal emitting from the capacitor with the trigger point of an oscilloscope. After measuring the delay between the release of the TTL signal and start point of intensity fluctuation, the oscilloscope is triggered in 100 ns after firing the capacitor. The profile of the current pulse is also measured using another oscilloscope to validate the bursting current for each shot.

4.2.2 Numerical Approach

Generally, the shock pressure is obtained from the peak value of the velocity profile, which is measured by a velocity interferometer. However, when the double transit time of shock waves within a target plate is less than the pulse duration of the shock load, multiple reverberations of shock and release waves rapidly accelerate the target without obvious fluctuation of velocity. It is difficult to distinguish the peak value from the velocity profile when shock waves arrive at the free surface. Therefore, numerical simulation is adopted to overcome the experimental limitation and to predict the initial pressure at the zero thickness by comparing with the measured time history of the free surface velocity of the target at various thicknesses.

In the present work, numerical analysis was conducted by using ANSYS

Explicit Dynamics, which is based on the explicit time integrator that handles the highly transient and nonlinear dynamics subjected to a very short and severe loading condition. In the solution process, the Lagrangian formulation is used to solve the governing partial differential equations for conservation of mass, momentum, and energy along with constitutive equations as well as initial and boundary conditions. The Lagrange-Lagrange interaction specified for the projectile/target contact and three-dimensional (3-D) structures is applied to determine the influence of geometry on longitudinal stress and particle velocity according to the wave propagation.

Erosion, which based on the strain, is permitted to ensure that the time step is kept large enough to ensure calculation to a specified termination time at reasonable stability. When a Lagrangian element is removed, the element changes into a free node of which the mass can be neglected or transferred to the adjacent nodes of the elements. If the inertia of the resulting free node is retained, the mass and momentum of the free node are maintained and are involved in the following calculation step. Otherwise, all free nodes are automatically eliminated from the calculation.

As shown in Fig. 4.14, a 304 stainless steel target of 700 μm diameter and 400 μm thickness and a Kapton flyer of 165 μm diameter and 12.5 μm thickness are defined for a two-dimensional (2-D) axisymmetric flyer impact. Quadrilateral dominant meshes are generated and then inflated toward the edge of the flyer and widened toward the fixed edge to ensure optimal computation time and accuracy. Here, quadrilateral elements of a size of 2 μm are used to construct the mesh with a reasonable aspect ratio. Gauges are

placed at intervals of 10 μm along the central axis to record the shock signals along the wave propagation.

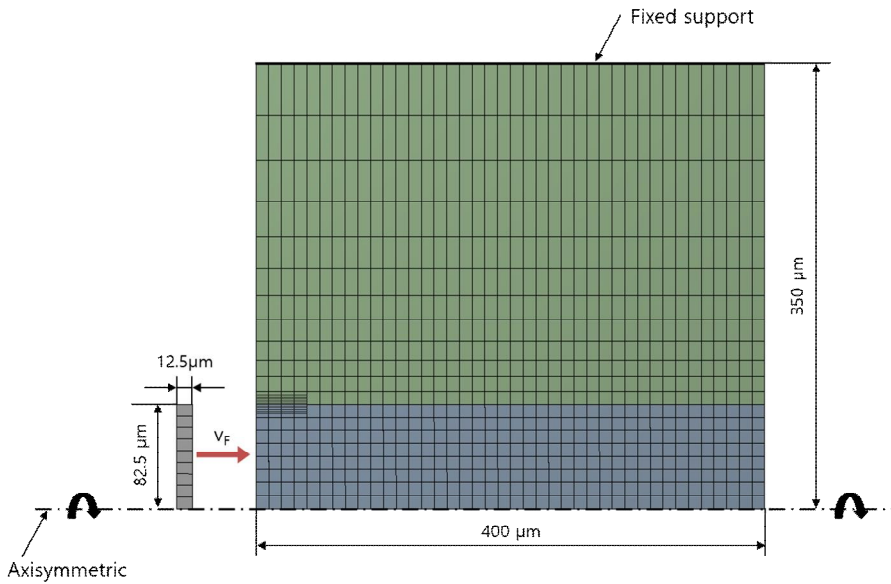


Fig. 4.14. Geometry and mesh of finite element model for 2-D axisymmetric flyer impact.

The material model is comprised of (i) an equation of state representing the relation between density, pressure, and internal energy and (ii) strength model describing the constitutive relation. For the impact phenomenon between solid materials, the Mie-Gruneisen form of equation of state is used to properly describe the state of a shock compressed solid by representing the relation between volume and pressure.

$$p - p_0 = \frac{\Gamma}{v} (e - e_0) \quad (4.33)$$

where v , p , and e are the volume, pressure, and internal energy, respectively. Γ is the Gruneisen parameter which represents the thermal pressure induced by the vibration of atoms. p_0 and e_0 are the pressure and internal energy, respectively, at a reference state that is generally at a temperature of 0 K.

The Rankine-Hugoniot jump condition represents the relation between states on both sides of shock waves in uniaxial compression. The conservation of mass, momentum, and energy for the Rankine-Hugoniot condition are

$$\rho_0 u_s = \rho(u_s - u_p) \quad (4.34)$$

$$p_H - p_0 = \rho_0 u_s u_p \quad (4.35)$$

$$p_H u_p = \rho_0 u_s \left(\frac{u_p^2}{2} + e_H - e_0 \right) \quad (4.36)$$

Here, ρ_0 and ρ are the densities at the reference and current states, respectively, p_H and e_H represent the pressure and internal energy on the Hugoniot, respectively, and u_s and u_p are the velocities of shock wave and particle, respectively.

For most solids and many liquids, an empirical linear relationship between particle and shock velocities has been found over a wide range of pressures.

$$u_s = c_0 + s u_p \quad (4.37)$$

where c_0 and s represent the velocities of bulk sound wave and characteristic material constant, respectively. Therefore, the Mie-Gruneisen form of equation of state with the shock Hugoniot as the reference state is expressed as follows.

$$\begin{cases}
 p = p_H + \Gamma \rho (e - e_H) \\
 p_H = \frac{\rho_0 c_0 \mu (1 + \mu)}{[1 - (s - 1)\mu]^2} \\
 e_H = \frac{p_H}{2\rho_0} \left(\frac{\mu}{1 + \mu} \right)
 \end{cases} \quad (4.38)$$

Here, $\mu = \rho / \rho_0 - 1$ and the assumption of $\Gamma \rho = \Gamma_0 \rho_0$, which is indicated by experimental and theoretical works, are applied. In using this form of equation of state, it is necessary to recognize the allowable range of impact velocity, because it is not suitable for any material change, such as melting or vaporization. The shock Hugoniot data of the flyer and the target material are presented in Table 4.3 [63, 79].

Table 4.3. Shock Hugoniot data for 304 stainless steel and Kapton [63, 79].

Material	ρ_0 [kg/m ³]	c_0 [m/s]	s	Γ_0
304 SS	7900	4570	1.49	1.93
Kapton	1414	2741	1.41	0.76

At a high velocity impact, the yield strength increases as the plastic strain increases. This phenomenon is known as work hardening and plays an important role in determining the profile of shock waves at a stress of an order

of GPa. Although the yield strength also increases with the increase of strain rate, the strain-rate-dependent effect rapidly decreases when it generally exceeds a stress of 10 GPa or 10^5 s^{-1} of strain rate. This is because an increase in the dynamic stress causes a high temperature at which the strain rate dependence of the yield strength is no longer valid. Therefore, the Steinberg-Guinan model, which can reproduce experimentally measured shock-induced stress and free surface velocity profiles at a high strain rate, is used in the present impact simulation. The constitutive relation for the shear modulus, G , and the yield strength, Y , are represented as functions of effective plastic strain, density, pressure, and temperature (or internal energy).

$$G = G_0 \left\{ 1 + \left(\frac{G'_p}{G_0} \right) \frac{p}{\eta^{1/3}} + \left(\frac{G'_T}{G_0} \right) (T - 300) \right\} \quad (4.39)$$

$$Y = Y_0 \left\{ 1 + \left(\frac{Y'_p}{Y_0} \right) \frac{p}{\eta^{1/3}} + \left(\frac{Y'_T}{Y_0} \right) (T - 300) \right\} (1 + \beta \varepsilon)^n \quad (4.40)$$

These equations are subject to the limitation that $Y_0 (1 + \beta \varepsilon)^n \leq Y_{\max}$. Here, ε , T , Y_{\max} , and $\eta (= \rho / \rho_0)$ represent effective plastic strain, temperature, maximum yield stress, and compression, respectively. β and n are the hardening constant and hardening exponent, respectively. The subscript zero indicates values at the reference state ($T = 300\text{K}$, $p = 0$, $\varepsilon = 0$). Parameters with a prime and subscript also refer to derivatives of the parameter with respect to each subscript variable at the reference state. The parameters of the Steinberg-Guinan strength model for a 304 stainless steel target is represented

in Table 4.4 [80].

Table 4.4. Parameters of Steinberg-Guinan strength model for 304 stainless steel [80].

Y_0	Y_{\max}	β	n	G_0	G_p'	G_T'	Y_p'
6.7e8 [Pa]	2.5e9 [Pa]	43	0.35	7.7e10 [Pa]	1.74	-3.504e7 [Pa/°C]	7.684e-3

4.2.3 Results and Discussion

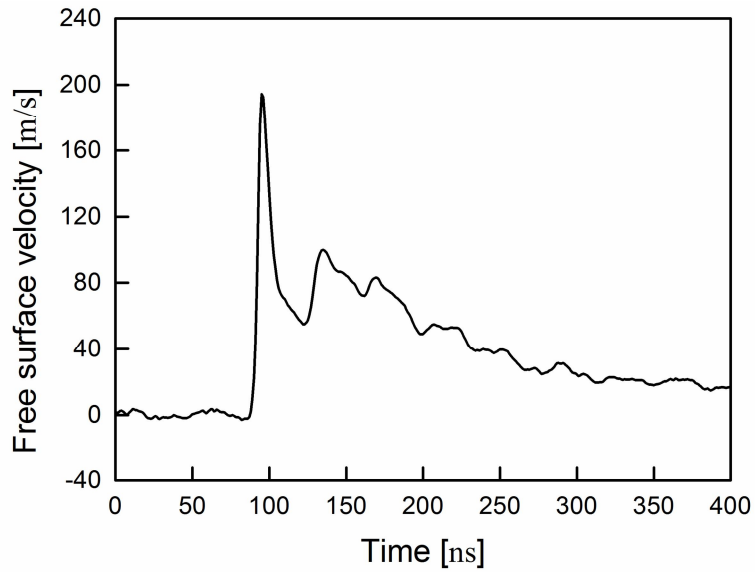


Fig. 4.15. Temporal profile of the free surface velocity measured by VISAR for a 304 stainless steel target of 100 μm thickness at the capacitor charging voltage of 1 kV.

The free surface velocity for various thicknesses was measured by VISAR to determine the decay of shock waves according to the distance of the wave propagation. Figure 4.15 presents the velocity profile of the free surface for a 304 stainless steel target of 100 μm thickness at the capacitor charging voltage of 1 kV. The first peak and consecutive peaks represent the first arrival of shock waves at the free surface and its reverberations in a target. The value of the first peak was considered to determine the strength of the shock front. Based upon the Rankine-Hugoniot jump condition and the elastoplastic behavior of the material, the longitudinal stress of shock waves is calculated with the velocity of the first peak as follows.

$$\sigma_x = \begin{cases} \rho_0 c_{el} u_p & (<\text{HEL}) \\ \rho_0 u_s u_p + \frac{2}{3} Y_0 & (>\text{HEL}) \end{cases} \quad \text{where } u_f \cong 2 u_p \quad (4.41)$$

Here, the Hugoniot elastic limit (HEL) is the transition point at which the material behavior changes from purely elastic to elastoplastic. c_{el} and Y_0 represent the velocity of elastic wave and yield strength of a material, respectively. The particle velocity is approximated from the free surface condition in which the free surface velocity, u_f , is two times faster than the particle velocity [61].

It is difficult to distinguish the first peak of a single shock for thin stainless steel below its thickness limit, where the release shock wave reflected at the free surface overlaps with the input shock loading at the impact surface. Therefore, the numerical simulation was conducted to obtain the pattern of shock attenuation for various impact velocities. The pattern was then

compared with that of the experimental results to determine the matching value [81].

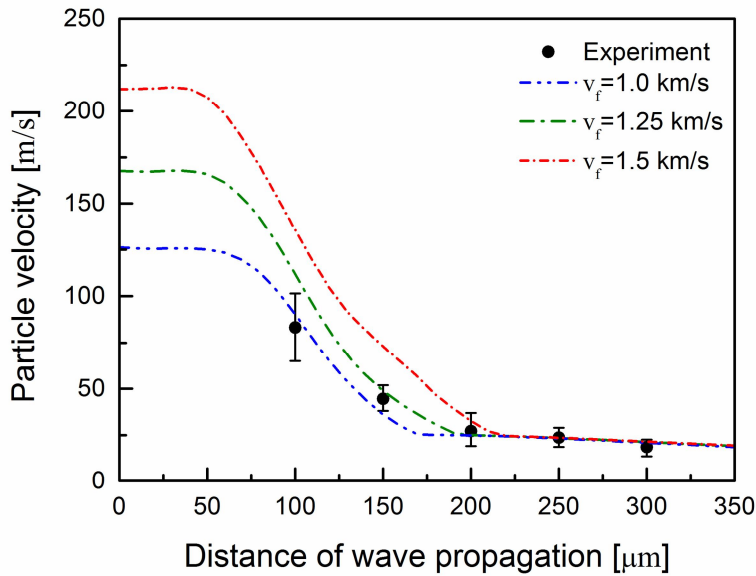


Fig. 4.16. Particle velocity generated by the shock front according to the distance of wave propagation within a 304 stainless steel target.

Figure 4.16 presents the particle velocity generated by the shock front according to the distance wave propagation within a 304 stainless steel target. The dots and lines represent the results obtained from experiment and numerical simulation, respectively. Based on the VISAR measurement, the impact velocity of a flyer was inferred by selecting a numerical case that most closely resembles the tendency of the experimental data. While the gauges in the simulation recording the time history of the shock properties are placed along the exact central axis, the focal point of the VISAR probe beam can be

aligned slightly off the center from the experimental setup. Therefore, it is necessary to recognize that experimental measurement is susceptible to deviations from the effect of the beam being off-center.

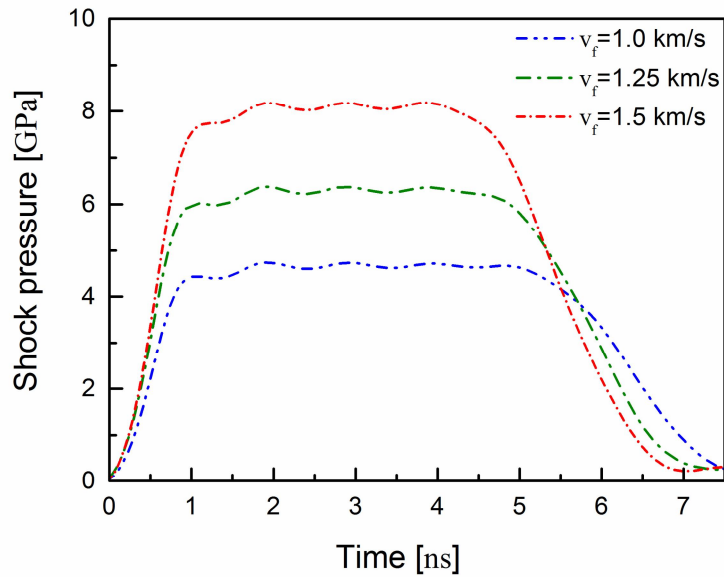
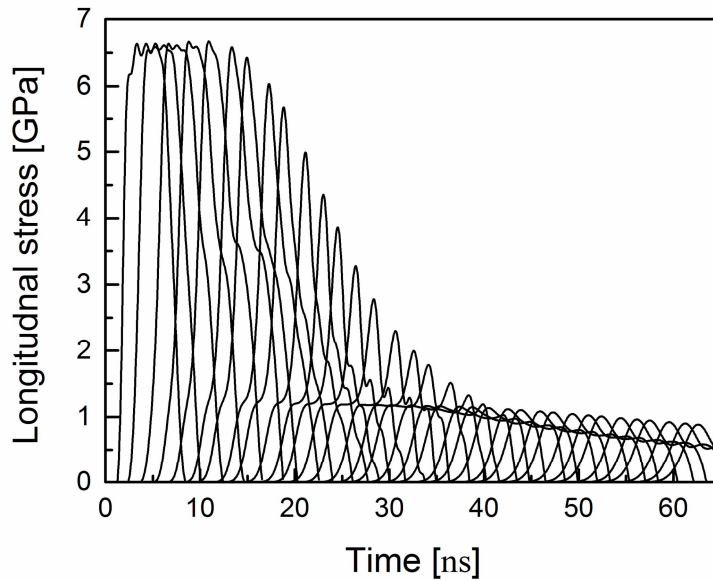


Fig. 4.17. Temporal profile of shock loading generated by flyer impact at the various velocity.

In the present system, shock waves rapidly decay within a very short distance due to the very short duration of pressure loading. As shown in Fig. 4.17, a rectangular pulse of about 5~6 ns is generated by a flyer with thickness of 12.5 μm at various impact velocities. In addition, the duration of the rectangular pulse is similar to the double transit time of the shock waves within the flyer. The pressure pulse falls off sharply as the shock impedance of the flyer is lower than that of the target material [66]. Therefore, the

pressure attenuation can be manipulated by controlling the thickness of the target and varying the impact velocity.

Since the hydrodynamic attenuation, which is related only to the thermomechanical variables, is the main cause of the large pressure drop, a shock wave starts to decrease when the release wave reaches the shock front, and its attenuation pattern is influenced by the amplitude and temporal profile of the input loading of the flyer impact [82]. Figure 4.18 shows the longitudinal stress and particle velocity generated by the flyer impact at 1.25 km/s. Gauges placed at intervals of 10 μm along the central axis are used to record shock properties on each line along the wave propagation. The shock front is sustained within approximately 50 μm and then starts to decay until it reaches the amplitude of the elastic precursor. Then, the elastic precursor is almost constant and is accompanied by a very slow decrease.



(a)

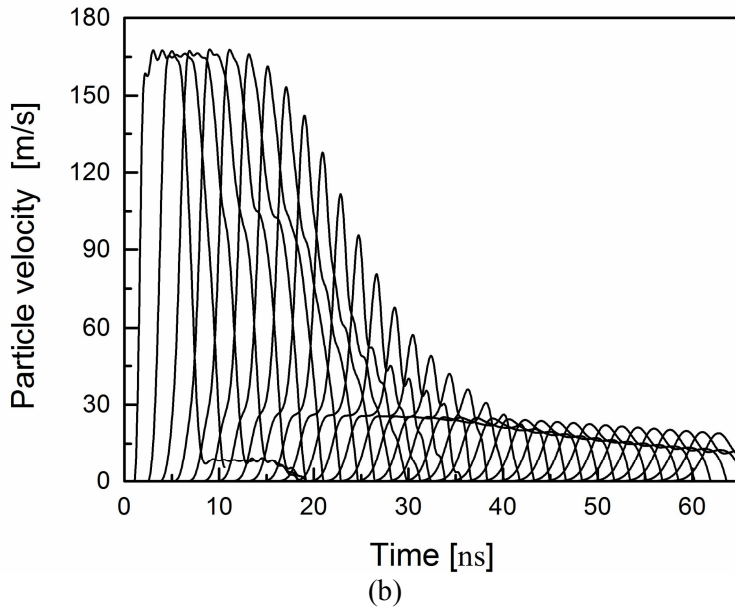


Fig. 4.18. Temporal profile of (a) longitudinal stress and (b) particle velocity generated by flyer impact at 1.25 km/s, which are recorded by gauges placed at intervals of 10 μm along the central axis from 0 to 350 μm .

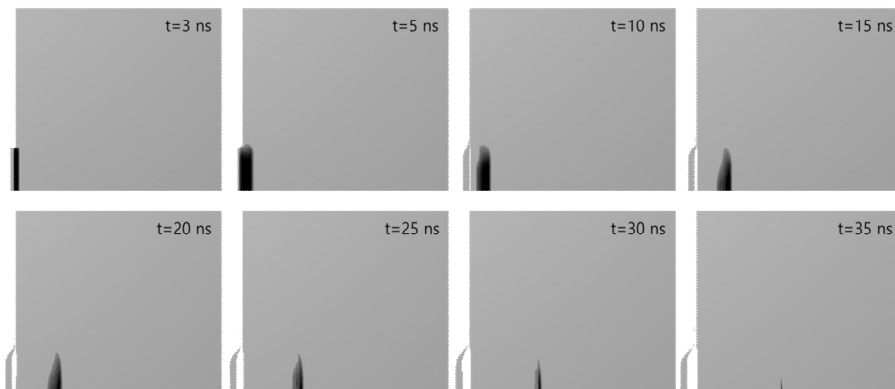


Fig. 4.19. Pressure contour of a 304 stainless steel target and a Kapton flyer along the wave propagation when it collides at the velocity of 1.25 km/s.

Moreover, geometric attenuation occurs because the one-dimensional (1-D) planar shock waves cannot be sustained along the wave propagation due to the edge effect, where the release waves emitted from the boundary of a flyer cause a decay in the shock waves. Figure 4.19 presents the pressure contour in a 304 stainless steel target subject to the Kapton flyer impact at 1.25 km/s. The consecutive images are captured at time intervals of 5 ns. The 2-D shock front structure diminishes with the radial distance of propagation. Since the input shock duration is rather short, as presented in Fig. 4.17, the plastic shock wave becomes fully attenuated within 40 ns as the elastic precursor remains. The waves propagating in the radial direction have no influence on the main shock wave since the diameter of the target is too large compared to the distance of the shock propagation. Therefore, a 304 stainless steel target with varying thicknesses from 50 μm to 200 μm is sufficient for determining the performance characteristics of the EFI unit.

Before the attenuation of a shock front, VISAR can be applied to a 304 stainless steel target with ~ 50 μm thickness, and the impact velocity is determined from the impedance matching technique, as illustrated in Fig. 4.10. When a flyer collides with a target material, two equal impinging pressures incur on both sides of the target due to pressure continuity. The relation between impact velocity and pressure is derived by combining Eqs. (4.35) and (4.37) as follows:

$$\begin{aligned}
 P_i &= \rho_{0,T} \{c_{0,T} + s_T u_{p,T}\} u_{p,T} \\
 &= \rho_{0,F} \{c_{0,F} + s_F (v_f - u_{p,T})\} (v_f - u_{p,T})
 \end{aligned} \tag{4.42}$$

$$u_{p,F} + u_{p,T} = v_f \quad (4.43)$$

The impact velocity can be summarized in terms of the particle velocity of a target and material properties as

$$v_f - u_{p,T} = -\frac{\rho_{0,F}c_{0,F}}{2s_F\rho_{0,F}} + \frac{\sqrt{(\rho_{0,F}c_{0,F})^2 + 4s_F\rho_{0,F}\{\rho_{0,T}(c_{0,T} + s_T u_{p,T})u_{p,T}\}}}{2s_F\rho_{0,F}} \quad (4.44)$$

or

$$u_{p,T} = \frac{\rho_{0,T}c_{0,T} + \rho_{0,F}c_{0,F} + 2\rho_{0,F}s_F v_f}{2(\rho_{0,F}s_F - \rho_{0,T}s_T)} + \frac{\sqrt{A}}{2(\rho_{0,F}s_F - \rho_{0,T}s_T)} \quad (4.45)$$

where $A = (-\rho_{0,T}c_{0,T} - \rho_{0,F}c_{0,F} - 2\rho_{0,F}s_F v_f)^2 - 4(\rho_{0,F}s_F - \rho_{0,T}s_T)(\rho_{0,F}c_{0,F}u_f + \rho_{0,F}s_F v_f^2)$

where P_i and v_f are the impact pressure and velocity at the impact surface, respectively. Subscripts T and F represent the properties for the target and flyer, respectively. The impact velocity of a flyer is calculated by using VISAR measurement and the shock Hugoniot data of the materials.

The resulting shock pressure versus velocity curve for a 304 stainless steel target and a flyer of polyimide is presented in Fig. 4.20. Shock pressure at the impact surface increases proportionally to the impact velocity, but the amount of velocity increase gradually decreases, because shock pressure has a quadratic term of particle velocity due to the linear relation between shock and particle velocity.

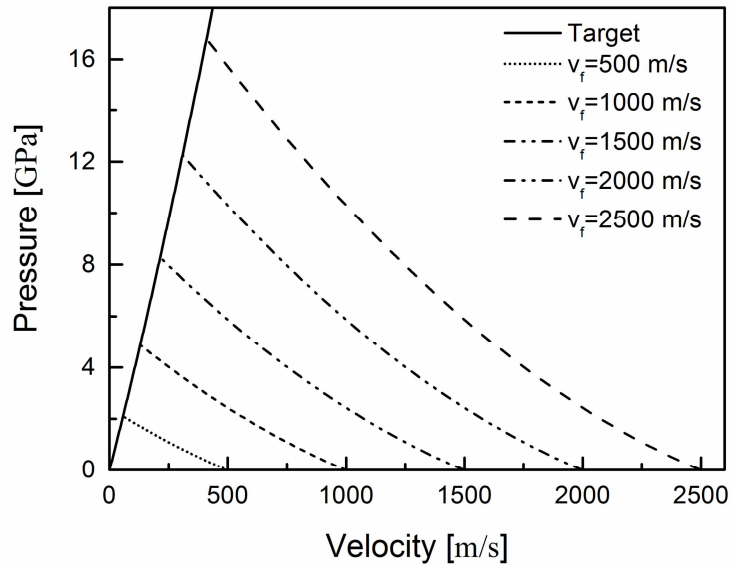


Fig. 4.20. Pressure-velocity diagram for single shock waves.

Finally, the impact velocity of the flyer is successfully obtained despite the limitation of the experimental technique, as explained earlier. The obtained pattern of shock attenuation and the obtained shock pressure-velocity curve can be used to assess the performance of the designed exploding foil initiator of a micro pyro-mechanical device.

Chapter 5. Conclusions

In this study, experiment and numerical analysis were carried out in order to analyze the behavior of plasma-driven micro shock waves with extremely high pressure and short duration. Diverse plasma-driven shock generators, such as laser-generated shock waves, a laser-driven flyer, and an exploding foil initiator, were developed for access to high pressure and precise control. A high-speed diagnostic using an instrument termed “Velocity Interferometer System for Any Reflector” (VISAR) was conducted to determine the performance characteristics of the developed plasma-driven shock systems. Numerical analysis was also performed for the verification of experimental results and for overcoming experimental limitations. The specific findings and conclusions are summarized as follows.

- (1) In the present laser-driven flyer system, the flyer velocity and the coupling efficiency were successfully enhanced by black paint coated metal plates of varying size and thickness. When compared to metal flyers without coating, the present system delivered an 90-148 % increase in the momentum of a velocity. This is because the lower reflectivity and the dust explosion of carbon nanoparticles are deemed responsible for such supreme performance. Lower reflectivity increased absorptance of the incident laser energy. A dust explosion allows the rapid and strong combustion of fine carbon particles suspended in the air. Consequently, the plasma in the black paint

coated flyer has produced a considerably higher pressure, a longer plasma duration, and therefore a higher acceleration of the mini flyer. The mini flyer flown under 1.4 km/s showed a controlled flight trajectory without fragmentation. On the other hand, around 50 % of the flyer plates break randomly at laser energies higher than ~ 1.4 J with resulting micro particles in sizes of 100 μm in diameter or less at a particle speed of 2.2 km/s. Either a single flyer as controlled by the present LDF system or a scatter of micro particles at higher intensity of a laser beam has a potential use in micro particle impact studies.

- (2) Micro-scale ice particles were accelerated to the velocity up to Mach 2 by the present laser-driven multi-layered launcher system. At the very early stage of acceleration, no significant deceleration was detected when ice particles overtook the shock front during the observed velocity regime. The deceleration of ice particles due to air drag was also not witnessed within the order of a millimeter, suggesting that drag is negligible within a mm length. The overall tendency of the velocity of ice particles and free surface velocity is similar to each other, and thus the velocity of ice particles is related to the free surface velocity of the metal foil. That is the metal foil deforms rapidly by the laser-generated plasma pressure of a few GPa, and the ice particles are detached at the free surface velocity of the metal foil. The free surface of the foil accelerates within 200 ns and then reaches the maximum velocity before 700 ns. The velocity of ice particles and longitudinal

stress of a metal foil are proportional only up to the laser irradiance of about 1.5 GW/cm^2 , and at any higher irradiance, the optical damage of the acrylic substrate occurs. This implies that the optical properties such as transmittance and damage threshold of the substrate are important design parameters when it comes to selecting the laser irradiance for a high velocities of the ice particles. It can provide an insight into the potential damage or performance threat associated with a supersonic aircraft exposed to the ice particle collisions.

- (3) Some preliminary analysis of shock behavior within a microscale steel sample was performed in an effort to collect necessary data for the miniaturization of a laser-based pyrotechnic device that works in a standard donor/acceptor configuration. The mechanism of evolution and attenuation of shock waves are explained from the hydrodynamic point of view. Shock waves start to evolve and decay when the shock or release wave reaches the shock front. Evolution and decay of shock waves is determined by the laser-generated plasma pressure. Hence, the magnitude and temporal shape of a laser beam are important for control of shock waves. As laser fluence increase, the plasma pressure increases and the occurrence time of laser ablation moves forward, while the reflectivity and ablation threshold of a target material work in opposite. As the thickness of the target decreases, the time interval and the fluctuation amplitude of the free surface velocity between each crest and trough become shorter and narrower. In the case of a thin foil

target whose double transit time of a shock wave is much shorter than the duration of the plasma pressure loading, numerous reverberations of shock and release waves rapidly accelerate a target without noticeable fluctuations. The minimum sample thickness required for sharpening the shock front and for avoiding pressure decrease by multiple reverberations of shock and release waves were determined in order to obtain exact pressure at a desired distance. A method of determining the HEL for such microscale sample was also developed. Thus the reported results can be used in the precise controlling of the shock strength during the laser initiation of microscale pyrotechnic devices.

- (4) A miniaturized exploding foil initiator (EFI), based on high pulsed electrical power generator, was designed to launch a micro Kapton flyer for impact initiation of high explosives in order to understand its performance characterization. Since the flyer poses various flight motion of rotation, bend, and fragmentation due to its extreme thinness, impedance matching technique was utilized to predict the average impact velocity of the flyer. For this qualification step, explosive substances were replaced with a witness plate and then measurement of shock attenuation within a stainless steel witness plate was conducted. Also, the lens configuration of a VISAR probe was specially designed to insure the focal spot reduction and the receiving angle increase. Thus, the exact velocity at the center of a stainless target was measured without any signal loss, despite the relatively large deformation at the

local spot. The obtained shock attenuation pattern according to the distance of wave propagation were used to infer the averaged velocity of a flyer using the impedance matching technique. Subsequently, the relations between the flyer velocity, the amplitude, and the width of impact loading with respect to input voltage of the EFI are established. The results are useful to determine the performance characteristic of the miniaturized pyrotechnic unit.

In this study, all aspects of the system including laser-matter interaction, plasma-driven shock waves, flyer acceleration, shock loading by flyer impact, and shock behavior in solids have been discussed. Therefore, the reported results establish the basis for future shock studies by providing a design guideline for a robust and optimized micro shock system.

References

- [1] Barker, L., 1972, "Laser interferometry in shock-wave research," *Experimental Mechanics*, 12(5), pp. 209-215.
- [2] Hemsing, W. F., 1979, "Velocity sensing interferometer (VISAR) modification," *Review of Scientific Instruments*, 50(1), pp. 73-78.
- [3] Paisley, D., 1989, "Laser-driven miniature flyer plates for shock initiation of secondary explosives," Los Alamos National Lab., NM (USA).
- [4] Lawrence, R. J., and Trott, W. M., 1993, "Theoretical analysis of a pulsed-laser-driven hypervelocity flyer launcher," *International Journal of Impact Engineering*, 14(1), pp. 439-449.
- [5] Miller, C. W., Kishimura, H., Kelly, S. C., and Thadhani, N., "LASER-DRIVEN MINIFLYER SYSTEM FOR SHOCK COMPRESSION STUDIES," *Proc. SHOCK COMPRESSION OF CONDENSED MATTER 2009: Proceedings of the American Physical Society Topical Group on Shock Compression of Condensed Matter*, AIP Publishing, pp. 1147-1150.
- [6] Robbins, D., Stahl, D., Sheffield, S., Alexander, D., Paisley, D., Kelly, A., Hamrahan, R., Snow, R., Gehr, R., and Rupp, T., 2004, "Laser-driven miniflyer system," *Technical Report No. La-14150*, Los Alamos National

Laboratory.

[7] Chen, X., and Wang, H.-X., 2001, "A calculation model for the evaporation recoil pressure in laser material processing," *Journal of Physics D: Applied Physics*, 34(17), p. 2637.

[8] Bowden, M., and Knowles, S., "Optimisation of laser-driven flyer velocity using photonic Doppler velocimetry," *Proc. SPIE Optical Engineering+ Applications*, International Society for Optics and Photonics, pp. 743403-743403-743411.

[9] Chmel, A., 1997, "Fatigue laser-induced damage in transparent materials," *Materials Science and Engineering: B*, 49(3), pp. 175-190.

[10] Hatt, D., and Waschl, J., "A study of laser-driven flyer plates," *Proc. American Institute of Physics Conference Series*, pp. 1221-1224.

[11] Brierley, H., Williamson, D. M., and Vine, T., "Improving laser-driven flyer efficiency with high absorptance layers," *Proc. SHOCK COMPRESSION OF CONDENSED MATTER-2011: Proceedings of the Conference of the American Physical Society Topical Group on Shock Compression of Condensed Matter*, AIP Publishing, pp. 315-318.

[12] Greenaway, M., Proud, W., Field, J., and Goveas, S., 2003, "A laser-accelerated flyer system," *International journal of impact engineering*, 29(1), pp. 317-321.

- [13] Safi, I., 2000, "Recent aspects concerning DC reactive magnetron sputtering of thin films: a review," *Surface and Coatings Technology*, 127(2), pp. 203-218.
- [14] Stahl, D. B., Gehr, R. J., Harper, R. W., Rupp, T. D., Sheffield, S. A., and Robbins, D. L., "Flyer velocity characteristics of the laser-driven miniflyer system," *Proc. AIP CONFERENCE PROCEEDINGS*, IOP INSTITUTE OF PHYSICS PUBLISHING LTD, pp. 1087-1090.
- [15] White, F. M., 1999, "Fluid mechanics. sl," McGraw-Hill.
- [16] Djurišić, A. B., and Li, E. H., 1999, "Optical properties of graphite," *Journal of applied physics*, 85(10), pp. 7404-7410.
- [17] Palik, E. D., 1998, *Handbook of optical constants of solids*, Academic press.
- [18] Rakić, A. D., Djurišić, A. B., Elazar, J. M., and Majewski, M. L., 1998, "Optical properties of metallic films for vertical-cavity optoelectronic devices," *Applied optics*, 37(22), pp. 5271-5283.
- [19] Benavides, O., Lebedeva, O., and Golikov, V., 2011, "Reflection of nanosecond Nd: YAG laser pulses in ablation of metals," *Optics express*, 19(22), pp. 21842-21848.
- [20] McMordie, J., and Roberts, P., 1975, "The interaction of pulsed CO₂ laser radiation with aluminium," *Journal of Physics D: Applied Physics*, 8(7),

p. 768.

[21] Cloutis, E. A., Gaffey, M. J., and Moslow, T. F., 1994, "Spectral reflectance properties of carbon-bearing materials," *Icarus*, 107(2), pp. 276-287.

[22] Heng, W., Zhen'an, T., Zhu, W., Wan, C., and Daquan, Y., 2013, "Simulation of through via bottom—up copper plating with accelerator for the filling of TSVs," *Journal of Semiconductors*, 34(9), p. 096001.

[23] Nielsch, K., Choi, J., Schwirn, K., Wehrspohn, R. B., and Gösele, U., 2002, "Self-ordering regimes of porous alumina: the 10 porosity rule," *Nano letters*, 2(7), pp. 677-680.

[24] Robertson, J., 1992, "Properties of diamond-like carbon," *Surface and Coatings Technology*, 50(3), pp. 185-203.

[25] Leider, H., Krikorian, O., and Young, D., 1973, "Thermodynamic properties of carbon up to the critical point," *Carbon*, 11(5), pp. 555-563.

[26] Shen, Z., Zhang, S., Lu, J., and Ni, X., 2001, "Mathematical modeling of laser induced heating and melting in solids," *Optics & laser technology*, 33(8), pp. 533-537.

[27] Akoshima, M., Abe, H., and Baba, T., 2015, "Thermal diffusivity of carbon materials as candidate reference materials," *International Journal of Thermophysics*, 36(10-11), pp. 2507-2517.

- [28] Casalegno, V., Vavassori, P., Valle, M., Ferraris, M., Salvo, M., and Pintsuk, G., 2010, "Measurement of thermal properties of a ceramic/metal joint by laser flash method," *Journal of Nuclear Materials*, 407(2), pp. 83-87.
- [29] Cengel, Y., 2007, *Introduction to thermodynamics and heat transfer+* EES software, New York: McGraw Hill Higher Education Press.
- [30] Bao, S., Tang, K., Kvithyld, A., Tangstad, M., and Engh, T. A., 2011, "Wettability of aluminum on alumina," *Metallurgical and materials transactions B*, 42(6), pp. 1358-1366.
- [31] El-Hadek, M. A., and Kaytbay, S. H., 2013, "Fracture properties of SPS tungsten copper powder composites," *Metallurgical and Materials Transactions A*, 44(1), pp. 544-551.
- [32] Rohsenow, W. M., Hartnett, J. P., and Ganic, E. N., 1985, "Handbook of heat transfer fundamentals," New York, McGraw-Hill Book Co., 1985, 1440 p. No individual items are abstracted in this volume.
- [33] Chen, T., Pang, S., Tang, Q., Suo, H., and Gong, S., 2015, "Induction of ball-filled pores in electron beam freeform fabrication of Ti-6-Al-4-V alloy by dissolved gas and metallic vapor," *Metallurgical and Materials Transactions A*, 46(12), pp. 5499-5503.
- [34] Rusjan, D., 2012, *Copper in horticulture*, INTECH Open Access Publisher.

- [35] Hultgren, R., Desai, P. D., Hawkins, D. T., Gleiser, M., and Kelley, K. K., 1973, "Selected values of the thermodynamic properties of the elements," DTIC Document.
- [36] Peterlongo, A., Miotello, A., and Kelly, R., 1994, "Laser-pulse sputtering of aluminum: Vaporization, boiling, superheating, and gas-dynamic effects," *Physical Review E*, 50(6), p. 4716.
- [37] Zhang, W., Yao, Y. L., and Chen, K., 2001, "Modelling and analysis of UV laser micromachining of copper," *The International Journal of Advanced Manufacturing Technology*, 18(5), pp. 323-331.
- [38] Fung, K., Chow, J. C., and Watson, J. G., 2002, "Evaluation of OC/EC speciation by thermal manganese dioxide oxidation and the IMPROVE method," *Journal of the Air & Waste Management Association*, 52(11), pp. 1333-1341.
- [39] Jamil, Y., Saeed, H., Ahmad, M. R., Khan, S. A., Farooq, H., Shahid, M., Zia, K., and Amin, N., 2013, "Measurement of ablative laser propulsion parameters for aluminum, Co–Ni ferrite and polyurethane polymer," *Applied Physics A*, 110(1), pp. 207-210.
- [40] Leitz, K.-H., Redlingshöfer, B., Reg, Y., Otto, A., and Schmidt, M., 2011, "Metal ablation with short and ultrashort laser pulses," *Physics Procedia*, 12, pp. 230-238.

- [41] Ready, J. F., 1971, *Effects of High Power Laser Radiation*, Acad. Press.
- [42] Eckhoff, R. K., 2003, *Dust explosions in the process industries: identification, assessment and control of dust hazards*, Gulf professional publishing.
- [43] Fox, J. A., 1974, "Effect of water and paint coatings on laser-irradiated targets," *Applied Physics Letters*, 24(10), pp. 461-464.
- [44] Gojani, A. B., Yoh, J. J., and Yoo, J. H., 2008, "Extended measurement of crater depths for aluminum and copper at high irradiances by nanosecond visible laser pulses," *Applied Surface Science*, 255(5), pp. 2777-2781.
- [45] Chirila, T. V., Constable, I. J., van Saarloos, P. P., and Barrett, G. D., 1990, "Laser-induced damage to transparent polymers: chemical effect of short-pulsed (Q-switched) Nd: YAG laser radiation on ophthalmic acrylic biomaterials: I. A review," *Biomaterials*, 11(5), pp. 305-312.
- [46] Mason, J. G., Strapp, J. W., and Chow, P., "The ice particle threat to engines in flight," *Proc. 44th AIAA Aerospace Sciences Meeting*, Reno, Nevada, pp. 9-12.
- [47] Boyce, B., Chen, X., Hutchinson, J., and Ritchie, R., 2001, "The residual stress state due to a spherical hard-body impact," *Mechanics of Materials*, 33(8), pp. 441-454.
- [48] Hamed, A., Tabakoff, W., and Wenglarz, R., 2006, "Erosion and

deposition in turbomachinery," *Journal of Propulsion and Power*, 22(2), pp. 350-360.

[49] Lee, J.-H., Veysset, D., Singer, J. P., Retsch, M., Saini, G., Pezeril, T., Nelson, K. A., and Thomas, E. L., 2012, "High strain rate deformation of layered nanocomposites," *Nature communications*, 3, p. 1164.

[50] Yu, H., Fedotov, V., Baek, W., and Yoh, J. J., 2013, "Towards controlled flyer acceleration by a laser-driven mini flyer," *Applied Physics A*, pp. 1-8.

[51] Bergman, T. L., Incropera, F. P., DeWitt, D. P., and Lavine, A. S., 2011, *Fundamentals of heat and mass transfer*, John Wiley & Sons.

[52] Berthe, L., Fabbro, R., Peyre, P., Tollier, L., and Bartnicki, E., 1997, "Shock waves from a water-confined laser-generated plasma," *Journal of Applied Physics*, 82(6), pp. 2826-2832.

[53] Walsh, J. M., and Christian, R. H., 1955, "Equation of state of metals from shock wave measurements," *Physical Review*, 97, pp. 1544-1556.

[54] Marshall, J., 1988, "Lasers in ophthalmology: the basic principles," *Eye*, 2, pp. S98-S112.

[55] Oka, Y. I., Nagahashi, K., Ishii, Y., Kobayashi, Y., and Tsumura, T., 2005, "Damage behaviour of metallic materials caused by subsonic to hypervelocity particle impact," *Wear*, 258(1-4), pp. 100-106.

[56] Kim, Y. K., and Itoh, S., 2007, "A study on the behavior of underwater

shock waves generated in a water container and its application to magnetic refrigeration material," *The International Journal of Multiphysics*, 1(3), pp. 291-302.

[57] Kim, B., Park, J., and Yoh, J. J., 2016, "Analysis on shock attenuation in gap test configuration for characterizing energetic materials," *Journal of Applied Physics*, 119(14), p. 145902.

[58] Hammer, D. X., Jansen, E. D., Frenz, M., Noojin, G. D., Thomas, R. J., Noack, J., Vogel, A., Rockwell, B. A., and Welch, A. J., 1997, "Shielding properties of laser-induced breakdown in water for pulse durations from 5 ns to 125 fs," *Applied optics*, 36(22), pp. 5630-5640.

[59] Kinslow, R., 2012, *High-velocity impact phenomena*, Elsevier.

[60] Yu, H., Kim, J., and Yoh, J. J., 2014, "A high velocity impact experiment of micro-scale ice particles using laser-driven system," *Journal of Applied Physics*, 116(17), p. 173508.

[61] Forbes, J. W., 2013, *Shock wave compression of condensed matter: a primer*, Springer Science & Business Media.

[62] Asay, J. R., and Shahinpoor, M., 2012, *High-pressure shock compression of solids*, Springer Science & Business Media.

[63] Marsh, S. P., 1980, *LASL shock Hugoniot data*, Univ of California Press.

- [64] Cottet, F., and Romain, J., 1982, "Formation and decay of laser-generated shock waves," *Physical Review A*, 25(1), p. 576.
- [65] Loeb, A., and Eliezer, S., 1985, "An analytical model for creation and decay of strong shock waves caused by a trapezoidal laser pulse," *Physics of Fluids (1958-1988)*, 28(4), pp. 1196-1201.
- [66] Antoun, T., 2003, *Spall fracture*, Springer Science & Business Media.
- [67] Harris, A., 1950, "The decay of plane, cylindrical and spherical shock waves," *Underwater explosion research*, 1, pp. 1053-1056.
- [68] Fabbro, R., Fournier, J., Ballard, P., Devaux, D., and Virmont, J., 1990, "Physical study of laser-produced plasma in confined geometry," *Journal of applied physics*, 68(2), pp. 775-784.
- [69] Romain, J., and Darquey, P., 1990, "Shock waves and acceleration of thin foils by laser pulses in confined plasma interaction," *Journal of Applied Physics*, 68(4), pp. 1926-1928.
- [70] Fairand, B., and Clauer, A., 1979, "Laser generation of high-amplitude stress waves in materials," *Journal of Applied Physics*, 50(3), pp. 1497-1502.
- [71] Johnson, J., and Rohde, R., 1971, "Dynamic Deformation Twinning in Shock-Loaded Iron," *Journal of Applied Physics*, 42(11), pp. 4171-4182.
- [72] Peyre, P., Berthe, L., Scherpereel, X., and Fabbro, R., 1998, "Laser-shock processing of aluminium-coated 55C1 steel in water-confinement

regime, characterization and application to high-cycle fatigue behaviour," *Journal of materials science*, 33(6), pp. 1421-1429.

[73] Dalton, D., Brewer, J., Bernstein, A., Grigsby, W., Milathianaki, D., Jackson, E., Adams, R., Rambo, P., Schwarz, J., and Edens, A., 2008, "Laser-induced spallation of aluminum and Al alloys at strain rates above $2 \times 10^6 \text{ s}^{-1}$," *Journal of Applied Physics*, 104(1), p. 013526.

[74] Ebenhöch, S., Nau, S., and Häring, I., 2015, "Validated model-based simulation tool for design optimization of exploding foil initiators," *The Journal of Defense Modeling and Simulation: Applications, Methodology, Technology*, 12(2), pp. 189-207.

[75] Nappert, L., 1996, *An Exploding Foil Initiator System*, Defence Research Establishment Valcartier.

[76] Schwarz, A. C., 1981, "Study of factors which influence the shock-initiation sensitivity of hexanitrostilbene (HNS)," Sandia National Labs., Albuquerque, NM (USA).

[77] Dennis-Koller, D., Escobedo-Diaz, J. P., Cerreta, E., Bronkhorst, C. A., Hansen, B., Lebensohn, R., Mourad, H., Patterson, B., Tonks, D., and Elert, M. L., "Controlled shock loading conditions for microstructural correlation of dynamic damage behavior," *Proc. AIP Conference Proceedings-American Institute of Physics, Citeseer*, p. 1325.

- [78] Kiang, Y., and Lang, R., 1983, "Measuring focused Gaussian beam spot sizes: a practical method," *Applied optics*, 22(9), pp. 1296-1297.
- [79] May, C. M., Tarver, C. M., Elert, M., Furnish, M. D., Anderson, W. W., Proud, W. G., and Butler, W. T., "Modeling short shock pulse duration initiation of Lx-16 and Lx-10 charges," *Proc. Aip Conference Proceedings*, p. 275.
- [80] Steinberg, D., 1996, *Equation of state and strength properties of selected materials*, Lawrence Livermore National Laboratory Livermore, CA.
- [81] Yu, H., and Yoh, J. J., 2016, "Laser-generated shock wave attenuation aimed at microscale pyrotechnic device design," *AIP Advances*, 6(5), p. 055314.
- [82] Duvall, G., 1978, "Maxwell-like relations in condensed materials," *Iranian J. of Sci. and Techn*, 7, pp. 57-69.

초 록

1900년대 초반부터 우주 및 방위 산업이 중요해짐에 따라 충돌, 폭발, 그리고 고에너지 물질의 사용과 같은 고온, 고압 현상에 대한 관심이 지속적으로 증가해오고 있다. 고온 및 고압의 극한 조건에서의 재료의 물성은 일반적인 대기 환경에서 관측되는 거동과는 현저하게 다르다. 하지만 극한 조건에서 응축 물질의 반응에 대한 정보는 여전히 부족하며 이에 대한 연구가 요구되고 있다.

플라즈마 구동 충격 압축은 가스, 화약, 전기, 레일건과 같은 기존의 대규모 고압 발생 장치와 달리 실험실 규모에서 높은 압력의 충격파를 발생시킬 수 있는 유망한 기술이다. 게다가 비용 절감, 시간 단축, 제어 개선, 높은 반복성, 시스템의 소형화 등 다양한 측면에서 상당한 이점을 제공한다. 따라서 본 연구에서는 극한 고압 및 초단의 플라즈마 구동 충격파 거동을 분석하기 위한 실험 및 수치 해석을 수행하였다.

고압 환경 모사 및 정밀 제어를 위하여 레이저 유도 충격파, 레이저 구동 비행편, 그리고 슬래퍼 기폭관과 같은 다양한 플라즈마 구동 충격파 발생 장치를 개발하였다. 개발된 플라즈마 구동 충격 시스템의 성능 특성을 규명하기 위해 바이자 속도 간섭계를 활용한 충격파 측정을 수행하였다. 실험 결과의 검증 및 실험적 기법의 한계를 극복하기 위한 수치 해석 또한 함께 진행하였다.

본 연구를 통하여 레이저 물질 상호 작용, 플라즈마 구동 충격파,

비행편 가속, 비행편 충돌에 의한 충격 하중, 그리고 매질 내에서의 충격파 거동 등을 포함한 시스템의 모든 측면이 고찰되었다. 따라서 상기 결과는 견고하고 최적화된 플라즈마 구동 충격 시스템 설계를 위한 지침을 제공함으로써 향후 충격파 연구의 기반을 구축하였다.

주요어: 충격파, 수력학적 감쇠, 레이저, 플라즈마, 비행편, 고속, 바이자 속도 간섭계

학 번: 2012-30179